Numerical simulation of compressible multiphase flows

by

Zahra Hosseinzadeh Nik

A dissertation submitted to the graduate faculty

in partial fulfillment of the requirements for the degree of

DOCTOR OF PHILOSOPHY

Majors: Aerospace Engineering and Mechanical Engineering

Program of Study Committee:
Jonathan D. Regele, Co-Major Professor
Shankar Subramaniam, Co-Major Professor
Paul Durbin
Rodney O. Fox
Alberto Passalacqua

Iowa State University

Ames, Iowa

2017

DEDICATION

To my family.

TABLE OF CONTENTS

LIST OF TABLES

LIST OF FIGURES

ACKNOWLEDGEMENTS

This thesis would not have been possible without the support and guidance of many people.

First and foremost, I would like to thank my advisor Prof. Jonathan Regele for his instrumental role in my journey. His expertise guided the direction of my work, while his patience allowed the freedom for me to think independently. Second I would like to thank my co-advisor Prof. Shankar Subramaniam who I am incredibly fortunate to have had the opportunity to work with and has contributed immensely to my professional development.

I also owe my gratitude to the other members on my committee, Prof. Paul Durbin, Prof. Rodney Fox and Prof. Alberto Passalacqua for their guidance and efforts in this work. In addition, I want to thank all of my friends I have gained during my time at Iowa State for their help in maintaining some semblance of social life during my college career. Finally, my spouse and parents deserve special thanks for their enduring support and encouragement.

ABSTRACT

Compressible multiphase flow can be observed in numerous applications. The flow regimes in these applications are either gas-solid or gas-liquid. These flows often feature either rigid (i.e. solid) or deformable (i.e. droplet or bubble) particles and develop complex dynamics as particles interact with flow features such as shock waves. These shock-particle interactions introduce unique challenges for numerical simulation. This thesis will focus on the development and application of numerical methods for the prediction of shock-particle interaction in both gas-solid and gas-liquid regimes.

First, the simulation of a shock wave impacting a particle cloud is investigated following Ref. [1] to replicate the canonical multiphase shock tube problem of Wagner et al.[2], [3] experiments. This study is motivated by a lack of knowledge in the dense gas particle regime due to the inherent difficulties encountered in quantitative measurement of flow properties in this regime. Wagner et al.[2] pioneered an experiment to isolate the flow behavior involved, using a multiphase shock tube. However, the highly unsteady flow behavior inside the particle curtain and the wake behind that is still uncharacterized. This dissertation aims to study this canonical problem to quantify flow unsteadiness and velocity fluctuations using particle-resolved direct numerical simulation (PR-DNS) by solving the compressible full Navier-Stokes equations coupled with an extended Immersed Boundary Method (IBM) for compressible flow, in the Parallel Adaptive Wavelet-Collocation Method (PAWCM) framework. This investigation reveals the sources of unsteadiness and importance of fluctuating field statistics such as kinetic energy and Reynolds stress terms.

Secondly, we focus on development of a flow solver to investigate shock-particle interaction in gas-liquid flows with surface tension effects. The motivation for this study is to gain a deeper understanding of the process of fuel atomization in a supersonic cross flow of a supersonic

combustor under the startup conditions. Simulating interface dynamics and surface tension effect during shock-particle interactions in compressible gas-liquid flows is extremely challenging and requires robust numerical methods that can handle discontinuities caused by both material interfaces and shocks. In order to simulate these dynamics, a solver is developed in PAWCM based on a five-equation interface-capturing model and an existing shock capturing scheme. An interface sharpening scheme is developed for PAWCM to counter the numerical diffusion induced by the shock-capturing scheme, and to maintain the immiscibility condition at the material interface. The capillary force is implemented using a continuous surface approach. Capability of the flow solver is demonstrated by several one and two dimensional benchmark problems.

Finally, a shock-capturing two-fluid scheme is developed to further quantify the flow features obtained by PR-DNS results via solving the phase-averaged governing equations. This is developed based on an extension of the latest version of the Advection Upstream Splitting Method (AUSM), called the all-speed simple low-dissipation AUSM (SLAU) scheme. The scheme features low dissipation without any tunable parameters in low Mach number regimes while maintaining the robustness of AUSM-family fluxes at high Mach numbers with a very simple formulation. This has been tested on benchmark problems and was compared with the two-phase AUSM+ and AUSM+-up schemes.

References

[1] J. D. Regele, J. Rabinovitch, T. Colonius, and G. Blanquart, “Unsteady effects in dense, high speed, particle laden flows,” *Int. J. Multiph. Flow*, vol. 61, no. May, pp. 1–13, 2014.

[2] J. L. Wagner *et al.*, “A multiphase shock tube for shock wave interactions with dense particle fields,” *Exp. Fluids*, vol. 52, no. 6, pp. 1507–1517, 2012.

[3] J. L. Wagner *et al.*, “Interaction of a planar shock with a dense field of particles,” in *AIP Conference Proceedings*, 2012, vol. 1426, pp. 1655–1658.

CHAPTER 1. INTRODUCTION

Compressible multiphase flows with shock-particle interaction are observed in many environmental and industrial applications such as volcanic eruptions, supernovae, multiphase explosions, nuclear reactors and high-speed propulsion systems [1]–[3]. These flows can be categorized as existing in either gas-solid or gas-liquid regimes. Experimental studies of these flows are difficult, because the velocities, pressures, and temperatures at which these flows occur are very high, making experiments hazardous and expensive [4]. This makes modeling and simulation of these flows an attractive alternative to experimental approaches. In these multiphase flow regimes, due to the presence of compressible flow features such as shock waves, expansion waves and contact discontinuities, the interactions between the phases are more complicated than those that occur in incompressible flows. These features introduce unique challenges for numerical simulations. Thus, the primary purpose of this work is to develop and apply suitable numerical methods for prediction of shock-particle interaction in both the gas-solid and gas-liquid regimes at the microscale, where the details of interaction on the scale of particle and shock are well resolved. From there, an attempt is made to develop a mesoscale two-fluid model.

1.1 Microscale study of shock-particle interaction in compressible gas-solid flows

The interaction between shock waves and particles in gas-solid flows has been studied in two setups. First, the shock interaction with an isolated particle and second the shock interaction with a cloud of particles.

The shock-single particle interaction in the gas-solid flow has been extensively studied over the last two decades [5]–[11]. Igra and Takayama [12] performed shock tube experiments and reported that the unsteady drag experienced by a particle affected by a shock is significantly larger than that obtained from similar steady flow drag model. Loth [13] investigated the effect of

compressibility on the drag experienced by a particle and showed that the drag is dominated by compressibility at high Reynolds numbers. Efforts have been made to create a proper model for the unsteady drag force in shock-single-particle flow [3], [6], [14], [15].

In typical applications, however, shock waves interact with a cloud of particles. The model developed for a shock single particle interaction is suitable for the study of shock-particle interaction in the dilute gas-solid flow regimes where solid phase volume fraction, α_s is less than 0.01 [16]–[23]. However, these models are invalid for flows where the solid volume fraction is high such as the dense regime ($0.01 \leq \alpha_s \leq 0.5$) and granular regime ($\alpha_s \gg 0.5$). Computational modeling has also shown the ability to capture the gas–solid flow physics in the granular regime. For instance, using the continuum mixture theory developed by Baer and Nunziato [24], Baer [25] accurately modeled the normal shock impingement studies of Sheffield et al. [26], [27]. However, these theories also become invalid for flows in the intermediate (dense) regime.

To gain insight into the complicated phenomena associated with this flow regime, an experiment was conducted by Wagner et al.[28] to develop quantitative measurements of shock-particle cloud interaction in the compressible dense regime. This was accomplished by driving a planar shock wave into a dense particle cloud having a volume fraction of $\alpha_s = 0.2$ and measuring the resulting interaction dynamics with high-speed Schlieren imaging and fast-response pressure sensors. However, due to the opaque nature of the particles, observation of flow features at the particle scale was not possible. Therefore, numerical simulations must be used in order to fully characterize the flow [4]. Ling et al. [3] attempt to provide a physical interpretation of the experimental data through a volume-averaged point-particle model in mesoscale using new one-dimensional particle drag models. The numerical results show that the physics in the interaction

between a shock wave with a dense gas-particle cloud is markedly different from that with a dilute mixture and that the dense particle volume fractions lead to a significant increase in interphase momentum transfer compared to the standard drag law (e.g., Clift and Gauvin [29]). Moreover, the dense particle curtain was reported to prolong unsteadiness by time scales several orders of magnitude [30]–[32] in comparison with single particle impacted under similar flow conditions [9], [33], [34].

Regele et al. [1] were also able to capture the interaction unsteadiness, through a microscale Euler simulation. They show that after the shock wave impacts the particle cloud, strong unsteady effects and significant velocity fluctuations arise inside the cloud and in the wake immediately behind it. However, the sources of this strong unsteadiness and the development of the fluctuating field statistics is not clear, as of yet. This work attempts to further quantify the flow dynamics in this canonical problem by quantification of the flow unsteadiness and fluctuating field statistics using particle resolved direct numerical simulation of the Navier-Stokes equations.

1.2 Microscale study of shock particle interaction in compressible gas-liquid flows

In most applications of compressible gas-liquid flows, shock waves interact with deformable particle such as liquid droplets or bubbles [35]–[39]. These interactions can be observed in supersonic combustors, such as scramjets under startup conditions or in underwater explosions[40]. Due to the challenges of studying these flows experimentally, a numerical approach is necessary to simulate compressible gas-liquid flows under the influence of surface tension forces. In this interaction the material interface deforms and interacts with the shock waves, with surface tension forces playing an important role in maintaining the interface. The interaction between the shock wave and deformable interface increases the difficulty in utilizing a numerical

method [41]. A proper methodology requires treatment of the interface dynamics between the two phases. This treatment can be categorized as a sharp interface method or diffused interface method.

In a sharp interface method, the interface is kept sharp via explicit representation and is tracked in a discontinuous way. However, there are several different sharp interface methods such as front tracking, Arbitrary Lagrangian Eulerian (ALE) method and the level set method. The front tracking method [42]–[45] separately tracks the interface (front) and creates modification to the cells where the interface lies to account for the discontinuity. This modification requires special treatment to maintain numerical stability. ALE methods [46]–[48] require using an unstructured mesh and a re-meshing algorithm to deform the mesh with the interface. The level set method [49]–[52] defines a series of ghost cells near the interface that includes the fluid mixture. The immiscibility condition can be maintained by a level set re-initialization technique [53].

An alternative approach is a diffused interface method [54]–[56]. The concept behind the method is similar to a shock capturing scheme and can easily handle interface deformation on fixed or adaptive Cartesian grids. This method adds an advection equation for the volume fraction to capture the interface and is simple to implement in multiple dimensions. However, the main drawback of the method is numerical diffusion of the interface. Depending on the amount of numerical viscosity and the dissipation effect introduced by the shock capturing scheme, the interface can become overly diffused. In simulations of shock-interface interaction, this can introduce a significant error if strong shocks are present, or the density ratio of the two phases is large.

To counter numerical diffusion of the material interface there are several methods such as the Weighted Essentially Non-Oscillatory (WENO) [41], [57] or the Localized Artificial Diffusivity (LAD) scheme [40], [58]–[60]. These are high-order reconstruction schemes that decrease the

numerical diffusion and help to accurately capture interface dynamics. However, these methods do not satisfy the total variation diminishing (TVD) criteria and introduce spurious oscillation across the material interface [41]. Thus, the curvature calculation becomes problematic when surface tension effects are incorporated in the solver. An alternative approach is the interface steepening technique developed by Shukla et. al. [61] that has been successful in countering the numerical diffusion of a material interface when coupled with TVD special reconstruction. This scheme successfully sharpens the interface during shock-droplet interactions in the presence of a high density ratio. This method is based on implementing the compression step in the pseudo time step. Further development of this method with a nonlinear-preconditioning and incorporating in the physical time step is performed in Ref. [62], [63].

While compressible gas-liquid flow has been studied numerically in the past [64]–[69] , surface tension has often been neglected. These studies have mostly focused on the early stages of shock interaction with the interface where surface tension effect does not play an important role [70], [71] . On the other hand, the existing compressible models, which include surface tension effects, have mostly focused on low Mach numbers, for which the compressible effect is not very important, such as cavitation or evaporation. There are only some recent studies on incorporation of surface tension effect in compressible gas-liquid flows solver [71]–[75]. In these studies the surface tension force has been incorporated in either the conservative form [75] or in the non-conservative form [71]–[74]. The non-conservative form has been more popular as the surface curvature, on which the surface tension is derived, can be controlled easier.

In this work, we will focus on developing a compressible gas-liquid solver based on the diffused interface method coupled with the interface steepening scheme to capture the interface

dynamics and include surface tension effects based on the non-conservative continuum surface force.

1.3 A mesoscale compressible two-fluid model

The focus so far was on the development and application of numerical simulation to capture the complex fluid dynamics involved in the shock-particle interactions. However, in most engineering applications the computational fluid dynamics study occurs at mesoscale. Thus the next step is to create a model to capture the interaction of shock wave with a particle laden flow in mesoscale based on the results obtained at microscale. Toward this goal, a two-fluid shock and interface capturing scheme is required to solve the phase averaged governing equations.

The finite volume Advection Upstream Splitting Method (AUSM), originally developed by Liou and Steffen [76], and variant of the AUSM-family schemes are known to be excellent at shock and interface capturing while remaining computationally inexpensive and not requiring characteristic analysis. This scheme has been employed successfully by several authors to simulate multiphase flow in different test cases[39], [77], [78]. This scheme has been extended to all-speeds that can be used for low to high Mach number flows [79]. However, these schemes include at least one problem-dependent parameter, such as a cut-off Mach number [80]. This parameter should be a very small, but non-zero, for very low Mach number flows. This approach can be problematic since there is no standard method to define the cut-off Mach number, especially when no uniform flow is present [81].

Recently, a new, simple low-dissipation numerical flux function of the AUSM-family has been developed for all speeds, called the simple low-dissipation AUSM (SLAU) [82], [83]. In contrast with previous all-speed schemes, the simple low-dissipation AUSM features low dissipation without any tunable parameters in a low Mach number regime while maintaining the

robustness of the AUSM-family fluxes against shock-induced anomalies at high Mach numbers (e.g., carbuncle phenomena). Furthermore, the simple low-dissipation AUSM has a simpler formulation than other all-speed schemes [83]–[85]. The advantage of the SLAU scheme has motivated us to extend this scheme to two-phase application. Thus, in this dissertation we develop a two-phase and simple low-dissipation AUSM-family (TSLAU) scheme which is free from reference parameters.

1.4 Thesis organization

This thesis outlines the development and application of numerical methods for the compressible multiphase flow in the gas-solid and gas-liquid regimes. Chapter 2 is a manuscript in preparation for submission to the International Journal of Multiphase Flow (IJMF). This chapter presents the governing equations for particle resolved direct numerical simulation of a gas-solid flow including compressible Navier-Stokes equations and a compressible immersed boundary method to account for particles. In this chapter, several problems are investigated. The problem of shock interaction with a transverse array of particles is studied to reveal the effect of the wave-wave and wave-wake interaction on introducing unsteadiness. Then, the simulation of a multiphase shock tube of Wagner et al.[28] and Regele et al. [1] is performed to investigate and quantify flow unsteadiness in a shock-particle cloud interaction. The vorticity equation budget is calculated to provide insight into the sources of unsteadiness in the particle cloud and the wake behind it. Phasic Favre averaging statistics were calculated to perform detailed analysis of the importance of velocity fluctuations and kinetic energy in the fluctuating field which arise from the strong unsteadiness. An analogous simulation and analysis is presented for the same particle cloud impacted by a gradually induced flow with a compression wave to assesses the importance of impulsive effect of shock by comparison of the two cases.

Chapter 3 is a paper on the development of a flow solver for particle resolved direct numerical simulation of compressible gas-liquid flows. In this chapter the development of a five-equation interface-capturing scheme along with the interface compression scheme to account for the immiscibility condition is explained. The implementation of the surface tension force based on the continuum surface force and curvature calculation are described. Then some results demonstrating the method's capabilities are presented.

Chapter 4 is a paper on the development of a finite volume, parameter free, two-phase and low dissipation AUSM-family (TSLAU) scheme. This includes the presentation of the system of equations for a single-pressure two-fluid model along with the detailed explanation of the extension of this scheme based on the single phase all speed SLAU scheme. Then the details about the temporal discretization, source terms, and equations of state and primitive variable deduction procedures are explained. The method's capabilities are evaluated using a well-known benchmark problem in comparison with the two-phase AUSM$^+$, two phase AUSM$^+$-up.

References

[1] J. D. Regele, J. Rabinovitch, T. Colonius, and G. Blanquart, "Unsteady effects in dense, high speed, particle laden flows," *Int. J. Multiph. Flow*, vol. 61, no. May, pp. 1–13, 2014.

[2] Y. Mehta, T. L. Jackson, J. Zhang, and S. Balachandar, "Numerical investigation of shock interaction with one-dimensional transverse array of particles in air," *J. Appl. Phys.*, vol. 119, no. 10, pp. 0–13, 2016.

[3] Y. Ling, J. L. Wagner, S. J. Beresh, S. P. Kearney, and S. Balachandar, "Interaction of a planar shock wave with a dense particle curtain: Modeling and experiments," *Phys. Fluids*, vol. 24, no. 11, 2012.

[4] Y. Ling, A. Haselbacher, and S. Balachandar, "Importance of unsteady contributions to force and heating for particles in compressible flows: Part 1: Modeling and analysis for shock–particle interaction," *Int. J. Multiph. Flow*, vol. 37, no. 9, pp. 1026–1044, 2011.

[5] H. Tanno, K. Itoh, T. Saito, A. Abe, and K. Takayama, "Interaction of a shock with a sphere suspended in a vertical shock tube," *Shock Waves*, vol. 13, no. 3, pp. 191–200, Nov. 2003.

[6] M. Sun, T. Saito, K. Takayama, and H. Tanno, "Unsteady drag on a sphere by shock wave loading," *Shock Waves*, vol. 14, no. 1–2, pp. 3–9, Jun. 2005.

[7] M. Bredin and B. Skews, "Drag measurements in unsteady compressible flow. Part 1: an unsteady flow facility and stress wave balance. R&D J," *South Afr. Inst. Mech. Eng*, 2007.

[8] L. J. Forney, D. B. Van Dyke, and W. K. McGregor, "Dynamics of Particle—Shock Interactions: Part I: Similitude," *Aerosol Sci. Technol.*, vol. 6, no. 2, pp. 129–141, Jan. 1987.

[9] M. Parmar, A. Haselbacher, and S. Balachandar, "Modeling of the unsteady force for shock–particle interaction," *Shock Waves*, vol. 19, no. 4, pp. 317–329, Aug. 2009.

[10] L. J. Forney, A. E. Walker, and W. K. McGregor, "Dynamics of Particle-Shock Interactions: Part II: Effect of the Basset Term," *Aerosol Sci. Technol.*, vol. 6, no. 2, pp. 143–152, Jan. 1987.

[11] J. Z. P. Sridharan T.L. Jackson and S. Balachandar, "Shock interaction with 1-D array of particles in air," *J. Appl. Phys.*, vol. 117, no. 7, p. 75902, Feb. 2015.

[12] O. Igra and K. Takayama, "Shock Tube Study of the Drag Coefficient of a Sphere in a Non-Stationary Flow," *Proc. R. Soc. London A Math. Phys. Eng. Sci.*, vol. 442, no. 1915, 1993.

[13] E. Loth, "Compressibility and Rarefaction Effects on Drag of a Spherical Particle," *AIAA J.*, vol. 46, no. 9, pp. 2219–2228, Sep. 2008.

[14] A. V. Fedorov, A. V. Shul'gin, and S. V. Poplavski, "Motion of a particle behind the shock wave front," *Combust. Explos. Shock Waves*, vol. 46, no. 2, pp. 207–215, Mar. 2010.

[15] M. Parmar, A. Haselbacher, and S. Balachandar, "Improved Drag Correlation for Spheres and Application to Shock-Tube Experiments," *AIAA Journal*, vol. 48, no. 6. pp. 1273–1276, Jun-2010.

[16] H. Miura and I. I. Glass, "On the Passage of a Shock Wave Through a Dusty-Gas Layer," *Proc. R. Soc. London A Math. Phys. Eng. Sci.*, vol. 385, no. 1788, 1983.

[17] V. M. Boiko, V. P. Kiselev, S. P. Kiselev, a. N. Papyrin, S. V. Poplavsky, and V. M. Fomin, "Shock wave interaction with a cloud of particles," *Shock Waves*, vol. 7, no. 5, pp. 275–285, 1997.

[18] H. Tanno, K. Itoh, T. Saito, A. Abe, and K. Takayama, "Interaction of a shock with a sphere suspended in a vertical shock tube," *Shock Waves*, vol. 13, no. 3, pp. 191–200, Nov. 2003.

[19] H. Miura and I. I. Glass, "On a Dusty-Gas Shock Tube," *Proc. R. Soc. London A Math. Phys. Eng. Sci.*, vol. 382, no. 1783, 1982.

[20] H. Miura, "Decay of shock waves in a dusty-gas shock tube," *Fluid Dyn. Res.*, vol. 6, no. 5–6, pp. 251–259, Dec. 1990.

[21] R. Ripley, F. Zhang, and F. Lien, "Acceleration and heating of metal particles in condensed matter detonation," *Proc. R. Soc. A*, 2012.

[22] L. Svarovsky, *Handbook of powder technology: Solid-Gas Separation*. 1981.

[23] S. Hank, R. Saurel, and O. Le Metayer, "A Hyperbolic Eulerian Model for Dilute Two-Phase Suspensions," *J. Mod. Phys.*, vol. 2, no. 9, pp. 997–1011, 2011.

[24] M. S. Baer and J. W. Nunziato, "A two-phase mixture theory for the deflagration to detonation (DDT) transition in reactive granular materials," *Int. J. Multiph. Flow*, vol. 12, no. 6, pp. 861–889, 1986.

[25] M. R. Baer, "Continuum Mixture Modeling of Reactive Porous Media," in *High-Pressure Shock Compression of Solids IV*, New York, NY: Springer New York, 1997, pp. 63–82.

[26] S. A. Sheffield, R. R. Alcon, R. L. GustavsenR A Graham, M. U. Anderson, and R. A. Graham, "Particle velocity and stress measurements in low density HMX," *AIP Conf. Proc.*, vol. 309, 1994.

[27] R. W. Houim and E. S. Oran, "A Technique for Computing Dense Granular Compressible Flows with Shock Waves," *Jcp*, 2013.

[28] J. L. Wagner *et al.*, "A multiphase shock tube for shock wave interactions with dense particle fields," *Exp. Fluids*, vol. 52, no. 6, pp. 1507–1517, 2012.

[29] R. Clift and W. H. Gauvin, "Motion of entrained particles in gas streams," *Can. J. Chem. Eng.*, vol. 49, no. 4, pp. 439–448, Aug. 1971.

[30] T. G. Theofanous and C. H. Chang, "The dynamics of dense particle clouds subjected to shock waves. Part 1. Experiments and scaling laws," *J. Fluid Mech*, vol. 89, pp. 177–206, 2016.

[31] T. G. Theofanous and C. H. Chang, "The dynamics of dense particle clouds subjected to shock waves. Part 2. Modeling/numerical issues and the way forward," *Int. J. Multiph. Flow*, vol. 89, pp. 177–206, 2017.

[32] J. L. Wagner, S. P. Kearney, S. J. Beresh, E. P. DeMauro, and B. O. Pruett, "Flash X-ray measurements on the shock-induced dispersal of a dense particle curtain," *Exp. Fluids*, vol. 56, no. 12, pp. 1–12, 2015.

[33] M. K. Parmar, A. Haselbacher, and S. Balachandar, "Prediction and Modeling of Shock-Particle Interaction," *47th AIAA Aerosp. Sci. Meet.*, 2009.

[34] J. L. Wagner, S. J. Beresh, S. P. Kearney, B. O. M. Pruett, and E. K. Wright, "Shock tube investigation of quasi-steady drag in shock-particle interactions," *Phys. Fluids*, vol. 24, no. 12, p. 123301, Dec. 2012.

[35] J. C. Meng and T. Colonius, "Numerical simulations of the early stages of high-speed droplet breakup," *Shock Waves*, vol. 25, no. 4, pp. 399–414, Jul. 2015.

[36] E. Johnsen and T. Colonius, "Compressible Multicomponent Flow Calculations and Shock-Bubble Interaction," no. September, 2006.

[37] B. E. Gel'fand, S. A. Gubin, S. M. Kogarko, and S. P. Komar, "Singularities of the breakup of viscous liquid droplets in shock waves," *J. Eng. Phys.*, vol. 25, no. 3, pp. 1140–1142, Sep. 1973.

[38] M. W. Evans, F. H. Harlow, and B. D. Meixner, "Interaction of Shock or Rarefaction with a Bubble," *Phys. Fluids*, vol. 5, no. 6, p. 651, 1962.

[39] C. H. Chang and M. S. Liou, "A robust and accurate approach to computing compressible multiphase flow: Stratified flow model and AUSM+-up scheme," *J. Comput. Phys.*, vol. 225, no. 1, pp. 840–873, 2007.

[40] E. Johnsen *et al.*, "Assessment of high-resolution methods for numerical simulations of compressible turbulence with shock waves," *J. Comput. Phys.*, vol. 229, no. 4, pp. 1213–1237, Feb. 2010.

[41] V. Coralic and T. Colonius, "Finite-volume WENO scheme for viscous compressible multicomponent flows," *J. Comput. Phys.*, vol. 274, pp. 95–121, 2014.

[42] S. O. Unverdi and G. Tryggvason, "A front-tracking method for viscous, incompressible, multi-fluid flows," *J. Comput. Phys.*, vol. 100, no. 1, pp. 25–37, May 1992.

[43] J. Glimm, J. W. Grove, X. L. Li, K. Shyue, Y. Zeng, and Q. Zhang, "Three-Dimensional Front Tracking," *SIAM J. Sci. Comput.*, vol. 19, no. 3, pp. 703–727, May 1998.

[44] H. Terashima and G. Tryggvason, "A front-tracking method with projected interface conditions for compressible multi-fluid flows," *Comput. Fluids*, vol. 39, no. 10, pp. 1804–1814, 2010.

[45] H. Terashima and G. Tryggvason, "A front-tracking/ghost-fluid method for fluid interfaces in compressible flows," *J. Comput. Phys.*, vol. 228, no. 11, pp. 4012–4037, Jun. 2009.

[46] B. Wang and H. Xu, "A Method Based on Riemann Problem in Tracking Multi-Material Interface On Unstructured Moving Grids," *Eng. Appl. Comput. Fluid Mech.*, vol. 1, no. 4, pp. 325–336, Jan. 2007.

[47] H. Luo, J. D. Baum, and R. Löhner, "On the computation of multi-material flows using ALE formulation," *J. Comput. Phys.*, vol. 194, no. 1, pp. 304–328, 2004.

[48] S. Fechter and C. D. Munz, "A discontinuous Galerkin based sharp-interface method to simulate three-dimensional compressible two-phase flow," *Int. J. Numer. Methods Fluids*, vol. 78, no. 7, pp. 413–435, Jul. 2015.

[49] W. Mulder, S. Osher, and J. A. Sethian, "Computing interface motion in compressible gas dynamics," *J. Comput. Phys.*, vol. 100, no. 2, pp. 209–228, Jun. 1992.

[50] T. G. Liu, B. C. Khoo, and K. S. Yeo, "Ghost fluid method for strong shock impacting on material interface," *J. Comput. Phys.*, vol. 190, no. 2, pp. 651–681, 2003.

[51] R. Abgrall and S. Karni, "Computations of Compressible Multifluids," *J. Comput. Phys.*, vol. 169, no. 2, pp. 594–623, May 2001.

[52] R. R. Nourgaliev and T. G. Theofanous, "High-fidelity interface tracking in compressible flows: Unlimited anchored adaptive level set," *J. Comput. Phys.*, vol. 224, no. 2, pp. 836–866, 2007.

[53] E. Olsson, G. Kreiss, and S. Zahedi, "A conservative level set method for two phase flow II," *J. Comput. Phys.*, vol. 225, no. 1, pp. 785–807, 2007.

[54] R. Saurel and R. Abgrall, "A Simple Method for Compressible Multifluid Flows," *SIAM J. Sci. Comput.*, vol. 21, no. 3, pp. 1115–1145, Jan. 1999.

[55] K.-M. Shyue, "An Efficient Shock-Capturing Algorithm for Compressible Multicomponent Problems," *J. Comput. Phys.*, vol. 142, no. 1, pp. 208–242, May 1998.

[56] G. Allaire, S. Clerc, and S. Kokh, "A Five-Equation Model for the Simulation of Interfaces between Compressible Fluids," *J. Comput. Phys.*, vol. 181, no. 2, pp. 577–616, Sep. 2002.

[57] E. Johnsen and T. Colonius, "Implementation of WENO schemes in compressible multicomponent flow problems," *J. Comput. Phys.*, vol. 219, no. 2, pp. 715–732, 2006.

[58] S. K. Shankar, S. Kawai, and S. K. Lele, "Numerical Simulation of Multicomponent Shock Accelerated Flows and Mixing using Localized Artificial Diffusivity Method," *AIAA Pap. 2010-352*, no. January, p. 2010, Jan. 2010.

[59] S. Kawai, S. K. Shankar, and S. K. Lele, "Assessment of localized artificial diffusivity scheme for large-eddy simulation of compressible turbulent flows," *J. Comput. Phys.*, vol. 229, no. 5, pp. 1739–1762, Mar. 2010.

[60] S. Kawai and S. Lele, "Localized artificial viscosity and diffusivity scheme for capturing discontinuities on curvilinear and anisotropic meshes," *Annu. Res. Briefs*, no. Eccomas, pp. 6–7, 2007.

[61] R. K. Shukla, C. Pantano, and J. B. Freund, "An interface capturing method for the simulation of multi-phase compressible flows," *J. Comput. Phys.*, vol. 229, no. 19, pp. 7411–7439, 2010.

[62] A. Tiwari, J. B. Freund, and C. Pantano, "A diffuse interface model with immiscibility preservation," *J. Comput. Phys.*, vol. 252, pp. 290–309, 2013.

[63] R. K. Shukla, "Nonlinear preconditioning for efficient and accurate interface capturing in simulation of multicomponent compressible flows," *J. Comput. Phys.*, vol. 276, pp. 508–540, 2014.

[64] S. Heister, M. Rutz, and J. Hilbing, "Effect of acoustic perturbations on liquid jet atomization," in *31st Joint Propulsion Conference and Exhibit*, 1995.

[65] S. D. Heister and A. R. Karagozian, "Gaseous jet in supersonic crossflow," *AIAA J.*, vol. 28, no. 5, pp. 819–827, May 1990.

[66] C. F. Chenault, P. S. Beran, and R. D. W. Bowersox, "Numerical investigation of supersonic injection using a Reynolds-stress turbulence model," *AIAA J.*, vol. 37, no. 10, pp. 1257–1269, Oct. 1999.

[67] D. M. Peterson, P. K. Subbareddy, and G. V. Candler, "Assessment of Synthetic Inflow Generation for Simulating Injection Into a Supersonic Crossflow," *14th AIAA/AHI Sp. Planes Hypersonic Syst. Technol. Conf.*, 2006.

[68] A. Ferrante, G. Matheou, and P. E. Dimotakis, "LES of an inclined sonic jet into a turbulent crossflow at Mach 3.6," *J. Turbul.*, vol. 12, no. October 2014, p. N2, Jan. 2011.

[69] K. Mahesh, "The Interaction of Jets with Crossflow," *Annu. Rev. Fluid Mech.*, vol. 45, no. 1, pp. 379–407, Jan. 2013.

[70] J. C. Meng and T. Colonius, "Numerical simulations of the early stages of high-speed droplet breakup," *Shock Waves*, vol. 25, no. 4, pp. 399–414, Jul. 2015.

[71] D. Gueyffier, J. Li, A. Nadim, R. Scardovelli, and S. Zaleski, "Volume-of-Fluid Interface Tracking with Smoothed Surface Stress Methods for Three-Dimensional Flows," *J. Comput. Phys.*, vol. 152, no. 2, pp. 423–456, Jul. 1999.

[72] J. . Brackbill, D. . Kothe, and C. Zemach, "A continuum method for modeling surface tension," *J. Comput. Phys.*, vol. 100, no. 2, pp. 335–354, Jun. 1992.

[73] V.-T. Nguyen, J. Peraire, B. C. Khoo, and P.-O. Persson, "A discontinuous Galerkin front tracking method for two-phase flows with surface tension," *Comput. Fluids*, vol. 39, no. 1, pp. 1–14, 2010.

[74] B. Braconnier and B. Nkonga, "An all-speed relaxation scheme for interface flows with surface tension," *J. Comput. Phys.*, vol. 228, no. 16, pp. 5722–5739, 2009.

[75] G. Perigaud and R. Saurel, "A compressible flow model with capillary effects," *J. Comput. Phys.*, vol. 209, no. 1, pp. 139–178, 2005.

[76] M. Liou, "A Sequel to AUSM: AUSM," *J. Comput. Phys.*, vol. 129, pp. 364–382, 1996.

[77] Y. Y. Niu, Y. C. Lin, and C. H. Chang, "A further work on multi-phase two-fluid approach for compressible multi-phase flows," *Int. J. Numer. Methods Fluids*, 2008.

[78] M. M.-S. Liou, L. Nguyen, T. G. Theofanous, C. C.-H. Chang, L. Nguyen, and T. G. Theofanous, "How to Solve Compressible Multifluid Equations: a Simple, Robust, and Accurate Method," *AIAA J.*, vol. 46, no. 9, pp. 2345–2356, Sep. 2008.

[79] M. S. Liou, "A sequel to AUSM, Part II: AUSM+-up for all speeds," *J. Comput. Phys.*, vol. 214, no. 1, pp. 137–170, 2006.

[80] E. Shima and K. Kitamura, "On New Simple Low-Dissipation Scheem of AUSM-Family for All Speeds," *AIAA Pap.*, no. January, pp. 1272–2010, 2010.

[81] K. Kitamura, E. Shima, Y. Nakamura, and P. L. Roe, "Evaluation of Euler Fluxes for Hypersonic Heating Computations."

[82] K. Kitamura, "New approaches for computation of low Mach number flows," *Comput. Fluids*, vol. 85, pp. 143–152, 2013.

[83] E. Shima and K. Kitamura, "Parameter-Free Simple Low-Dissipation AUSM-Family Scheme for All Speeds," *AIAA J.*, vol. 49, no. 8, pp. 1693–1709, Aug. 2011.

[84] K. Kitamura, E. Shima, Y. Nakamura, and P. L. Roe, "Evaluation of Euler Fluxes for Hypersonic Heating Computations," *AIAA J.*, vol. 48, no. 4, pp. 763–776, Apr. 2010.

[85] K. Chakravarthy and D. Chakraborty, "Modified SLAU2 scheme with enhanced shock stability," *Comput. FLUIDS*, vol. 100, pp. 176–184, 2014.

CHAPTER 2. INVESTIGATION AND QUANTIFICATION OF FLOW UNSTEADINESS IN SHOCK-PARTICLE CLOUD INTERACTION

A paper in preparation for international journal of multiphase flow

Zahra Hosseinzadeh-Nik[1], Shankar Subramaniam[2], Jonathan D. Regele[3]

Abstract

This work aims to study the interaction of a shock wave with a cloud of particles to quantify flow unsteadiness and velocity fluctuations using particle-resolved direct numerical simulation (PR-DNS). Three cases are studied, with each case revealing one aspect of the intricate flow phenomena involved in this interaction. The unsteady interaction of a shock wave with a transverse array of particles reveals the origin of unsteadiness under the effect of mutual wave-wave and wave-wake interactions between the particles. In the second case, the interaction of a shock with a particle cloud is studied, with a focus on the interaction of the complex wave system with the vortical structure. A budget analysis of the vorticity equation reveals the sources of strong unsteadiness in the particle cloud. A detailed analysis of the velocity fluctuation and kinetic energy in the fluctuating motion is performed to ascertain the importance of the velocity fluctuations that arise from the strong unsteadiness. An analogous analysis is presented, in the third case, for a gradually induced flow on the same particle cloud along with a comparison to the shock induced case to assess the impulsive effect of shock on intensity of the fluctuating field statistics.

[1] PhD candidate, Department of Aerospace Engineering and Mechanical Engineering, Iowa State University.
[2] Professor, Department of Mechanical Engineering, Iowa State University.
[3] Assistant Professor, Department of Aerospace Engineering, Iowa State University.

2.1 Introduction

The interaction between shock waves and particles is an important phenomenon in compressible particle-laden flows [1]–[5]. When a shock wave propagates around a particle a complex wave system including regular and irregular shock-wave reflection and diffraction is established [6]–[8].

Shock interaction with a single isolated particle has been studied extensively [6], [7], [9], [10]. In many typical applications, shock waves interact with a cloud or dispersion of particles [8], [11], [12]. In these processes, depending on the solid phase volume fraction, α_s, the flow topology ranges from a very dense gas-solid flow ($\alpha_s \geq 0.5$) during the propagation of the shock wave within the particle cloud to a dilute gas-solid flow ($\alpha_s < 0.01$), at distances far from the source. Between these two extremes ($0.01 < \alpha_s < 0.5$), there exists a dense gas-solid flow regime during early interaction times. A detailed discussion of these three regimes is given by Zhang et al. [13].

The modeling techniques developed for an isolated particle are suitable for dilute particle-laden flows (i.e., with negligible particle volume fraction), but cannot be applied directly in dense particle-laden flows (i.e., with finite particle volume fraction) [8]. With increasing particle volume fraction, the existence of neighboring particles further complicates the interaction between shock waves and particles. In these situations, inter-particle interactions, interactions between particles and reflected or diffracted waves from neighboring particles, and interactions between particles and the wakes of neighboring particles become important.

Much experimental work in the dilute regime has been conducted[14]–[16]. Simulations and theoretical analysis have been applied to predict shock attenuation in this regime[17], [18]. Computational modeling has also shown the capability to capture the gas–solid flow physics in the

very dense regime. For instance, Baer and Nunziato [19] use continuum mixture theory to accurately model the normal shock impingement. However, there is a substantial knowledge gap in gas–solid flows with intermediate particle volume fractions that are roughly equivalent to those found in dense gas–solid flow. Thus, detailed knowledge of the interactions that occur in dense gas–solid flow is required [5], [8], [20], [21].

On the other hand, shock–particle interaction is strongly time-dependent[4], [22]. The particle is subjected to very strong gas acceleration as the shock wave passes over it [21], [23]. Sun et al. [9] and Bredin and Skews [24] presented time-resolved measurements of the force on a stationary particle subjected to a shock wave. The instantaneous force on the particle under such highly unsteady conditions was shown to be much larger than the corresponding quasi-steady force that would have resulted if the change from the quiescent pre-shock state to the uniform post-shock state were to happen very slowly [4], [8]. In particular, the instantaneous force during the passage of the shock wave is reported to be an order of magnitude larger than the steady drag force resulting from the post-shock gas velocity [5]. This clearly highlights the importance of unsteady effects in shock–particle interactions.

The unsteady effects are usually neglected even if strong interactions between compressible flow features and particles are to be expected [13], [25], [26]. However, in some applications, such as in detonations, the large unsteady forces exerted on the particle can cause deformation and breakage. Similarly, intense unsteady heating can cause melting or initiate chemical reactions. There are a limited number of papers that address the influence of unsteady forces on the motion of particles interacting with a shock wave, such as Parmar et al. [10] and Forney et al. [2]. Ling et al. [5], [8] also proposed a model that includes unsteady contributions to force and heating. They have also developed a one-dimensional phase-averaged point-particle model including the

unsteady momentum coupling forces to reproduce the experimental results of Wagner et al.[21]. This result highlights the importance of unsteadiness in the shock-particle interaction in the dense gas-solid regime.

Although this model is promising, it is appropriate to question whether all aspects of the experimental flow can be captured using a one-dimensional model that only includes the unsteady momentum coupling forces. Regele et al. [27] performed 2D simulations using the Euler equations and observed high flow unsteadiness. They compared the results with a 1D model and indicated that the 1D model can characterize the overall steady-state flow behavior but fails to capture unsteady behavior due to neglect of unsteady terms such as Reynolds stress. There is also evidence that the Reynolds stress can be important in simple homogeneous incompressible flow in the dense particle-laden regime [28], [29]. In these results, the inter-particle interactions, the interactions between particles and the wakes of neighboring particles play a role. However, the interactions between particles and the reflected or diffracted waves from neighboring particles is absent. Even in the absence of shocks, Mehrabadi et al. [28] showed that the Reynolds stress term is non-negligible and fluctuations in the gas-phase velocity can contribute significantly to the total gas-phase kinetic energy. Furthermore, the authors denote local particle-scale gas-phase velocity fluctuations generated by the presence of particles, larger than the Kolmogorov length scale, as pseudo-turbulent velocity fluctuations. They refer to the kinetic energy associated with these fluctuations as the pseudo-turbulent kinetic energy (PTKE) because these fluctuations can be generated even in laminar gas-solid flow. They show that the PTKE in the fluctuating motion can be as high as the kinetic energy in the mean flow, especially for systems with higher solid volume fractions. The ratio of PTKE to mean kinetic energy increases with the solid volume fraction and decreases with the mean slip Reynolds number. This provides evidence that the pseudo-turbulent

effects play an important role in the dense gas-solid regime. Sun et al. [29] provided evidence that the velocity fluctuations can also result in temperature fluctuations. Regele et al. [27] showed that velocity fluctuations from shock-particle interactions are more significant and can be on the same order as the mean velocity. However, since the calculations were performed with the Euler equations, additional studies including viscous and thermal diffusion are required to more accurately quantify the magnitude of the velocity fluctuations. These observations along with the experimental results of Wagner et al.[21] indicate that quantification of the unsteadiness and gas-phase velocity fluctuation in the shock-particle cloud interaction is necessary to better understand the flow interaction.

The overarching goal of this paper is to quantify the flow unsteadiness and velocity fluctuations induced by shock waves interacting with particle-clouds and determine their sources. The approach is to perform 2-D simulations of shock waves impacting an array or cloud of particles, where the same conditions used in Regele et al. [27] will be used for the particle cloud. The fully compressible Navier-Stokes equations are solved, which provides a more accurate estimate of the magnitude of these terms than the previous Euler simulations [27]. A transverse array of particles is used to obtain deeper insight into the wave dynamics and unsteady vortex generation on each particle under the mutual wave-wave and wave-wake interaction between the particles. Quantification of the shock-particle cloud interaction highlights the impact of the complex shock dynamics that arise from the effect of neighboring particles on the mean and fluctuating flow field evolution. These results are then compared against a gradually induced flow over the same particle cloud, to remove the impulsive effect of the shock and understand how the impulsive shock dynamics contribute to the unsteadiness and the fluctuating field statistics.

The paper is organized as follows. The mathematical approach and the numerical methods are presented in Sections 2.2 and 2.3 respectively. The results for a shock wave impacting a transverse array of particles are contained in Section 0 and the results describing the particle cloud behavior are in Section 2.3.2. Finally, conclusions are drawn in Section 2.6.

2.2 Mathematical approach

2.2.1 Governing equations for PR-DNS

In this work the interaction of shock and compression waves with particles are studied where the particles are frozen in place because of the large density ratio between the two phases [27]. In these interactions the smallest scale flow feature, other than the shock thickness, is the boundary layer present near the surface of each particle. The appropriate method to accurately capture these flow features is the Particle-Resolved Direct Numerical Simulation (PR-DNS) methodology in which the flow scales, introduced by the presence of large particles, are resolved [28], [29]. To this end, the fully compressible Navier-Stokes equations are solved to ensure the accuracy of the captured features in the cloud and the wake structure behind the cloud. The non-dimensionalized continuity, momentum and energy equations in conservative form are

$$\frac{\partial \rho}{\partial t} + \frac{\partial (\rho u_i)}{\partial x_i} = 0 \tag{2-1}$$

$$\frac{\partial (\rho u_i)}{\partial t} + \frac{\partial \left(\rho u_i u_j\right)}{\partial x_j} = -\frac{\partial p}{\partial x_i} + \frac{1}{Re_a}\frac{\partial \left(\tau_{ij}\right)}{\partial\, x_j} \tag{2-2}$$

$$\frac{\partial (\rho E)}{\partial t} + \frac{\partial}{\partial x_j}\left[(\rho E + p)u_j\right] = \frac{1}{Re_a}\frac{\partial \left(u_i \tau_{ij}\right)}{\partial x_j} + \frac{1}{(\gamma - 1)Re_a Pr}\frac{\partial}{\partial x_j}\left(k\frac{\partial T}{\partial x_j}\right) \tag{2-3}$$

where the velocity, u_i, is non-dimensionalized by a reference speed of sound c_0, time (t) by l/c_0, total energy (E) by c_0^2, density (ρ) by ρ_0, pressure (p) by $\rho_0 c_0^2$, viscosity (μ) by μ_0, thermal conductivity (k) by k_0 , and temperature (T) by T_0. All quantities with subscript "0" denote the

reference state, which is the undisturbed gas state. The Prandtl number ($Pr = \mu_0 c_{p0}/k_0$) is defined as the ratio of the momentum diffusivity to thermal diffusivity. Re_a is the acoustic Reynolds number determined by the characteristic length scale, l,

$$Re_a = \frac{\rho_0 c_0 l}{\mu_0}. \tag{2-4}$$

The non-dimensional equation of state is

$$p = (\gamma - 1)\rho\left(E - \frac{1}{2}u_i u_i\right). \tag{2-5}$$

The non-dimensional stress tensor, τ_{ij}, is expressed as

$$\tau_{ij} = \mu\left(\frac{\partial u_i}{\partial x_j} + \frac{\partial u_j}{\partial x_i} - \frac{2}{3}\frac{\partial u_k}{\partial x_k}\delta_{ij}\right), \tag{2-6}$$

and the temperature is found using a non-dimensionalized ideal gas equation of state

$$T = \gamma p/\rho \tag{2-7}$$

with $\gamma = 1.4$. The temperature dependence of viscosity, μ, is assumed to follow Sutherland's law[30]

$$\mu = \frac{1 + S_1}{T + S_1} T^{1.5} \tag{2-8}$$

where S_1 is Sutherland constant normalized by T_0 and has the value of 0.4.

2.2.2 Immersed Boundary method

Particle Resolved DNS coupled with immersed boundary methods is a common approach used to study particle scale fluid dynamics [28], [31]–[34]. However, most of these approaches are based on incompressible formulations. Recently, Brown-Dymkoski et al. [35] developed an immersed boundary method for compressible flow based on the extension of Brinkman Penalization Method that allow any arbitrary Dirichlet, Neumann, or Robin-type boundary

condition and has been applied to several validation test cases [35] in the Adaptive Wavelet Collocation framework (explained in the next section). In this work, the immersed boundary method developed by Brown-Dymkoski et al. [35] is used to impose adiabatic no slip conditions at particle surfaces. The penalization equations are:

$$\frac{\partial \rho}{\partial t} = (1-\chi)RHS - \frac{\chi}{\eta_c}\left(n_k \frac{\partial \rho}{\partial x_k} - \phi\right) \tag{2-9}$$

$$\frac{\partial \rho u_i}{\partial t} = (1-\chi)RHS - \chi\left[\frac{1}{\eta_b}\rho(u_i - u_{0i}) + \rho \nu_n \frac{\partial^2 u_i}{\partial x_j \partial x_j} + \frac{u_i}{\eta_c}\left(n_k \frac{\partial \rho}{\partial x_k} - \phi\right)\right] \tag{2-10}$$

$$\begin{aligned}\frac{\partial \rho E}{\partial t} = (1-\chi)RHS \\ - \chi\left[\frac{1}{\eta_c}\left(n_k \frac{\partial \rho E}{\partial x_k}\right) + \frac{1}{\eta_b}\rho(u_j - u_{0j})u_j - \frac{1}{\eta_c}\rho u_j n_k \frac{\partial u_j}{\partial x_k}\right. \\ \left. - \rho u_j \nu_n \frac{\partial^2 u_i}{\partial x_j \partial x_j} - \frac{1}{\eta_c} E\phi \; - \frac{1}{\eta_c c_v \rho q}\right]\end{aligned} \tag{2-11}$$

where χ is a mask function that is unity inside the object and zero outside, RHS indicates the right-hand side of the Navier-Stokes equations, and n_k is the inward facing surface normal of the object. The interior of the particles are governed by the penalization terms, while outside the particles, the equations are the same as the Navier-Stokes equations. The velocity u_{0j} is the velocity of the object, which for this work is zero. The parameters η_c, η_b, and ν_n control the accuracy and numerical stability as described in Ref. [35]. In the penalization for ρ, the quantity ϕ is governed by the equation

$$\frac{\partial \phi}{\partial t} = -\frac{\chi}{\eta_c} n_k \frac{\partial \phi}{\partial x_k} \tag{2-12}$$

where this quantity is passively controlled by the fluid physics and allows a Neumann condition on density, ρ. The error from these penalized boundary condition converges as $O(\eta_c, \eta_b^{0.5})$.

2.3 Numerical Approach

In order to perform a particle-resolved direct numerical simulation of shock-particle interaction, high resolution is required to fully resolve the flow features around the particles and shock waves. However, high resolution is not required homoegenously throughout the domain. Thus, an adaptive grid framework based on the parallel adaptive wavelet collocation method (PAWCM) is used to perform the simulations. The PAWCM is based on second-generation wavelets [36]–[39] and determines the grid points necessary to represent a solution based on a prescribed error threshold parameter ϵ and maximum level of resolution j. This allows a solution to be represented with a prescribed level of accuracy on much fewer grid points than what is traditionally necessary.

The hyperbolic solver developed for the PAWCM [40] is used to capture the wave structures and maintain numerical stability. This method is first order accurate near discontinuities such as shock waves and has higher accuracy in continuous regions. The spatial discretization in the continuous regions uses fourth-order finite-differencing and the time integration is based on the Crank-Nicolson method.

2.3.1 Averaging Method

To quantify flow unsteadiness and understand the significance of velocity fluctuations, mean flow statistics must be calculated. The phase average quantities of the gas phase, $\langle Q \rangle$ are obtained using

$$\langle Q \rangle = \frac{1}{V} \int_V Q dV \tag{2-13}$$

where V is the sampling volume in the gas phase. In the 2D simulations performed in this work, the sampling volume becomes a sampling area. The sampling area (V) is as thin as 3 cells in the

x-direction and spans the entire domain height in the y-direction. This equation is used to obtain the mean pressure and density at each x-position. The Favre average of a quantity Q is defined as

$$\tilde{Q} = \frac{\int_V \rho Q dV}{\int_V \rho dV} = \frac{\langle \rho Q \rangle}{\langle \rho \rangle} \tag{2-14}$$

2.3.2 Validation and drag force

The evolution of the unsteady drag coefficient during the early interaction of a shock wave with a single particle is studied to replicate the experiment of Abe et al. [41] and validate the flow solver. In this interaction, the shock Mach number, M, has the magnitude of 1.7 and is defined as the ratio of slip velocity to the local speed of sound. The particle Reynolds number based on the particle diameter, D is considered to be 2.5×10^5 and is defined as

$$Re_p = \frac{\rho_s u_s D}{\mu_s} \tag{2-15}$$

The particle Reynolds number is proportional to the acoustic Reynolds number for the non-dimensional governing equations, Eq.(2-9) to (2-11) by,

$$Re_a = Re_p \left(\frac{\rho_0}{\rho_s}\right)\left(\frac{1}{M}\right)\left(\frac{\mu_0}{\mu_s}\right), \tag{2-16}$$

where subscript s denotes the post-shock condition.

The jump condition is defined using

$$Q = Q_s - 0.5(Q_s - Q_0)\left[1 + \tanh\left(\frac{x_i - x_{i0}}{\delta/2}\right)\right] \tag{2-17}$$

where $Q = \{\rho, u, T\}$ is the vector of primitive variables with ρ being the density, u the velocity, and T the temperature. The post-shock conditions $Q_s = \{2.20, 0.93, 1.46\}$ and pre-shock conditions $Q_0 = \{1, 0, 1\}$ are prescribed using Rankine–Hugoniot jump conditions. The simulation is performed for a particle located at the origin with non-dimensional diameter, $D = 1$, in a

rectangular computational domain of $(X \times Y) = [-L, L] \times [-0.5L, 0.5L]$, where $L/D = 11.4$. The initial shock location is $x_{i0} = -0.52\text{D}$ and the jump transition distance is $\delta = 10^{-4}D$. The undisturbed air downstream of the planar shock is initially at rest ($u_0 = 0$). The post-shock condition is prescribed at the inlet and non-reflecting boundary conditions are imposed on other faces.

The unsteady drag coefficient is calculated using

$$C_D = \frac{\vec{F} \cdot \hat{e}_i}{0.5\rho_s u_s^2 A} \tag{2-18}$$

where $\vec{F}$ is the force acting on the particle and $\hat{e}_i$ is the unit vector in the streamwise direction, ρ_s is the post-shock density, u_s is the corresponding post-shock velocity and A is the cross-section of the particle, which is equal to the particle diameter in the 2D simulation [42], [43]. The force components are obtained using the integral over the outer surface of the particle ($\delta\Omega$)

$$F_i = \iint_{\delta\Omega} f_i dS \tag{2-19}$$

where $f_i = \sigma_{ij} n_j$ is the force acting on a differential surface dS, n_j is the outward pointing normal and $\sigma_{ij} = -p\,\delta_{ij} + \tau_{ij}$ is the total stress tensor. The surface integral is changed to a volume integral using the divergence theorem. To approximate the volume integral on a discrete grid, a summation over all grid points (k) inside the particle of volume Ω is used [44]

$$F_i = \iiint_{\Omega} \frac{\partial \sigma_{ij}}{\partial x_j} dV \approx \sum_{k \in \Omega} \left(\frac{\partial \sigma_{ij}}{\partial x_j} \right)_k \Delta V_k. \tag{2-20}$$

Figure 2-1 compares the evolution of the unsteady drag coefficient over the particle obtained from the numerical solution, with the number of points per particle $N_p = 176$, against the

experimental results reported by Abe et al. [41]. Time is non-dimensionalized by the acoustic time of the particle τ_d, which is the ratio of the particle diameter (D) over the speed of sound of the undisturbed gas (c_0). The unsteady drag coefficient experiences a maximum after being impacted by the shock. The magnitude of the maximum drag and the drag profile over time obtained from simulation are in good agreement with the experimental counterpart.

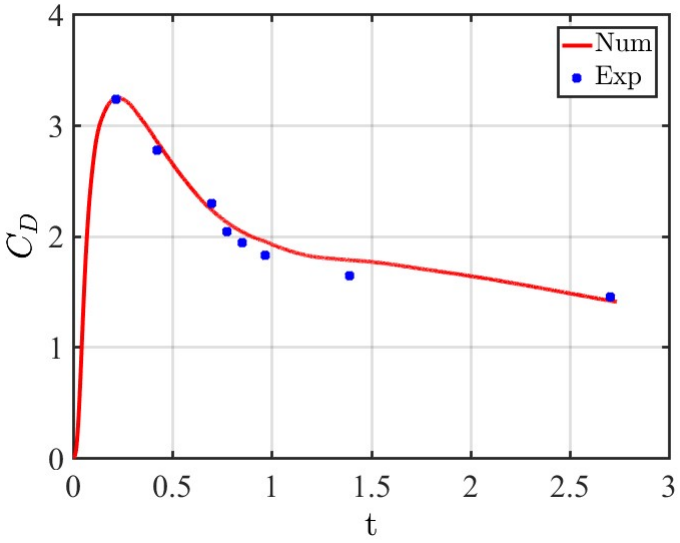

Figure 2-1 Comparison of the unsteady drag force obtained from the numerical results with the experimental data of Abe et al. [41]

2.4 Shock impacting a transverse array of particles

In this problem, the formation of the complex wave structure due to wave-wave interaction between the wave systems of neighboring particles, the wave-wake interaction between this complex wave system and the wake behind each particle, the evolution of local supersonic zones (LSZs), defined by Xu et. al [45], over the wake of each particle and the onset of unsteadiness under these interactions is discussed.

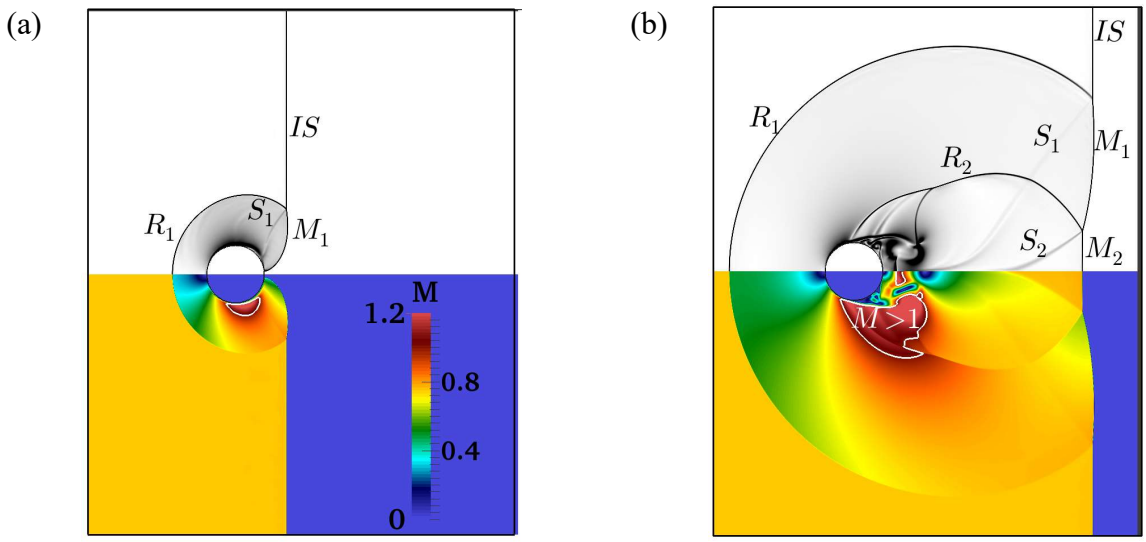

Figure 2-2 Initial evolution of the wave system around each particle at $t = 0.83$ and $t = 2.77$. Top: The numerical Schlieren image. Bottom: Mach number contour. Local supersonic zones, represented with sonic lines, are shown on top and bottom of the particle.

To simulate the shock interaction with a transverse array of particles, we consider the particle array as periodic images of a unit cell consisting of one particle with non-dimensional diameter $D = 1$, in a computational domain of $(X \times Y) = [-1.5L, L] \times [-0.5L, 0.5L]$, with $L/D = 11.4$ and impose periodic boundary conditions in the transverse direction. The particle diameter is considered to be the characteristic length scale. The transverse particle spacing between the adjacent particles (Δ) is equal to L. The shock Mach number is 1.67. The jump condition is defined using Eq. (2-17) with the post-shock conditions $Q_s = \{\rho, u, T\}_s = \{2.14, 0.89, 1.44\}$ and pre-shock conditions $Q_0 = \{\rho, u, T\}_0 = \{1, 0, 1\}$. The shock wave is initially located at a non-dimensional axial location $x_{i0} = -0.52$D and the particle is located at the origin. The undisturbed air downstream of the planar shock is initially at rest ($u_0 = 0$). For this problem, the post-shock condition is prescribed at the inlet ($x_{in} = -1.5L$) and a non-reflecting boundary condition [46] is imposed as the outlet condition (at $x_{in} = L$). Similar to the validation case, time is non-dimensionalized by the acoustic time of the particle τ_d.

Figure 2-2 depicts the initial evolution of the wave system around the particle in a unit cell at two non-dimensional times $t = 0.83$ and $t = 2.77$. The top half contains numerical Schlieren images using the density gradient and the bottom half is colored by the flow Mach number. Similar to other works [32], [47]–[51], we first observe the formation of an upper shock wave system consisting of the incident shock (IS), the reflected shock (R_1), the slip surface (S_1), and the Mach stem (M_1) at the early time of interaction in Figure 2-2 a. Then, as illustrated in Figure 2-2b, when the shock propagates further downstream the Mach stem is reflected at the plane of symmetry and the lower shock-wave system is formed. This consists of the Mach stem of the upper system (M_1), a second reflected shock wave (R_2), a second slip surface (S_2), and a second Mach stem (M_2). Figure 2-2 also shows that a local supersonic zone (LSZ), presented by sonic contour lines ($M = 1$), forms on the particle due to flow acceleration and grow over the boundary layer and wake behind the particle.

As the incident shock propagates downstream, the wave system of the particle grows toward the cell boundary and starts to interact with the wave system of the neighboring particles in the adjacent cell in the transverse direction. Figure 2-3 shows the time evolution using numerical Schlieren images of the two neighboring particles in the adjacent cells. The wave-wave interaction, which is the mutual interaction between the wave systems of the two neighboring particles, is shown in Figure 2-3a. In Figure 2-3b the incident shock (IS) and Mach stems (M_1) and (M_2) of both particles superimpose to form the transmitted shock (TS). As shown in Figure 2-3c, the wave-wake interaction starts once the reflected shocks reach the wake behind the particles.

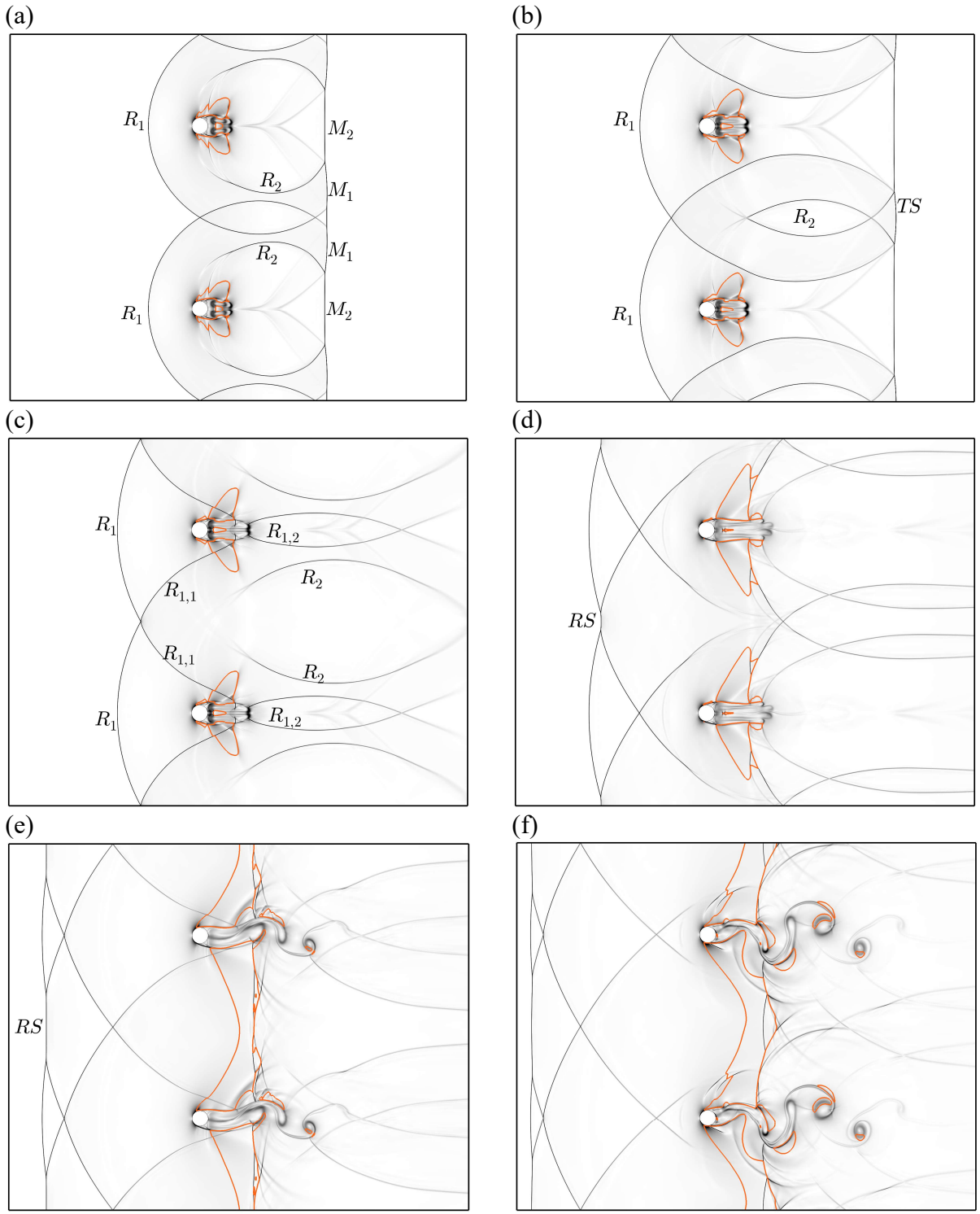

Figure 2-3 Wave-wave and wave-wake interaction between the neigbouring particles in two adjacent cells presented by the time series of Schlieren image at at a) $t = 5.04$, b) $t = 7.32$, c) $t = 9.60$, d) $t = 15.30$, e) $t = 22.14$, f) $t = 25.56$.

Some portion of the reflected shock ($R_{1,2}$) travels upstream of the wake and superimposes with the reflected shocks upstream of the particle and eventually form a cumulative reflected shock (RS) upstream of the particle Figure 2-3d. The other portion of the reflected shock ($R_{1,2}$) along with R_2 continues to reverberate downstream of the particle while interacting with the wake. The asymmetry and the waves appearing in the wake in Figure 2-3d suggests the commencement of Kelvin-Helmholtz instability from this interaction. This instability leads to unsteadiness and asymmetric vortex shedding under the effect of continuous wave-wake interactions in Figure 2-3e-f.

The LSZs grow throughout the wake during this interaction and induce stretching effects on the wake behind the particle Figure 2-3 a-d). Figure 2-3e shows the LSZs of the neighboring particles merge together and a shock forms between the wakes of neighboring particles, which indicates the flow is choked due to the convergent-divergent geometry formed by the particles and the wakes behind them. The shock location in the wake dictates the location of vortex roll-up. The formation of the LSZs on the vortices increases the size of eddies and contributes to the formation of large structures (Figure 2-3e-f).

To test the grid dependence of the solution, this problem is tested over three different resolutions based on the effective number of grid points per particle diameter, namely $N_p = 44$, 88, and 176. Figure 2-4 compares the evolution of the unsteady drag coefficient for the three resolutions. Excellent agreement exists for the drag coefficient for $t < 22$ when the flow is dominated by gasdynamic processes with shock waves inducing flow and reflecting off of particles. During this time the wake behind the particle is mostly symmetric but eventually destabilizes and asymmetry is introduced. At $t = 22$ a reflected shock interacts with the wake and completes the onset of unsteady vortex shedding. As expected, some variability exists in the drag

coefficient due to numerical diffusion. However, the results appear to be converging with increasing resolution and the difference between the $N_p = 88$ and 176 cases is small. This suggests that the impact of the grid dependence for the $N_p = 176$ case is minor.

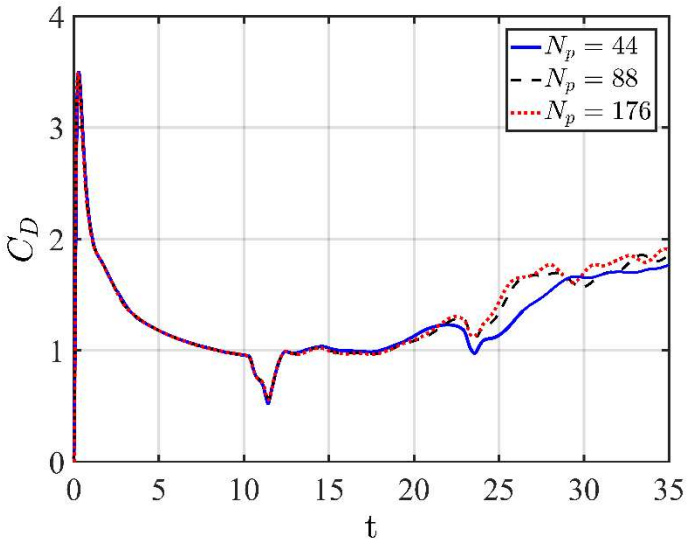

Figure 2-4 Grid convergence for the evolution of unsteady drag coefficient on each particle after the interaction of the shock wave with the particle array.

2.5 Particle cloud behavior

In this section the particle cloud is impacted by both shock and compression waves. The particle cloud configuration is based on the configuration proposed by Regele et. al [27], shown in Figure 2-5.

The particle cloud thickness is used as the reference length and the particle diameter is found based on the desired volume fraction $\alpha_d = 0.15$ where

$$D^2 = \frac{4\alpha L^2}{N\pi} \tag{2-21}$$

and $N = 24$ is the number of particles. The particles are distributed in the x-direction with equal spacing $\delta_x = L/N$ so that each particle occupies a unique x-location, which minimizes the fluctuations in plane-integrated cross-section. Then the particle rows are shuffled from the inline

distributed arrangement. Finally, each consecutive column of particles is shifted in the positive y-direction by approximately one particle diameter. This configuration minimizes the fluctuations in averaged variables and introduces the possibility for the oscillations to tend toward zero as the number of particles becomes large. See Ref. [27] for a more detailed discussion of the configuration.

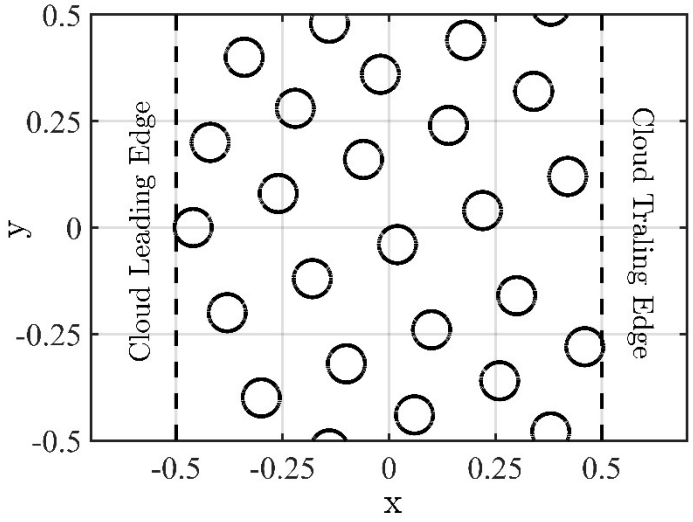

Figure 2-5 Particle arrangement

In this study, we focus on the early interaction of shock and compression waves with the particle cloud, thus based on Ref. [27] and [8] the particles are fixed in place. Ling et al. [8], Mehta et. al. [42] and Sridharan et. al. [43] justify this choice due to the ratio of velocity change in the particle to the fluid scaling with the fluid-to-particle density. Since the fluid-to-particle density ratio is extremely small, the ratio of the changes in velocity is likewise small. For example, in the present case of glass particles in air [21], the density ratio is $O(0.001)$ and thus the timescale associated with significant particle movement is long due to the large inertia of the particle. Therefore, it is reasonable to ignore particle movement in the time scale considered here.

The simulation is performed using the computational setup shown in Figure 2-6. The rectangular computational domain is $(\mathrm{X} \times \mathrm{Y}) = [-6L, 6L] \times [-0.5L, 0.5L]$ where $L = 1$ is the

thickness of the particle cloud, and $L/D = 11.4$. The cloud is located at $-0.5 \leq x \leq 0.5$. The shock and compression waves are initially located at $x = -1.0$. The undisturbed air downstream of the waves is initially at rest, $u_0 = 0$. A detailed discussion of the required grid resolution is contained Section 2.5.2.

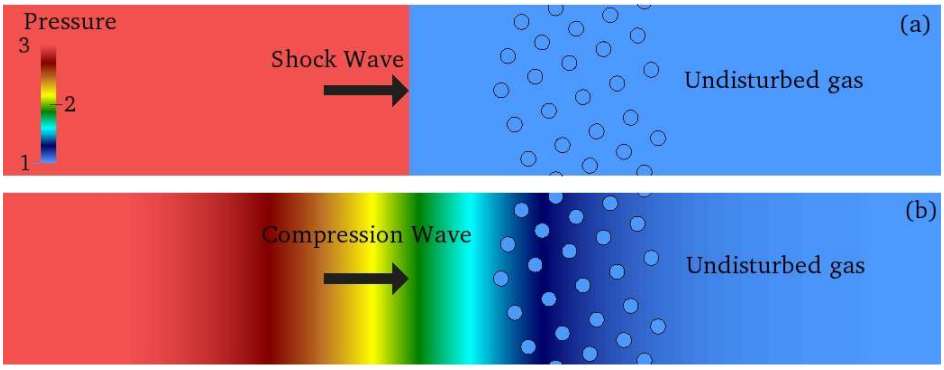

Figure 2-6 Initial pressure profile for a) shock induced case, b) gradually started case.

In the shock wave case, the particle cloud is impacted by a shock wave ($M_s = 1.67$) with the same jump conditions as described in the previous section. In the compression wave case, flow is induced gradually over the particles to study the difference in flow unsteadiness between the two cases. This provides a way to isolate the impulsive effects of shock waves. In this case, the two different states separated by the shock are separated with a smooth transition of states where the transition distance in Eq. (2-17) is equal to the particle cloud thickness $\delta = L$. Figure 2-6 compares the initial pressure profile of the shock and gradually induced cases. Similar to the particle array simulations, periodic boundary conditions are imposed in the transverse direction, the post-shock condition is prescribed at the inlet, and non-reflecting boundary conditions [46] are imposed at the outlet on the right.

2.5.1 The evolution of wave system and local supersonic zones

The evolution of the complex wave system in the particle cloud can be best described using the effect of flow dilatation. The dilatation is the divergence of velocity ($\nabla \cdot \vec{u}$), which is non-zero for compressible flow. This term appears in the non-conservative form of the continuity equation as a source term:

$$\frac{1}{\rho}\frac{D\rho}{Dt} = -\nabla \cdot \vec{u} \tag{2-22}$$

where a non-zero dilatation indicates that the density is changing. Figure 2-7 contains snapshots of dilatation ($\nabla \cdot \vec{u}$) at several different instances after the shock first encounters the particle cloud. In these figures and all the following numerical results, time is non-dimensionalized by the acoustic time of the cloud $\tau = L/c_0$. Negative dilatation (shown in black) represents flow compression while positive values (shown in white) represent flow expansion.

Figure 2-7a shows that when the incident shock first hits the particle cloud, a collective reflected bow shock is created ahead of the cloud, which is comprised of multiple shock reflections, one from the wave system of each particle. A collective transmitted shock is also formed downstream due to the superposition of the incident shock and the Mach stems of all neighboring particles. Expansion fans form on each particle, which introduces non-zero dilatation. Figure 2-7b shows that, as time proceeds, the transmitted shock impinges on the later particles and additional reflected waves from those particles interact with the wave systems of the leading particles and increase the complexity of the wave system. Portions of these waves propagate upstream and increase the amplitude of the cumulative reflected shock. The white areas in the figure indicate positive dilatation, which shows that expansion waves are induced at some point in time near each particle.

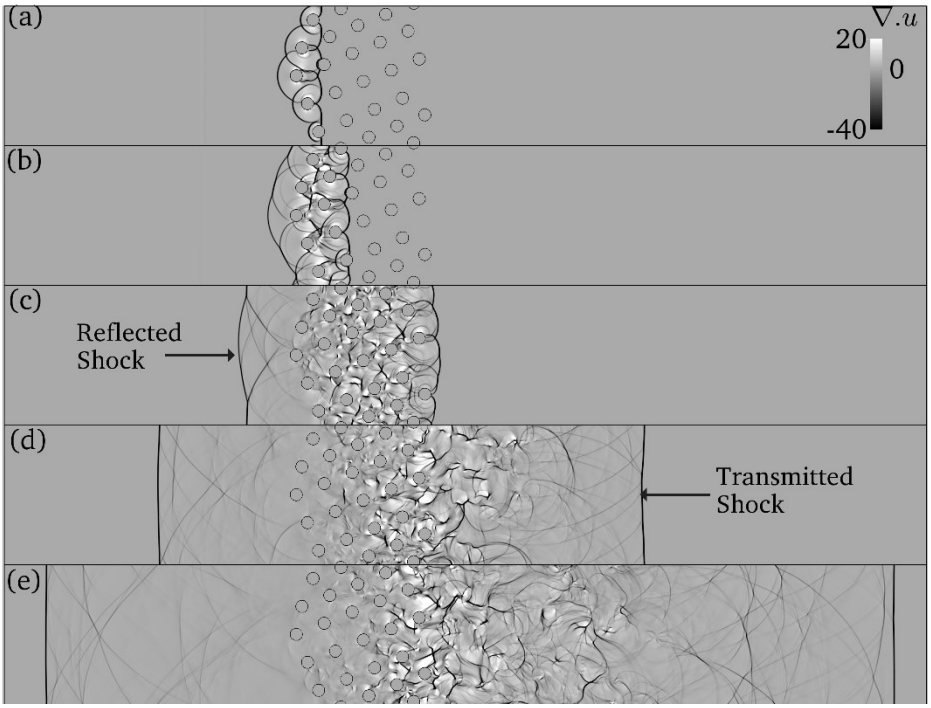

Figure 2-7 Snapshots of the dilatation contours after the interaction of shock with the particle cloud at a) $t = 0.43$, b) 0.56, c) 1.00, d) 2.10, e) 3.2.

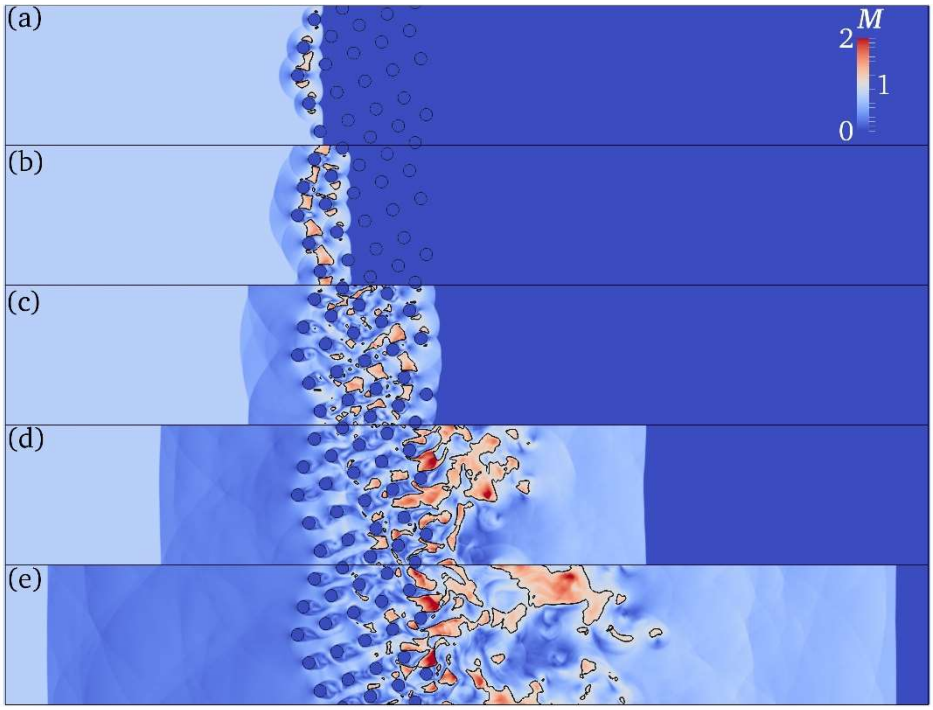

Figure 2-8 The evolution of local supersonic zones (LSZ) in the snapshots of the Mach numbers contours after the interaction of shock with the particle cloud at a) $t = 0.43$, b) 0.56, c) 1.00, d) 2.10, e) 3.2.

As the transmitted shock emerges from the cloud (Figure 2-7c), the reflected shock waves start to dissipate near the leading edge of the cloud. The flow expansion along these particles also reduces (Figure 2-7c-e) and propagates into the cloud as time proceeds. However, the shock waves and expansion waves continue to persist at the trailing positions of the cloud. The persistence of these waves is due to the convergent-divergent flow geometry created by the presence of the particles that creates a choked flow point at the trailing edge of the cloud. Thus, as the gas emerges from the cloud it accelerates to supersonic speed. This creates an $O(1)$ density variation that corresponds to a large dilatation in the cloud and wake region. Figure 2-7d-e indicates the presence of weaker shocks reverberating downstream of the cloud.

Snapshots of the instantaneous flow Mach number contour are depicted in Figure 2-8. As the shock propagates through the cloud the flow accelerates over each particle. Local Supersonic Zones (LSZs) appear over the particles (Figure 2-8a) and grow (Figure 2-8a-b) due to the mutual wave-wave interaction between the neighboring particles and eventually leads to choked flow conditions. Figure 2-8c-f shows that as the transmitted shock leaves the particle cloud, the LSZs travel downstream and accumulate mostly around the choked points at the leading edge of the cloud and the wake behind. This provides evidence of the acceleration of the flow to supersonic speeds while leaving the cloud.

2.5.2 Grid convergence

In Section 2.4 it was found that using $N_p = 176$ cells across a particle diameter was sufficient to minimize the grid sensitivity of the unsteady drag coefficient. In this section the same resolution is used, but it is prudent to analyze the sensitivity of the mean and fluctuating flow fields since these are primary quantities of interest. Thus, in this section a grid sensitivity study is performed

for both the mean streamwise velocity ($\widetilde{u}$) and the fluctuating velocities. The same resolution used in Section 2.4 is used with $N_p = 44, 88, 176$.

The fluctuation in the fluid velocity field (u'') are defined with respect to the Favre averaged fluid velocity ($\tilde{u}$) as $u'' = u - \tilde{u}$. The Root Mean Squared (RMS) of the velocity fluctuations is defined

$$u_{rms} = \sqrt{\widetilde{u''}} = \sqrt{\widetilde{u^2} - \tilde{u}^2} \tag{2-23}$$

Figure 2-9a-c demonstrates the mean streamwise velocity $\tilde{u}$, and RMS velocities in streamwise (u_{rms}) and transverse (v_{rms}) directions as a function of position in streamwise direction, x, for the coarse, fine, and very fine grid resolutions, at non-dimensional time $t = 3.2$. In these figures, the particle cloud is located between $-0.5 < x < 0.5$ and the wake behind the cloud is located between $0.5 < x < 2.5$. For all three resolutions, the mean velocity (Figure 2-9a) demonstrates convergence, however with the fluctuating velocities (Figure 2-9b-c) there are still some variations between the magnitude and phases at some locations. These variations occur near the trailing edge of the cloud because of numerical viscosity on both strong shock waves and the shear layers in the wakes. Overall, the grid using $Np = 176$ case suggests that this level of resolution is sufficient to capture the reflected shock, the transmitted shock, the contact discontinuity as well as the statistics in mean flow field and averaged magnitude of the velocity fluctuations. Thus, this resolution is used to represent the results for the particle cloud test cases.

The comparison of the mean flow field and the RMS velocities is shown in Figure 2-9d at a non-dimensional time $t = 3.2$ to illustrate the relative importance of the fluctuating field to the mean flow field. The stream-wise RMS velocity is larger than the transverse RMS velocity. The RMS velocities are the same order as the mean velocity, both inside the cloud and in the wake behind that. Regele et al. [27] also reported similar findings. However, as expected, the fluctuation

amplitude is smaller in the present work than what have been observed in their Euler simulations. This is expected since in the Euler simulation the molecular viscosity is not present and which may permit non-physical oscillations while using the Navier-Stokes equation coupled with the IBM has removed much more of the noise and non-physical oscillations associated with inviscid flow unsteadiness.

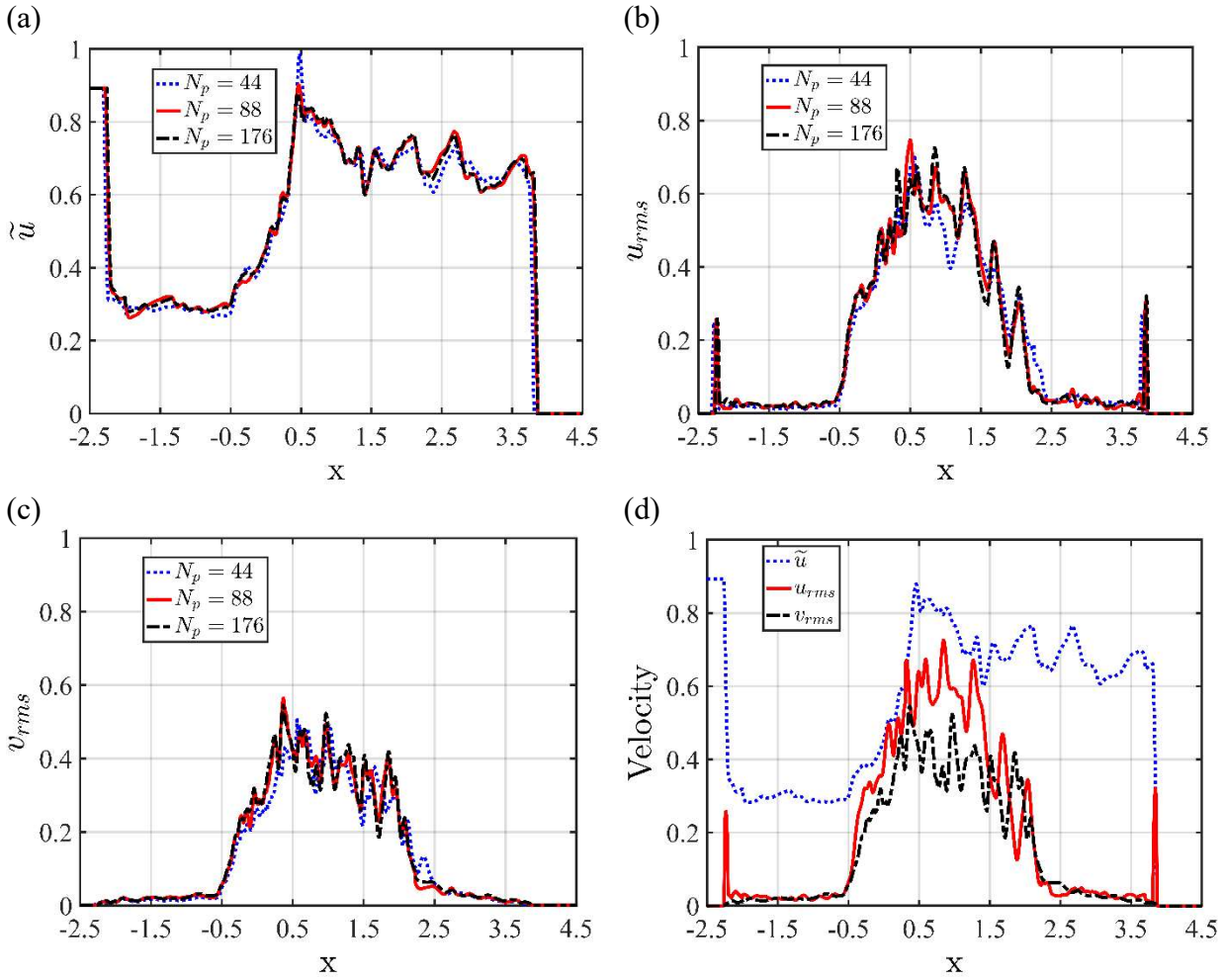

Figure 2-9 Grid convergence study for a) mean streamwise velocity, b) streamwise RMS velocity, c) transverse RMS velocity. d) Comparison of mean stream-wise velocity ($\widetilde{u_1}$) with the stream-wise, u_{rms}, and transverse, v_{rms} , velocity profile at $t = 3.2$.

2.5.3 Analysis of the flow unsteadiness

The evolution of the unsteadiness is presented in Figure 2-10 using contour plots of the vorticity. The instantaneous snapshots in this figure are taken at the same time as Figure 2-7 and Figure 2-8. Therefore, the reader is referred to those figures for the corresponding wave-system and LSZ locations.

Figure 2-10a-b shows that as a shock penetrates through the cloud, a boundary layer forms around each particle. The boundary layers eventually separate under the effect of the local wave-systems. The separated boundary layer (wake) behind each particle becomes unstable and vortex shedding starts. The magnitude of vorticity inside the cloud increases between $t = 1$ and 2.1 (Figure 2-10c-d) as the number of the shocks and LSZs in the cloud increase, which indicates an increase in unsteadiness during this period. Between $t = 2.1$ and 3.2 when shock transmits downstream, the magnitude of the vorticity decreases for the upstream particles whose positions are $x < 0$ (Figure 2-10d-e), where the shocks have been dissipated and LSZs have moved downstream. However, large unsteadiness is seen around the trailing edge of the cloud due to the presence of shocks and choked flow conditions that persist in those areas and continuously interact with the vortical structures. The vortical structures are elongated under the effects of LSZs. This effect is limited in the particle cloud due to the blocking effect of the neighboring particles. However, the stretching effect is greatest on particles located at the trailing edge of the cloud where the flow is accelerating in larger LSZs and experiences larger expansion and dilatation, while leaving the cloud, which induces more stretching effect on the shear layers.

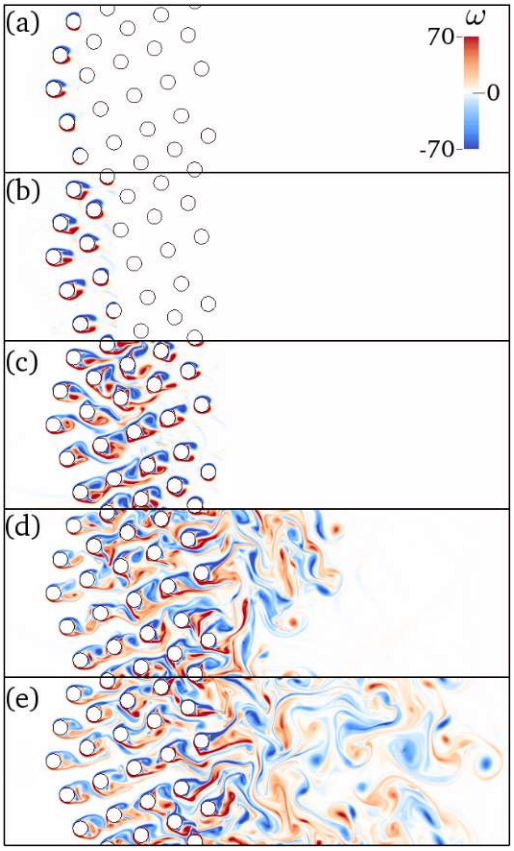

Figure 2-10 Snapshots of the vorticity after the interaction of shock with the particle cloud at a) $t = 0.43$, b) 0.56, c) 1.00, d) 2.10, e) 3.2.

For deeper insight into the sources of unsteadiness in the shock-particle cloud interaction a budget analysis of the vorticity equation production terms is conducted. The evolution equation for vorticity in a compressible flow

$$\frac{D\vec{\omega}}{Dt} = (\vec{\omega}\cdot\nabla)\vec{u} - \vec{\omega}(\nabla\cdot\vec{u}) + \frac{\nabla\rho\times\nabla p}{\rho^2} + \frac{1}{Re_a}\nabla\times\left(\frac{\nabla\cdot\tau}{\rho}\right) \tag{2-24}$$

describes the production and evolution of the fluid vorticity. In this equation, the left-hand side is the material derivative of the vorticity vector that describes the rate of change for vorticity of the gas phase. This change can be attributed to unsteadiness in the gas phase and the advection of vorticies. The first term on the right-hand side represents the stretching or tilting of vorticity due to velocity gradients. This term is zero for the 2D analysis. The second term on the right-hand side is the vorticity-dilatation that describes stretching of vorticity due to flow compressibility.

The third term on the right-hand side is the baroclinic term, which accounts for the production of vorticity due to misalignment of density and pressure gradient. The last term accounts for the diffusion of vorticity due to viscous diffusion. This term can be rewritten as

$$\nabla \times \left(\frac{\nabla \cdot \tau}{\rho}\right) = \nabla \times \left(\frac{\nabla \cdot (\mu \nabla \vec{u})}{\rho}\right) = \nu \nabla \times \left(\nabla . (\nabla \vec{u})\right) = \nu \nabla \times \nabla^2 \vec{u} = \nu \nabla^2 \omega \qquad (2\text{-}25)$$

assuming that the viscosity (μ) is constant and ν is the kinematic viscosity. This form describes the effect of viscous diffusion on the vorticity distribution. Analogues to the diffusion terms in the Navier-Stokes equations suggest that this term is always diffusive because the kinematic viscosity is always positive.

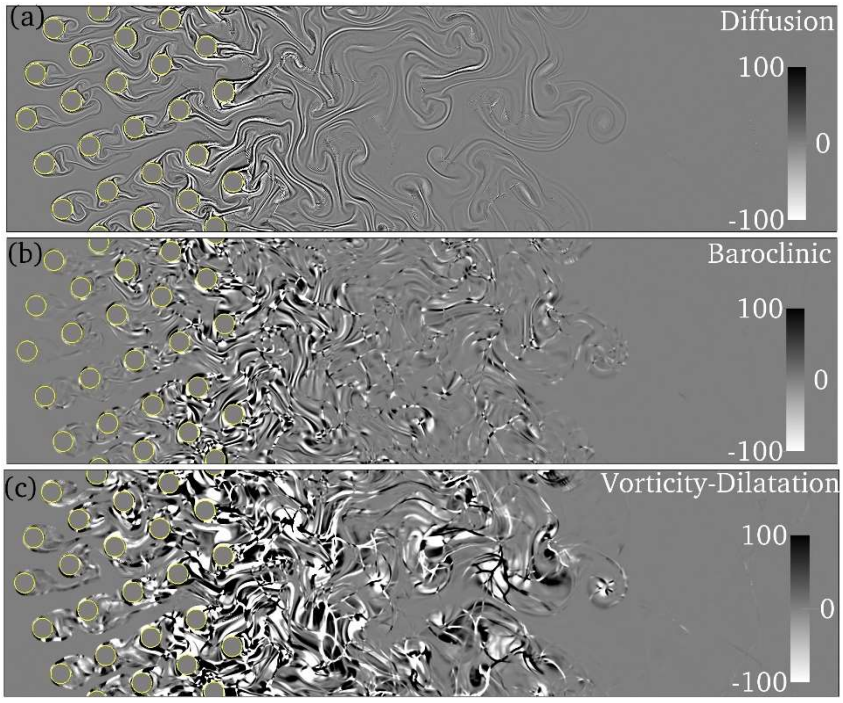

Figure 2-11 Vorticity production terms at $t = 3.2$ for a) diffusion term, b) baroclinic term, c) vorticity-dilatation term.

Figure 2-11 shows the dilatation, baroclinic, and diffusion source terms of the vorticity equation at a non-dimensional time of $t = 3.2$ for the shock-particle cloud interaction case. Figure 2-11a shows the diffusion term that is present around the particles due to the shear induced by

particles, and in the shear layers of vortical structures both inside the cloud and in the wake behind. Due to the no-slip boundary condition at the particle surface, the viscous flow decelerates in a thin boundary layer along the surface, which produces vorticity. Subsequently, this vorticity is advected downstream with the fluid. Away from particle surfaces, this term diffuses vorticity.

It can be seen that the diffusion term is larger around the trailing edge particles than the leading edge particles. This can be explained by comparing this plot with the Mach number contour plot at the corresponding time (Figure 2-8e). Mach number contours indicate that the flow is slower in most locations near the leading edge while the flow is significantly faster near the trailing edge. As a result, stronger shear stress is present in the flow around particles closer to the trailing edge.

Figure 2-11b illustrates the baroclinic term. This term results in generation of vorticity from unequal acceleration as a result of misalignment between the pressure and density gradients. In this condition, the pressure force on a fluid element does not pass through its center of mass and the pressure exerts a torque on the fluid element to generate vorticity or intensify pre-existing vorticity. Comparison of Figure 2-11b with the vorticity profile (Figure 2-10e) and wave structure (Figure 2-7e) indicate that this effect is present where shocks collocate with vortical structures and is more dominant wherever shocks are stronger. The wave structure in Figure 2-7e shows that at $t = 3.2$ stronger shocks are located at the second half of the cloud and the near wake region behind the cloud. As a result, the baroclinic term is more significant in those locations.

Figure 2-11c. shows the vorticity-dilatation term at $t = 3.2$. Comparison of this figure with the dilatation contours at the corresponding time (Figure 2-7e) indicate that the vorticity-dilatation term acts as a source for amplifying pre-existing vorticity in the region of negative dilatation (compression) and as a sink to attenuate vorticity in the region of positive dilatation (expansion).

The absolute value of this term is observed to be large in the supersonic regions (see Figure 2-8e), near the trailing edge of the cloud and in the wake region.

The qualitative discussion of the vorticity source terms above helps identify the effect of each term on the evolution of vorticity and unsteadiness and tie the effect with the local flow features, such as wave structure, LSZs and local dilatation. To better quantify these three terms and demonstrate the relative importance of them in the strong flow unsteadiness, we present a quantitative discussion based on the comparison of their phase-averaged magnitude. Similar quantification is performed for a gradually induced case.

The averaging method used to quantify the flow unsteadiness is described in Section 2.3.1. Since the resultant curves are still oscillatory due to the strong flow unsteadiness, a spline curve with the smoothing factor of $sp = 0.998$ is fitted to the data set to create a smooth graph.

Figure 2-12 shows the magnitude of the averaged diffusion, baroclinic and vorticity-dilatation terms at four times, $t = 0.56, 1, 2.1, 3.2$, for both the shock-induced and gradually-induced cases. To focus on regions with flow unsteadiness the results are plotted from $x = -0.5$ to $x = 2.5$. For both cases, the vorticity-dilatation term is the most dominant term at all considered times. The baroclinic and diffusion terms are both almost an order of magnitude less than the vorticity-dilatation term. The magnitude of each term for the shock-induced case is much greater than the gradually induced case. The order of the difference between the two cases for each term at the early time of interaction is larger than at later times. This indicates that the impulsive nature of the shock produces additional unsteadiness in the flow.

Figure 2-12a shows that for early times in the gradually induced case, the diffusion term and the baroclinic term are of the same order and competing together. In this case, the baroclinic effect is larger in the first half of the cloud while the diffusion term is larger in the second half. This

occurs because the induced flow transitions from low speed to high speed conditions further into the particle cloud. The strength of the reflected shock is proportional to the free stream velocity. Thus, the reflected shocks in the first half that have experienced higher free stream velocities than the second half of the cloud are stronger, which leads to a stronger baroclinic effect on those particles. In the shock-induced case, since the reflected shock waves reverberate around inside the cloud, the baroclinic term is almost an order larger than the diffusion term.

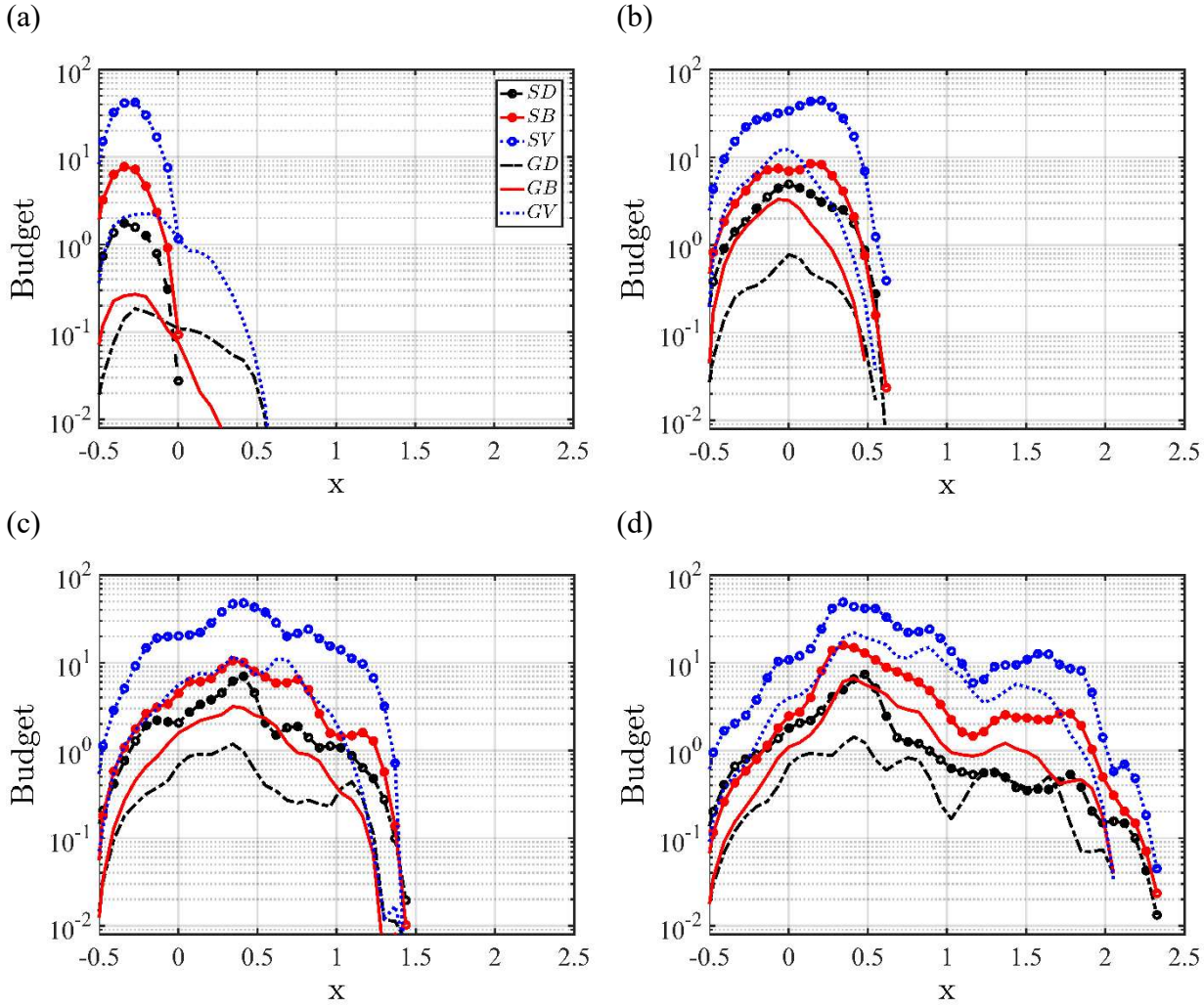

Figure 2-12 The magnitude of the averaged diffusion (black), baroclinic (red) and vorticity-dilatation (blue) terms at four times, $t = 0.56, 1, 2.1, 3.2$ for both cases of the shock-induced flow over the cloud (··o) and the gradually-induced flow over the cloud($-\cdot$). Cloud is located at $-0.5 < x < 0.5$ and wake is at $x > 0.5$.

As flow accelerates in the cloud (Figure 2-12b) the shear on the particles increases and thus the vorticity production from the diffusion term increases as well. The Baroclinic term grows due to the formation of reflected shocks and shocklets all over the cloud. The vorticity-dilatation term grows because the flow remains transonic within the cloud (Figure 2-7c).

After the transmitted shock leaves the cloud (Figure 2-12b), the shock waves dissipate which causes the baroclinic term to reduce. Figure 2-12c indicates that the decay starts from the leading edge and penetrates the cloud with time. Dilatation also diminishes in the cloud (Figure 2-7d-e) due to this transition and causes the vorticity-dilatation term to reduce as well (Figure 2-12c-d). However due to the choked flow conditions, local supersonic zones and finite dilatation around the trailing edge, all source terms maintain a peak value for $0.3 < x < 0.5$ at late times (Figure 2-12d).

In the wake, all vorticity production sources become smaller. In this region the dilatation and baroclinic terms are still free to produce more vorticity from shock waves and localized supersonic zones. However, in the absence of particles the diffusion term dissipates the existing vorticity. Once the flow is choked and passes through standing shocks to equalized the pressure the flow will remain subsonic. This ensures that the baroclinic term decreases further into the wake region (Figure 2-7d). Finally, once the flow is subsonic the vorticity amplifying effect of the dilation term will also disappear, which results in reduction of vorticity-dilatation term (Figure 2-7e).

2.5.4 Kinetic energy in the fluctuating motion

The importance of the fluctuating field and the effect of fluctuating velocity on the flow behavior can be best described using the Reynolds stress term in the mean flow momentum equation. The trace of the Reynolds stress term is kinetic energy in the fluctuating field, which is defined as

$$\mathrm{K} = \frac{1}{2}\frac{\langle \rho u_i'' u_i'' \rangle}{\langle \rho \rangle} = \frac{\widetilde{u''_\iota u''_\iota}}{2}. \tag{2-26}$$

The average kinetic energy, $\mathrm{E_k}$, in the gas phase

$$\mathrm{E_k} = \frac{1}{2}\frac{\langle \rho u_i u_i \rangle}{\langle \rho \rangle} = \frac{\widetilde{u_\iota u_\iota}}{2} \tag{2-27}$$

is the sum of the kinetic energy in the mean fluid field, $\widetilde{\mathrm{E_k}}$,

$$\widetilde{\mathrm{E_k}} = \frac{\tilde{u}_\mathrm{J}\tilde{u}_\mathrm{J}}{2} \tag{2-28}$$

and the average kinetic energy in the fluctuating field, K. It should be noted that the objective of the present work is to provide a better understanding of how flow unsteadiness is created in these situations and not to quantitatively predict the flow unsteadiness. The particle configuration developed by Regele et al. (2014) provides a way to minimize fluctuations in the volume fraction when calculating averaged quantities. Quantitative prediction must be performed with spherical particles in three dimensions using multiple particle arrangements.

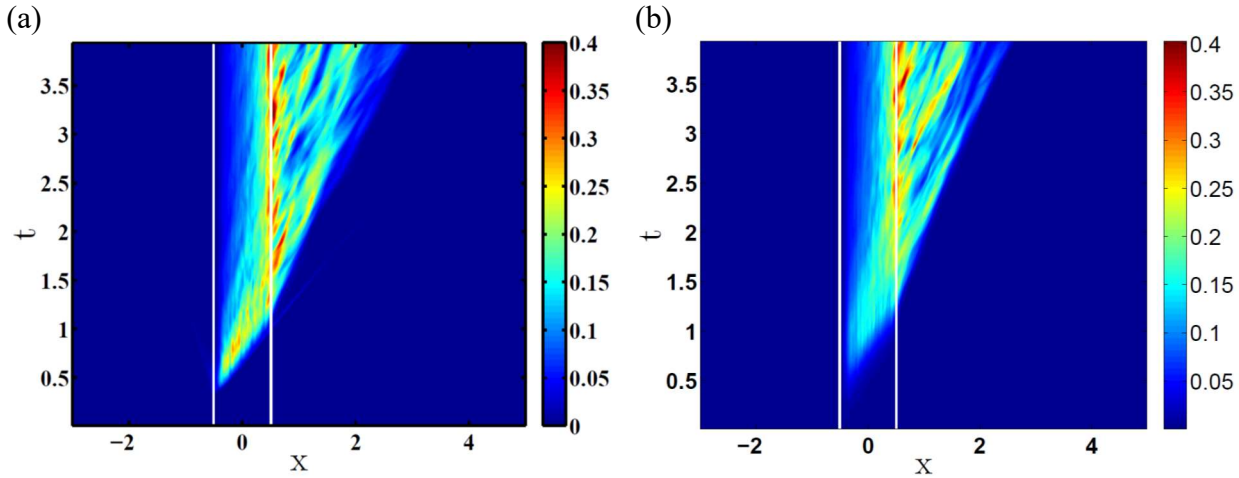

Figure 2-13 x-t diagram of the kinetic energy in the fluctuating field for a) shock-induced and b) gradually-induced flow by a compression wave.

Figure 2-13 shows the x-t diagram of the non-dimensional kinetic energy in the fluctuating field, K, for both the shock-induced case and the gradually-induced case. From the figure it is

evident that the average kinetic energy in the fluctuating field, K is present, in both the cloud ($-0.5 < x < 0.5$) and the wake behind the cloud (between $x = 0.5$ and the contact line) for both cases. In both cases the magnitude of K is significant during the early phases of interaction. Comparison of the shock-induced case, Figure 2-13a, with the gradually-induced case, Figure 2-13b, shows that before about $t = 2.1$, when the flow is in the unsteady mode, the shock-induced case presents a higher magnitude of the kinetic energy in the fluctuating motion both inside the cloud and on the trailing edge of the cloud and it experiences a more rapid change in comparison to the gradually-induced case. This provides evidence that the impulsive effect of the shock, introduces stronger unsteady effect. In both cases, after $t = 2.2$ the flow transitions to the steady-state, showing a decay in K due to the dissipation of shocks and compression waves and reduction of wave-wake interactions. However, it is seen that K holds a significant value at locations around the trailing edge of the cloud (x~0.5) and the immediate wake behind it.

To better illustrate the significance of the strong unsteady effect induced by the impulsive effect of the shock, the evolution of the kinetic energy over time in three specific locations of the particle cloud (where x is -0.3, 0.0 and 0.3) are compared with that of the gradually-induced case in Figure 2-14. At each location, the evolution of the kinetic energy in the fluctuating field, K, reaches a peak followed by a decay over time and oscillates around its steady state value for both cases. The peak value for the shock-induced case is larger at all locations. The difference between the peak values indicate the impulsive effect of shock on appearance of the fluctuating field at those locations. This effect is more dominant in the particles closer to the leading edge, $x = -0.3$ and it decreases as we reach $x = 0.3$. At each location the peak occurs at a later time for the gradually induced case due to the delay of impact over the large transition distance, δ, for the compression wave.

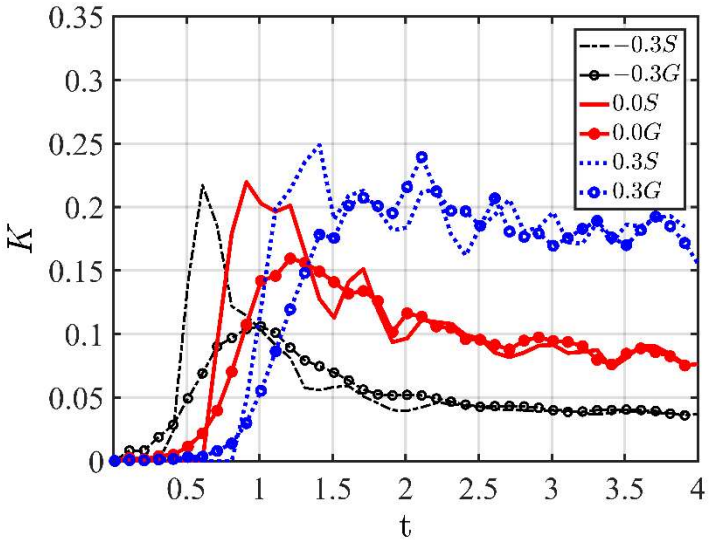

Figure 2-14 Comparison of kinetic energy in the fluctuating motion at three different positions, $x = -0.3, 0.0, 0.3$, of the particle cloud for the shock induced (S) and gradually induced cases (G).

The steady-state values for the gradually-induced case converges to that of the shock induced case at each location because the cumulative effect of the shock and the compression wave should converge together. The reason being that both waves induce flow transition from the same pre-shock to the same post-shock condition. The magnitude of steady-state value of K is larger near the trailing edge of the cloud due to the choking effect in local supersonic zones and persistence of moving shocks at both case which lead to continues wave-wake interaction between these shock waves and the expanded vortical structure that introduces continuous instability and enhances the velocity fluctuations [52].

Comparison of the non-dimensional kinetic energy in the fluctuating field, K, with the kinetic energy in the mean flow field, $\widetilde{E_k}$, reveals the importance of the fluctuating field generated under the effect of the shock on the particle cloud. This comparison is demonstrated in Figure 2-15 at four different non-dimensional times, $t = 0.56$, $t = 1$, $t = 2.1$ and $t = 3.2$. At $t = 0.56$ (Figure 2-15a). When the transmitted shock is inside the cloud, the kinetic energy in the fluctuating field, K, is developing and reaching the kinetic energy in the mean flow field $\widetilde{E_k}$.

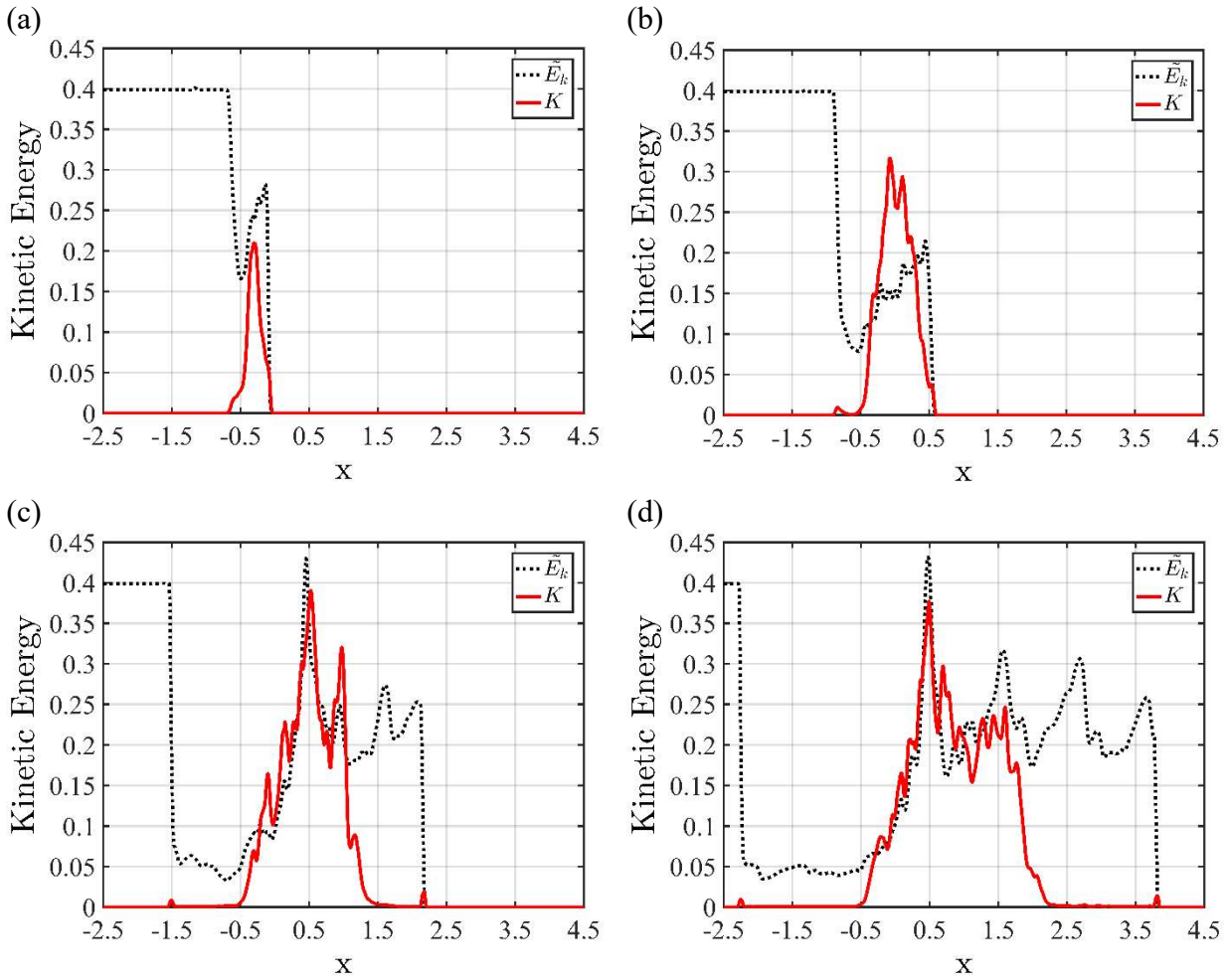

Figure 2-15 Comparison of the mean kinetic energy with the kinetic energy in the fluctuating field

Figure 2-15b shows that, as the transmitted shock is emerging the cloud, $t = 1$, K has increased all over the cloud while $\widetilde{E_k}$ has decreased. This means that the energy has been transferred from the mean flow field to the fluctuating field. This leads to K having a larger value than $\widetilde{E_k}$ in almost 60% of the cloud. This is the consequence of production of multiple reflected shocks that continuously interact with the highly unsteady wakes and enhance the kinetic energy in the fluctuating motion.

As the transmitted shock is traveling downstream (Figure 2-15c-d) both K and $\widetilde{E_k}$ decline in the leading locations of the cloud because the flow regime has changed to subsonic in these regions

and the shock waves have dissipated. However, towards the trailing edge they still hold larger values because of the persistence of the shock waves and LSZs in those areas. The ratio of $K/\widetilde{E_k}$ is approximately one both inside the cloud and the near wake behind that.

These results show that the unsteady effect of the shock induces a significant amount of kinetic energy in the fluctuating motion. Comparison of magnitude of kinetic energy in the fluctuating motion and the kinetic energy in the mean flow field proves that K contribute significantly to the average kinetic energy, E_k. Since K is the trace of the Reynolds stress term it implies that this term in the momentum equation and the corresponding unclosed terms in the energy equation cannot be neglected while attempting to model shock-particle cloud interaction in the dense regime.

2.6 Conclusions

In this work the interaction of a shock wave with two different configurations of particles in the dense gas-solid regime, namely a transverse array of particles and a particle cloud is investigated. Particle-resolved direct numerical simulations are performed by solving the compressible Navier-Stokes equations coupled with an immersed boundary method.

Simulations of a shock interaction with a transverse array of particles reveal the evolution of the wave system, local supersonic zones, and the wake behind each particle as well as the commencement of Kelvin-Helmholtz instabilities and vortex shedding under the effect of the wave-wave and wave-wake interactions between the neighboring particles. It is demonstrated that the unsteady drag coefficient of a cylinder after shock passage agrees well with experimental data. It is also shown that the drag coefficient, mean and unsteady flow velocities are insensitive to grid resolution.

Shock interaction with a particle cloud in comparison with a gradually-induced flow over the same particle cloud is investigated to quantify the flow unsteadiness and velocity fluctuations that arise from these interactions. The sources of flow unsteadiness and vorticity generation are quantified by analyzing the vorticity production terms for compressible flows. It is shown that a primary source of vorticity comes from the viscous diffusion term when the no slip condition at particle surfaces creates strong shear forces. This vorticity is then advected downstream. The baroclinic term, which is larger than the diffusion term in most locations, generates vorticity where reflected shocks collocate with the vortical structures. The vorticity-dilatation term is almost an order of magnitude larger than the other two terms. It amplifies pre-existing vorticity in the region of negative dilatation and attenuates vorticity in the region of positive dilatation. The magnitude of each term for the shock-induced case is much larger than the gradually induced case because of a shock waves natural ability to induce flow unsteadiness. The order of this difference reduces over time until the shock and gradually induced cases reach the same unsteadiness levels.

To perform a detailed analysis of the importance of velocity fluctuations and kinetic energy in the fluctuating field, arising from the strong unsteadiness, phasic-Favre averaging statistics are calculated. Based on this analysis, the kinetic energy in the fluctuating field is the same order of magnitude as the kinetic energy in the mean flow field and contributes significantly to the mean kinetic energy. Thus, the Reynolds stress term in the momentum equation and the corresponding unclosed terms in the energy equation cannot be neglected while modeling the dense compressible flow regime. While this effect is true in general it is greater in shock-induced situations.

References

[1] L. J. Forney, D. B. Van Dyke, and W. K. McGregor, “Dynamics of Particle—Shock Interactions: Part I: Similitude,” *Aerosol Sci. Technol.*, vol. 6, no. 2, pp. 129–141, Jan. 1987.

[2] L. J. Forney, A. E. Walker, and W. K. McGregor, "Dynamics of Particle-Shock Interactions: Part II: Effect of the Basset Term," *Aerosol Sci. Technol.*, vol. 6, no. 2, pp. 143–152, Jan. 1987.

[3] G. Tedeschi, H. Gouin, and M. Elena, "Motion of tracer particles in supersonic flows," *Exp. Fluids*, vol. 26, no. 4, pp. 288–296, Mar. 1999.

[4] M. Parmar, A. Haselbacher, and S. Balachandar, "Improved Drag Correlation for Spheres and Application to Shock-Tube Experiments," *AIAA Journal*, vol. 48, no. 6. pp. 1273–1276, Jun-2010.

[5] Y. Ling, A. Haselbacher, and S. Balachandar, "Importance of unsteady contributions to force and heating for particles in compressible flows: Part 1: Modeling and analysis for shock–particle interaction," *Int. J. Multiph. Flow*, vol. 37, no. 9, pp. 1026–1044, 2011.

[6] H. Tanno, K. Itoh, T. Saito, A. Abe, and K. Takayama, "Interaction of a shock with a sphere suspended in a vertical shock tube," *Shock Waves*, vol. 13, no. 3, pp. 191–200, Nov. 2003.

[7] A. E. Bryson and R. W. F. Gross, "A new approach to problems of shock dynamics Part 2. Three-dimensional problems," *J. Fluid Mech.*, vol. 5, no. 3, p. 369, Apr. 1959.

[8] Y. Ling, J. L. Wagner, S. J. Beresh, S. P. Kearney, and S. Balachandar, "Interaction of a planar shock wave with a dense particle curtain: Modeling and experiments," *Phys. Fluids*, vol. 24, no. 11, 2012.

[9] M. Sun, T. Saito, K. Takayama, and H. Tanno, "Unsteady drag on a sphere by shock wave loading," *Shock Waves*, vol. 14, no. 1–2, pp. 3–9, Jun. 2005.

[10] M. Parmar, A. Haselbacher, and S. Balachandar, "Modeling of the unsteady force for shock–particle interaction," *Shock Waves*, vol. 19, no. 4, pp. 317–329, Aug. 2009.

[11] R. R. Nourgaliev and T. G. Theofanous, "High-fidelity interface tracking in compressible flows: Unlimited anchored adaptive level set," *J. Comput. Phys.*, vol. 224, no. 2, pp. 836–866, 2007.

[12] T. G. Theofanous and C. H. Chang, "The dynamics of dense particle clouds subjected to shock waves. Part 2. Modeling/numerical issues and the way forward," *Int. J. Multiph. Flow*, vol. 89, pp. 177–206, 2017.

[13] F. Zhang, D. L. Frost, P. A. Thibault, and S. B. Murray, "Explosive dispersal of solid particles," *Shock Waves*, vol. 10, no. 6, pp. 431–443, Jan. 2001.

[14] G. Rudinger, *Fundamentals of gas-particle flow*. Elsevier Scientific Pub. Co, 1980.

[15] M. Sommerfeld, "The unsteadiness of shock waves propagating through gas-particle mixtures," *Exp. Fluids*, vol. 3, no. 4, pp. 197–206.

[16] J. H. Geng and H. Groenig, “Dust suspensions accelerated by shock waves,” *Exp. Fluids*, vol. 28, no. 4, pp. 360–367, Apr. 2000.

[17] H. Miura and I. I. Glass, “On the Passage of a Shock Wave Through a Dusty-Gas Layer,” *Proc. R. Soc. London A Math. Phys. Eng. Sci.*, vol. 385, no. 1788, 1983.

[18] B. Y. Wang, Q. S. Wu, C. Wang, O. Igra, and J. Falcovitz, “Shock wave diffraction by a square cavity filled with dusty gas,” *Shock Waves*, vol. 11, no. 1, pp. 7–14, Mar. 2001.

[19] M. S. Baer and J. W. Nunziato, “A two-phase mixture theory for the deflagration to detonation (DDT) transition in reactive granular materials,” *Int. J. Multiph. Flow*, vol. 12, no. 6, pp. 861–889, 1986.

[20] J. L. Wagner, S. P. Kearney, S. J. Beresh, E. P. DeMauro, and B. O. Pruett, “Flash X-ray measurements on the shock-induced dispersal of a dense particle curtain,” *Exp. Fluids*, vol. 56, no. 12, pp. 1–12, 2015.

[21] J. L. Wagner *et al.*, “A multiphase shock tube for shock wave interactions with dense particle fields,” *Exp. Fluids*, vol. 52, no. 6, pp. 1507–1517, 2012.

[22] M. Parmar, a Haselbacher, and S. Balachandar, “On the unsteady inviscid force on cylinders and spheres in subcritical compressible flow.,” *Philos. Trans. A. Math. Phys. Eng. Sci.*, vol. 366, no. 1873, pp. 2161–2175, 2008.

[23] A. L. Gonor, J. J. Gottlieb, and I. Hooton, “Shock wave diffraction over wedges, cylinders, and spheres in gases, liquids, and condensed matter,” *J. Appl. Phys.*, vol. 95, no. 3, pp. 1577–1585, 2004.

[24] M. Bredin and B. Skews, “Drag measurements in unsteady compressible flow. Part 1: an unsteady flow facility and stress wave balance. R&D J,” *South Afr. Inst. Mech. Eng*, 2007.

[25] F. M. Najjar, J. P. Ferry, A. Haselbacher, and S. Balachandar, “Simulations of Solid-Propellant Rockets: Effects of Aluminum Droplet Size Distribution,” *J. Spacecr. Rockets*, vol. 43, no. 6.

[26] V. S. Lanovets, V. A. Levich, N. K. Rogov, Y. V. Tunik, and K. N. Shamshev, “Dispersion of the detonation products of a condensed explosive with solid inclusions,” *Combust. Explos. Shock Waves*, vol. 29, no. 5, pp. 638–641, Sep. 1993.

[27] J. D. Regele, J. Rabinovitch, T. Colonius, and G. Blanquart, “Unsteady effects in dense, high speed, particle laden flows,” *Int. J. Multiph. Flow*, vol. 61, no. May, pp. 1–13, 2014.

[28] M. Mehrabadi, S. Tenneti, R. Garg, and S. Subramaniam, “Pseudo-turbulent gas-phase velocity fluctuations in homogeneous gas – solid flow : fixed particle assemblies and freely evolving suspensions,” *J. Fluid Mech*, vol. 770, pp. 210–246, 2015.

[29] B. Sun, S. Tenneti, S. Subramaniam, and D. L. Koch, "Pseudo-turbulent heat flux and average gas–phase conduction during gas–solid heat transfer: flow past random fixed particle assemblies," *J. Fluid Mech.*, vol. 798, pp. 299–349, 2016.

[30] W. Sutherland, "The viscosity of gases and molecular force," *Philos. Mag. Ser. 5*, vol. 36, no. 223, pp. 507–531, 1893.

[31] B. Sun, S. Tenneti, and S. Subramaniam, "Pseudo-turbulent heat flux and average gas – phase conduction in gas – solid heat transfer : Flow past random fixed particle assemblies," 2015.

[32] A. Chaudhuri, A. Hadjadj, and A. Chinnayya, "On the use of immersed boundary methods for shock/obstacle interactions," *J. Comput. Phys.*, vol. 230, no. 5, pp. 1731–1748, 2011.

[33] N. K. R. Kevlahan and O. V. Vasilyev, "An Adaptive Wavelet Collocation Method for Fluid-Structure Interaction at High Reynolds Numbers," *SIAM J. Sci. Comput.*, vol. 26, no. 6, pp. 1894–1915, Jan. 2005.

[34] A. Piquet, O. Roussel, and A. Hadjadj, "A comparative study of Brinkman penalization and direct-forcing immersed boundary methods for compressible viscous flows," *Comput. Fluids*, vol. 136, pp. 272–284, 2016.

[35] E. Brown-Dymkoski, N. Kasimov, and O. V. Vasilyev, "A characteristic based volume penalization method for general evolution problems applied to compressible viscous flows," *J. Comput. Phys.*, vol. 262, pp. 344–357, 2014.

[36] W. Sweldens, "The Lifting Scheme: A Custom-Design Construction of Biorthogonal Wavelets," *Appl. Comput. Harmon. Anal.*, vol. 3, no. 2, pp. 186–200, Apr. 1996.

[37] O. V Vasilyev and C. Bowman, "Second-Generation Wavelet Collocation Method for the Solution of Partial Differential Equations," *J. Comput. Phys.*, vol. 165, no. 2, pp. 660–693, Dec. 2000.

[38] O. V. Vasilyev, "Solving Multi-dimensional Evolution Problems with Localized Structures using Second Generation Wavelets," *Int. J. Comut. Fluid Dyn.*, vol. 17, no. 2, pp. 151–168, Mar. 2003.

[39] O. V Vasilyev and N. K-R Kevlahan, "An adaptive multilevel wavelet collocation method for elliptic problems," 2005.

[40] J. D. Regele and O. V. Vasilyev, "An adaptive wavelet-collocation method for shock computations," *Int. J. Comut. Fluid Dyn.*, vol. 23, no. 7, pp. 503–518, 2009.

[41] A. Abe, K. Kayama, and K. Itoh, "Experimental and numerical study of shock wave propagation over cylinders and spheres," *Trans. Model. Simul. www.witpress.com*, vol. 30, pp. 1743–355, 2001.

[42] Y. Mehta, T. L. Jackson, J. Zhang, and S. Balachandar, "Numerical investigation of shock interaction with one-dimensional transverse array of particles in air," *J. Appl. Phys.*, vol. 119, no. 10, pp. 0–13, 2016.

[43] P. Sridharan, T. L. Jackson, J. Zhang, and S. Balachandar, "Shock interaction with one-dimensional array of particles in air," *J. Appl. Phys.*, vol. 117, no. 7, p. 75902, Feb. 2015.

[44] R. J. Goetsch, "A numerical approach to the simulation of granular and multiphase flows," *Grad. Theses Diss.*, 2015.

[45] C. Y. Xu, L. W. Chen, and X. Y. Lu, "Large-eddy simulation of the compressible flow past a wavy cylinder," *J. Fluid Mech.*, vol. 665, pp. 238–273, 2010.

[46] J. B. Freund, "Proposed Inflow/Outflow Boundary Condition for Direct Computation of Aerodynamic Sound," *AIAA J.*, vol. 35, no. 4, pp. 740–742, Apr. 1997.

[47] J. Y. Yang, Y. Liu, and H. Lornax, "Computation of Shock Wave Reflection by Circular Cylinders," *AIAA J.*, vol. 25, no. 5, pp. 683–689, 1987.

[48] J. Kaca, "An interferometric investigation of the diffraction of a planar shock wave over a semicircular cylinder," *UTIAS Tech. Note*, vol. 269, no. September, 1988.

[49] D. K. Ofengeim and D. Drikakis, "Simulation of blast wave propagation over a cylinder," *Shock Waves*, vol. 7, no. 5, pp. 305–317, 1997.

[50] D. Drikakis, D. Ofengeim, E. Timofeev, and P. Voionovich, "Computation of Non-Stationary Shock-Wave/Cylinder Interaction Using Adaptive-Grid Methods," *J. Fluids Struct.*, vol. 11, no. 6, pp. 665–692, 1997.

[51] J. Zoltak and D. Drikakis, "Hybrid upwind methods for the simulation of unsteady shock-wave diffraction over a cylinder," *Comput. Method. Appl. M*, vol. 162, no. 97, pp. 165–185, 1998.

[52] L.-W. Chen, C.-Y. Xu, and X.-Y. Lu, "Numerical investigation of the compressible flow past an aerofoil," *J. Fluid Mech.*, vol. 643, p. 97, 2009.

CHAPTER 3. NUMERICAL SIMULATION OF SHOCK WAVE IMPACTING A DROPLET USING THE ADAPTIVE WAVELET COLLOCATION METHOD

A paper Published in proceedings of ILASS Americas 28th Annual
Conference on Liquid Atomization and Spray Systems, Dearborn, MI, May 2016

Zahra Hosseinzadeh Nik[4], Mohamad Aslani[5], Mark Owkes[6] Jonathan D. Regele[7].

Abstract

Under startup conditions, supersonic combustors must atomize and ignite liquid fuel at hypersonic speeds. Little is known about fluid atomization in a supersonic cross flow experimentally and few methods exist to investigate this behavior numerically. In order to simulate this behavior, an approach must be used that naturally accounts for the multiscale nature of the atomization process. In this work, a five equation interface-capturing scheme is developed to solve the compressible multi-component Navier-Stokes equations. The gas phase is modeled as an ideal gas and the liquid phase is modeled using a stiffened-gas equation of state. In order to account for the truly multiscale nature of this fluid behavior, the governing equations are solved using the highly efficient Parallel Adaptive Wavelet-Collocation Method (PAWCM). The PAWCM uses wavelets to dynamically adapt the grid used to represent the solution, which minimizes the overall computational cost and allows larger simulations to be performed. Shocks and interfaces are captured using a modified version of the hyperbolic solver developed specifically for the PAWCM.

[4] PhD candidate, Aerospace and Mechanical Engineering departments, Iowa State University.
[5] PhD candidate, Aerospace Engineering department, Iowa State University.
[6] Assistant professor of Mechanical Engineering department, Montana State University.
[7] Assistant professor of Aerospace Engineering department, Iowa State University.

Surface tension is modeled using a continuous surface approach. One and two-dimensional simulations are used to demonstrate the method's capabilities.

3.1 Introduction

The reliable atomization and ignition of liquid fuel injected into supersonic combustors is a significant limitation to Scramjet development. Little is known about the primary and secondary breakup processes in supersonic crossflows. A large body of literature exists that describes the breakup behavior of liquid droplets (secondary atomization) after being impacted by a shock wave to induce a strong shear [1]. However, most of the work uses shock waves that still induce subsonic post-shock velocities.

In shock tube experiments a droplet is impacted by a shock wave that passes over the droplet and causes minimal deformation during this interaction. The advantage of this approach is that a drop can be subjected to a step change in ambient flow that is nearly uniform over its surface[2]–[13]. An unequal pressure distribution forms around the droplet after the shock passes and deforms the initially spherical droplet. Interfacial tension and viscous forces resist this deformation and it is the competition between these resistive and pressure forces that determines the evolution of the droplet. Typical breakup modes include vibrational, bag, multimode, sheet-thinning, and catastrophic.

The use of direct numerical simulations has become more common in the last two decades to investigate droplet breakup and atomization behavior. Zaleski et al. [14] performed 2D water column simulations of the Navier-Stokes equations with constant density and viscosity. Igra and Takayama [15] showed experimentally that breakup behavior is similar between a 2D water column and a spherical droplet. Han and Tryggvason [16], [17] solved the axi-symmetric Navier-Stokes equations in order to simulate a spherical droplet fragmentation with a density ratio of 10.

Transitional Weber numbers (We) did not match experiments and it is thought that this may be because most experiments are conducted at much higher density ratios. Aalburg et al. [18] expanded upon this work to simulate drop deformation at higher density ratios but did not have sufficient resolution to simulate breakup.

Quan and Schmidt [19] developed a 3D code with compressibility effects in ambient gas. Chang and Liou [20] developed a stratified flow model that can simulate the interaction of a shock wave with a liquid drop. Initial results indicate good agreement with experimental results of Theofanous et al. [13] at high Mach numbers. Khare et al. [21] used a volume of fluid method to perform full 3-D simulations using the incompressible multi-fluid Navier-Stokes equations and reproduced the transitional Weber numbers reasonably well.

Most of the studies on secondary atomization focus on the breakup of a spherical droplet from a shock wave (experimental) or impulsively started flow (numerical). While most of the numerical simulations of interfacial flows have been incompressible, there have been a few studies[22]–[24] done in compressible flows. Other approaches neglect surface tension and analyze shock wave interactions with either bubbles[25]–[27] or the early stages of droplet deformation[28].

The breakup of droplets is a truly multiscale behavior and requires a multiscale approach. The Parallel Adaptive Wavelet-Collocation Method[29]–[31] is an intrinsically multiscale numerical approach that uses wavelets to determine which points are necessary to represent a solution within some *a priori* prescribed accuracy. In this work, a compressible multiphase interfacial flow methodology is developed within the PAWCM framework.

This paper is organized as follows. First the governing equations used to model the multiphase flow are described in detail. Second, the numerical method used to implement the system of

equations are described. Then some results demonstrating the method's capabilities are presented, followed by conclusions.

3.2 Multi-fluid compressible flow model

Multi-fluid/multi-component simulations are modeled using the quasi-conservative, volume fraction approach Navier-Stokes equations,

$$\frac{\partial(\rho_1\alpha_1)}{\partial t} + \nabla\cdot(\rho_1\alpha_1\boldsymbol{u}) = 0 \tag{3-1}$$

$$\frac{\partial(\rho_2\alpha_2)}{\partial t} + \nabla\cdot(\rho_2\alpha_2\boldsymbol{u}) = 0 \tag{3-2}$$

$$\frac{\partial(\rho\boldsymbol{u})}{\partial t} + \nabla\cdot(\rho\boldsymbol{u}\boldsymbol{u} + p\boldsymbol{I} - \boldsymbol{T}) = \boldsymbol{f} \tag{3-3}$$

$$\frac{\partial\rho e_t}{\partial t} + \nabla\cdot\left((\rho e_t + P\boldsymbol{I})\boldsymbol{u} - \boldsymbol{T}.\boldsymbol{u}\right) = \boldsymbol{f}\cdot\boldsymbol{u} \tag{3-4}$$

$$\frac{\partial\alpha_1}{\partial t} + \nabla\alpha_1 u = \alpha_1\nabla.u, \tag{3-5}$$

where ρ is the total density, $\boldsymbol{u}$ is the vector of velocity components, p is the pressure, e_t is the total energy, α is the volume fraction, $\boldsymbol{I}$ is the identity tensor and $\boldsymbol{T}$ is the stress tensor defined as,

$$\boldsymbol{T} = 2\mu\left(\frac{1}{2}(\nabla\boldsymbol{u} + (\nabla\boldsymbol{u})^T) - \frac{1}{3}(\nabla\cdot\boldsymbol{u})\boldsymbol{I}\right) \tag{3-6}$$

where μ is the shear stress. This coefficient is calculated using the mixture rule $\mu = \alpha_1\mu_1 + \alpha_2\mu_2$[27]. The current focus is on viscous effects and terms associated with thermal diffusion are ignored. Additionally μ_1 and μ_2 are modeled as constants so that μ is a function of composition only. Both assumptions, however, can be lifted, when appropriate terms are used to calculate temperature[32].

All equations are written in conservative form except the advection equation for the volume fraction. It has been shown that this equation is needed to calculate and preserve pressure equilibrium at the fluid interface and including the divergence term maintains $0 \leq \alpha_1 \leq 1$.

This set of equations is written for two fluids, but it is easily extendable to account for more than two fluids by adding a density and advection equation. Moreover, these equations conserve the mass of each fluid and the energy of the system and they do not generate spurious oscillations at the interface (necessary criteria for a multiphase simulation).

Table 3-1 Parameters used in stiffened gas EOS[27].

Fluid	$\rho[kg/m^3]$	γ	$\pi^{\infty}[GPa]$	$c[m/s]$
Air	1.205	1.4	0	343
Water	998	4.4	1	1450
Helium	0.166	1.67	0	1008

The system of equations is closed using the stiffened gas equation of state (EOS) to account for different phases in the flow,

$$p + \gamma\Pi^{\infty} = (\gamma - 1)\left(\rho e_t - \frac{1}{2}\rho \boldsymbol{u}\boldsymbol{u}\right), \tag{3-7}$$

where γ is the multicomponent ratio of specific heats and $\Pi^{\infty}(Pa)$ is the multicomponent fitting parameter for different components in the flow.Following the mixture rules in the interface capturing method ($\rho_1\alpha_1 + \rho_2\alpha_2 = \rho, \alpha_1 + \alpha_2 = 1$), γ and Π^{∞} are found using the following:

$$\frac{1}{\gamma - 1} = \frac{\alpha_1}{\gamma_1 - 1} + \frac{1 - \alpha_1}{\gamma_2 - 1} \tag{3-8}$$

$$\frac{\gamma\Pi^{\infty}}{\gamma - 1} = \frac{\alpha_1\gamma_1\pi_1^{\infty}}{\gamma_1 - 1} + \frac{(1 - \alpha_1)\gamma_2\pi_2^{\infty}}{\gamma_2 - 1} \tag{3-9}$$

where values of γ and π^{∞} are listed in Table 1 for air, water, and Helium. The speed of sound is defined as $c = \sqrt{\gamma(p + \pi^{\infty})/\rho}$.

Any additional forces being applied to the fluid are contained in $\boldsymbol{f}$. In multiphase flows, one of the most important forces is the capillary force. Thus, the corresponding force and power terms are added to the system of equations using a continuum surface force model (CSF),

$$\boldsymbol{f} = -\sigma\kappa\nabla\alpha_1 \tag{3-10}$$

$$\boldsymbol{f}.\boldsymbol{u} = -\sigma\kappa\boldsymbol{u}\cdot\nabla\alpha_1, \tag{3-11}$$

where $\sigma(N/m)$ is the surface tension and κ is the curvature of the interface for the higher density fluid (in this case α_1). The curvature κ is calculated using

$$\kappa = \nabla\cdot\boldsymbol{n}, \tag{3-12}$$

where $\boldsymbol{n} = \frac{\nabla\alpha_1}{|\nabla\alpha_1|}$ is the normal vector. Details on normal vector calculations are described in detail in the next section.

Finally, the above equations are non-dimensionalized using a reference density, speed of sound, and length scale. This introduces two non-dimensional parameters, namely the acoustic Reynolds and Weber numbers:

$$Re_a = \rho_0 c_0 l/\mu_0 \tag{3-13}$$

$$We_a = \rho_0 c_0^2 l/\sigma. \tag{3-14}$$

3.3 Numerical Implementation

The Parallel Adaptive Wavelet Collocation Method (PAWCM), makes use of second generation wavelets to dynamically adapt the grid to localized structures in the flow in time and space[29]–[31]. This approach allows the solution to be approximated using a subset of the points

that would normally be used with a uniform grid scheme. Dynamic domain partitioning is used for parallel computations and the method has been shown to scale well on up to 2048 processors[31].

In this paper, a second order finite difference discretization for the spatial terms are used along with a third order Total Variation Diminishing (TVD) Runge-Kutta (RK) time integration scheme. A modified version of the original hyperbolic solver developed for the PAWCM[33] that uses a TVD flux limiter to add artificial viscosity to the regions where a lower order flux is required. Therefore, for the tests that include sharp density and pressure jumps (e.g. shock waves), the order of accuracy drops to between first and second order in those regions. Similar to flux terms, the source terms are discretized in a consistent form.

3.3.1 Interface capturing model

For simplicity, both the shock and fluid interface are captured over several cells using an interface/shock capturing approach. The diffusive nature of the numerical scheme requires the fluid interface to be steepened for certain variables. After the fluid evolution is solved for in physical time, the interface is steepened by iterating in false time τ.

The employed interface steepening technique uses a combination of interface and density sharpening to minimize the thickness of the numerically diffused interface. This approach uses a semi-conservative level set function where the volume fraction of the liquid phase indicates the interface. This function takes the values zero or one on either side of the interface with $\alpha_1 = 0.5$ indicating the actual interface location. The boundary between immiscible materials is modeled by the smooth variation of α_1 between these limits. Following the approach outlined by Shukla et al. [26], the interface function is steepened in false time using a compression step

$$\frac{d\alpha_1}{d\tau} = \boldsymbol{n} \cdot \nabla\left(\epsilon_h(\boldsymbol{n} \cdot \nabla\alpha_1) - \alpha_1\,(1-\alpha_1)\right), \tag{3-15}$$

where $\boldsymbol{n}$ is the normal vector and ϵ_h is a length-scale on the order of the grid spacing. In this equation the first term on the right hand side serves as a diffusion term to maintain nonlinear stability and the second term steepens the interface.

Since the density is a function of local flow conditions in compressible flows a separate steepening equation is required for each density equation. The approach outlined by Shukla et al. [26] is used to steepen the density. The compression step for the phase 1 density takes the form

$$\frac{d\alpha_1\rho_1}{d\tau} = H\boldsymbol{n}\cdot\left[\nabla\left(\epsilon_h.\nabla(\alpha_1\rho_1)\right) - (1-2\alpha_1)\nabla(\alpha_1\rho_1)\right] \tag{3-16}$$

The same approach is used for phase 2. The term H is a smoothed Heaviside function

$$H = \tanh\left[\left(\frac{(\alpha_1(1-\alpha_1)}{10^{-2}}\right)^2\right]. \tag{3-17}$$

This function localizes the compression of density to the interface region. The interface function and the density for each phase are steepened after each timestep. A single steepening iteration is used after each step in physical time. A false time CFL condition is established to calculate the false time step size $\Delta\tau = CFL_\tau \cdot h$, where h is the smallest grid size in the domain and CFL_τ is the steepening CFL number. Values for this parameter vary between 0.1 and 0.5 depending upon the desired steepness.

3.3.2 Normal vector calculation

Normal vectors are required to evaluate the right-hand side of the steepening equation and calculating the surface tension force. In both shock and interface capturing schemes, the representation of a sharp physical interface is most realistic if the interface thickness is minimized. This corresponds to making ϵ_h as small as possible during the compression step. However, accurate computation of the gradients of the interface function, α_1, particularly those that define normal, are well-behaved only if α_1 is sufficiently resolved with the computational mesh.

Otherwise, numerical artifacts appear and quickly disrupt the attractive properties of the compression scheme. This is in contrast with the modeling objective of maintaining a sharp interface. In order to address this issue, Shukla et. al.[26] propose an auxiliary function

$$\psi = \frac{\alpha_1^{\beta}}{\alpha_1^{\beta} + (1-\alpha_1)^{\beta}}, \quad \beta < 1 \tag{3-18}$$

that is more continuous across the fluid interface and provides gradients that contain less numerical noise. This function can be used to calculate the same normal vector values as would be calculated using α_1, but uses smoother gradients. The normal vector is then represented as

$$\boldsymbol{n} = \frac{\nabla \alpha_1}{|\nabla \alpha_1|} = \frac{\nabla \psi}{|\nabla \psi|} . \tag{3-19}$$

In this function a small value of β alleviates the problems associated the steep gradients of α_1 because the width of the hyperbolic tangent profile for ψ is $1/\beta$ times that of α_1. In this work, $\beta = 0.1$ is usually sufficient to provide smooth and well-defined normal vectors.

An additional advantage of using the smoother function ψ to calculate the normal vectors, instead of α_1, is that the curvature κ contains less noise after calculating a second derivative with respect to ψ. This approach eliminates the need to filter oscillations in the curvature retroactively.

3.4 Numerical Results

To show the robustness of the proposed method to solve compressible multiphase flows, 1-D and 2-D simulations have been performed. For brevity, only five test problems are contained here. Each problem has its own unique properties that assess the performance of the numerical method.

3.4.1 1 D Advection of an isolated multiphase interface

The advection of an isolated water/air interface under atmospheric pressure in a periodic domain is a simple test that determines whether the numerical method produces any spurious

oscillations at the fluid interface for pressure and velocity[27]. These oscillations, which appear initially in pressure terms ($O(10^{-6})$ to $O(10^{-1})$), may occur when the interface capturing method is not implemented correctly and/or the conservative sharpening technique used is not consistent with the associated numerical implementation. No surface tension is used in this 1D simulation, but one iteration of steepening is applied with a $CFL_\tau = 0.25$.

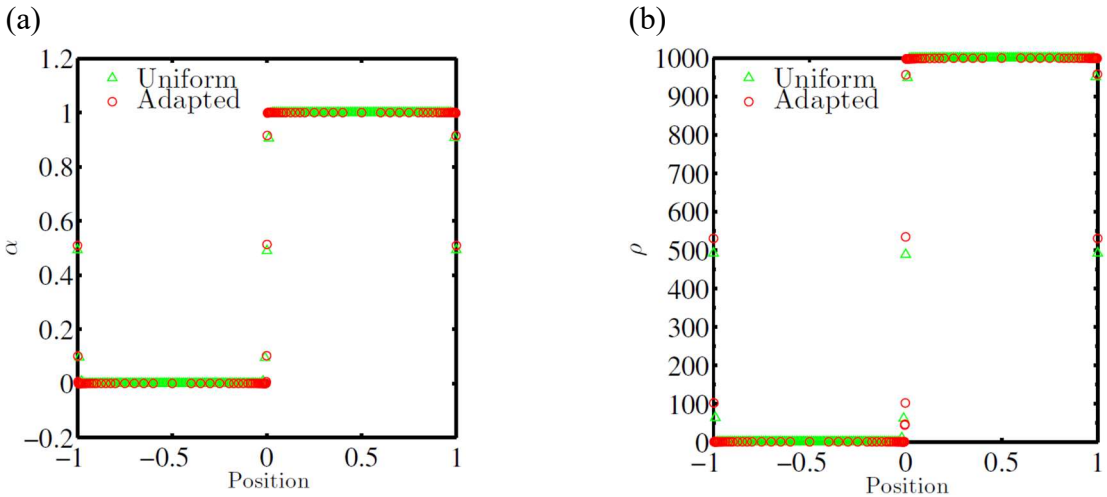

Figure 3-1 Volume fraction (a) and density (b) for the 1-D advection problem.

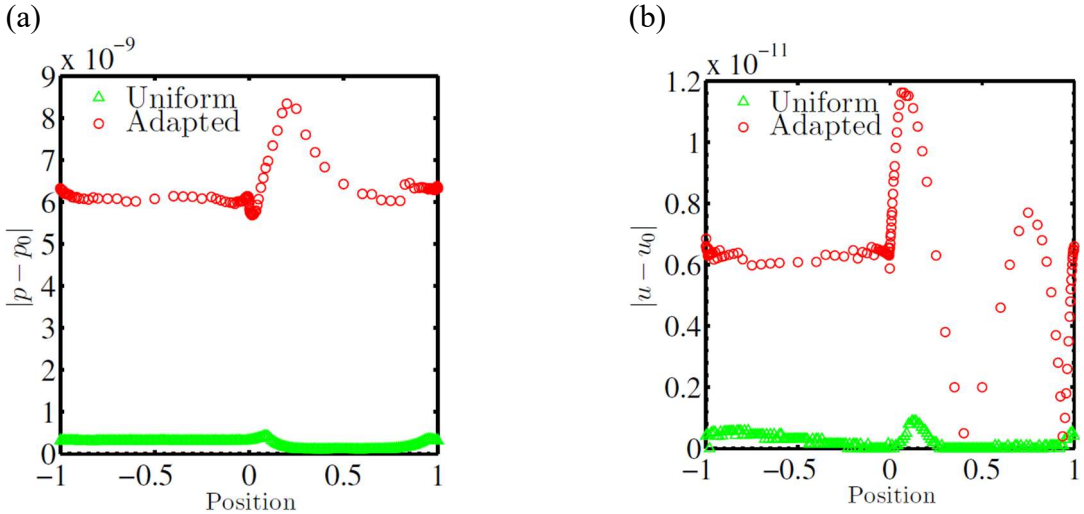

Figure 3-2 Error in (a) pressure and (b) velocity fluctuations for the 1-D advection problem.

3.4.2 1D Advection of an isolated multiphase interface

The initial condition for the problem normalized by the density and speed of sound in water is[27]:

$$(\alpha_1\rho_1, \alpha_2\rho_2, u, P, \alpha_1) = \begin{cases} (1.204 \times 10^{-3}, 0, 0.01, 4.82 \times 10^{-5}, 1) & -1 \le x \le 0 \\ (0, 1, 0.01, 4.82 \times 10^{-5}, 0) & 0 \le x \le 1 \end{cases} \quad (3\text{-}20)$$

The solution is integrated in time with a CFL=0.5 for one period until $t = 20$. The volume fraction and density at the end of the simulation are shown in Figure 3-1 for solutions on adaptive and uniform grids (200 cells). The figures show that only a minimal number of points are used across the interface and the adaptive method has the same solution with around half the points as the uniform grid. Also the method is able to handle high density ratios with minimal amounts of numerical diffusion.

In order to demonstrate the magnitude of spurious oscillations at the interface, the error in pressure and velocity are plotted in Figure 3-2. Both uniform and adaptive grids create minimal oscillations (error $\sim O(10^{-9})$), which confirms the ability of the method to minimize such errors, especially in an interface capturing method with high density ratios.

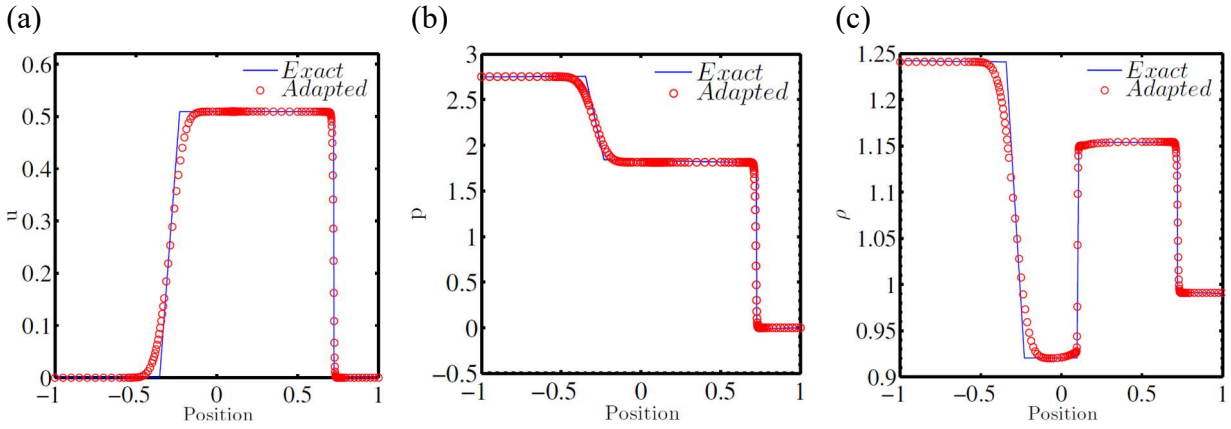

Figure 3-3 Velocity (a), pressure (b), and density (c) distributions for the 1-D Riemann problem.

3.4.3 Gas-Liquid Riemann Problem

The second problem to validate the interface compression in 1D is the gas liquid Riemann problem where both shock and interface exist in the numerical domain. This problem demonstrates the robustness of the solver when the shock capturing and interface capturing are functioning at the same time. In this problem a highly compressed air on the left is adjacent to water at atmospheric pressure on the right. The initial condition is given by[27]

$$(\alpha_1\rho_1, \alpha_2\rho_2, u, P, \alpha_1) = \begin{cases} (1.241, 0, 2.573, 1.24) & -1 \leq x < 0 \\ (0.991, 0, 3.059 \times 10^{-4}, 0) & 0 \leq x \leq 1 \end{cases} \quad (3\text{-}21)$$

The simulation is performed with a base grid of 20 points with 7 levels of refinement for an effective uniform grid resolution of 2,560 points. Of these 2,560 points, the solution is represented with around 100 points. The CFL number used for the time integration is 0.5 and the simulation is run until $t = 0.2$. Similar to the previous problem, a single step of steepening is performed in pseudo-time with a CFL_τ number of 0.25. Figure 3-3 compares the analytical solution with the numerical simulation for velocity, pressure and density. The results show that the method is able to predict the correct location of the transmitted and reflected shocks. As should be expected, the pressure and velocity are constant across the interface.

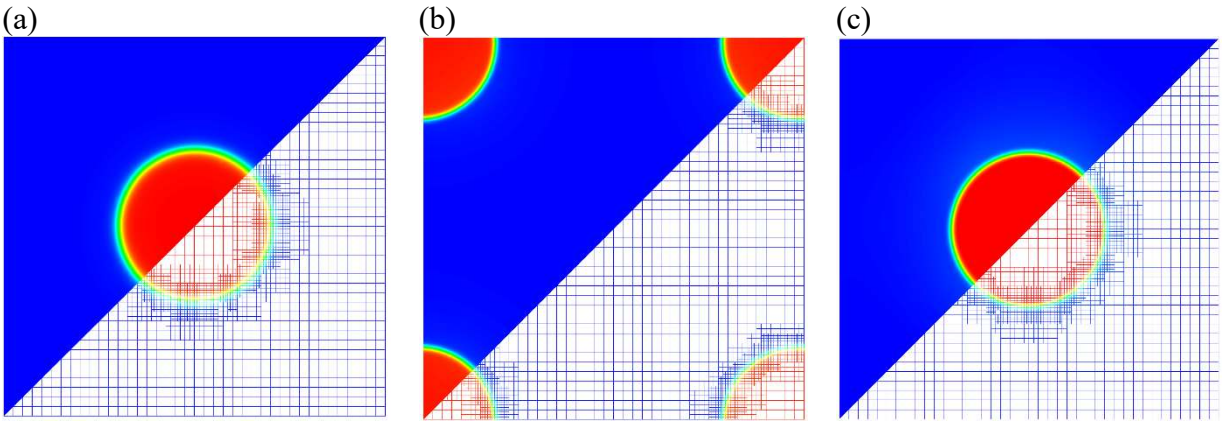

Figure 3-4 Profile of interface function at a) the initial condition, b) after half a period, and c) after 10 periods.

3.4.4 2D Advecting Water Column

The first two-dimensional test case is the advection of a water column. When a water column is advecting the spurious oscillations at the material interface can contaminate the fine flow features and have a negative impact on both the reliability and quality of computed solutions[27]. This can lead to interface deformation and mass loss. Therefore, the main challenge of this problem is shape preservation and mass conservation while moving. In this problem the rectangular computational domain is $\Omega = [-2.5, 2.5] \times [-2.5, 2.5]$. A water column of unit radius is placed in air with its center initially located at the origin. The rest of the initial condition for this problem, normalized by gas density and speed of sound, is

$$r = \sqrt{x^2 + y^2} \tag{3-22}$$

$$\alpha_1 = \frac{1}{2}\left(1 + \tanh\left(\frac{r-1}{\Delta}\right)\right)$$

$$(\alpha_1\rho_1, \alpha_2\rho_2, u, v, P) = \begin{cases} (10^3, 0, 0.5, , 0.5, 1) & r \leq 1 \\ (0, 1, 0.5, 0.5, 1) & r > 1 \end{cases}$$

where phase 1 is water, $\alpha_1 = 1$, and phase 2 is air, $\alpha_1 = 0$. The maximum resolution grid spacing Δ is used in the initial condition to ensure that the initial profile always uses the same number of grid points across the interface. There is no molecular viscosity in this test case.

The solution is computed on an adaptive grid with two refinement levels to provide an effective grid of 160×160 points. Figure 3-4 demonstrates the interface function profile at (a) the initial condition, (b) after half a period, and (c) after 10 periods of advection. The water column moves diagonally in a periodic domain while the grids continuously adapt to the interface location. Figure 3-4(a) shows that the initial profile of the interface is smeared over several points. At the later times shown in Figure 3-4(b) and (c), the compression scheme sharpens the interface and maintains a constant interface thickness of a few grid cells throughout the computations. Figure

3-4(c) also confirms that the method does not produce any noticeable oscillations near the interface.

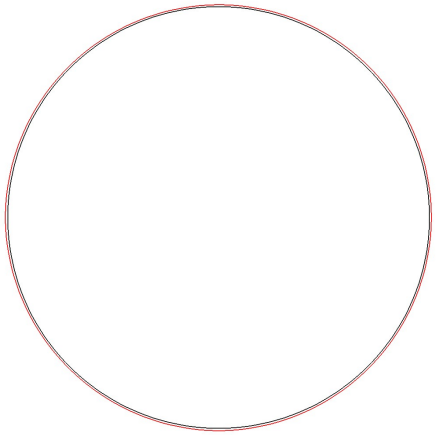

Figure 3-5 Comparison of the contour plot of interface location at initial condition (red line) and after 10 periods of advection (black line).

A contour plot that illustrates the interface location ($\alpha_1 = 0.5$) for the initial condition and after 10 periods of advection is shown in Figure 3-5. This shows that the interface size and shape is preserved and the mass is mostly conserved after several periods. The black circle after 10 periods has a smaller diameter than the initial red circle. This change is associated with the initial thickness of the interface being larger than the steady-state thickness that is maintained through a majority of the simulation.

3.4.5 Shock water column interaction (no surface tension)

Now we consider the interaction of a strong planar shock wave ($M = 1.67$) interacting with a water column. The shock moves to the left and has an initial position of $x = 15$. The water column has an initial diameter $D = 2$ and is located at $x = 10$. The computational domain is $\Omega = [-20, 20] \times [-5, 5]$ and the equation of state parameters for water and air are given in Table. 3.1. The solution is computed on an adaptive grid with 2560×640 effective grid points. Periodic

boundary conditions are applied for the top and bottom boundaries. The left boundary is an outflow boundary. On the right boundary the post-shock condition is imposed. The Initial conditions are

$$r = \sqrt{(x-10)^2 + y^2} \tag{3-23}$$

$$\alpha_1 = \frac{1}{2}\left(1 + \tanh\left(\frac{r-1}{2\epsilon_h}\right)\right)$$

$$(\alpha_1\rho_1, \alpha_2\rho_2, u, v, P) = \begin{cases} (10^3\alpha_1, (1-\alpha_1), 0, 0, 0.714) & x < 10 \\ (0, 2.111, -0.892, 0\ , 2.142) & x > 10 \end{cases}.$$

Figure 3-6 shows the early interaction of the shock wave with the water column. The results agree qualitatively with the results of Igra et al. [34]. The incident shock and the subsequent wave systems in the wake of the deforming cylinder are visualized using numerical Schlieren images of the gas phase density (defined $|\nabla\rho_2|$) in the top portion of each figure. The bottom of each figure shows the dynamically adaptive grid colored by pressure.

Transmitted and reflected shocks are generated from the impact of the incident shock with the water column. The interaction of these waves with the interface leads to interfacial instabilities at the water-air interface and the wake structure behind the water column. There is a high-pressure region associated with the forward stagnation point, behind the reflected wave. A transition from a shock reflection to a Mach reflection happens at a critical angle behind the water column. This transition leads to maximum drag experienced by the column[28]. This phenomena has been reported in the literatures for both cylinders and spheres[34]. High pressure at the rear stagnation point is generated due to the convergent Mach stems behind the column.

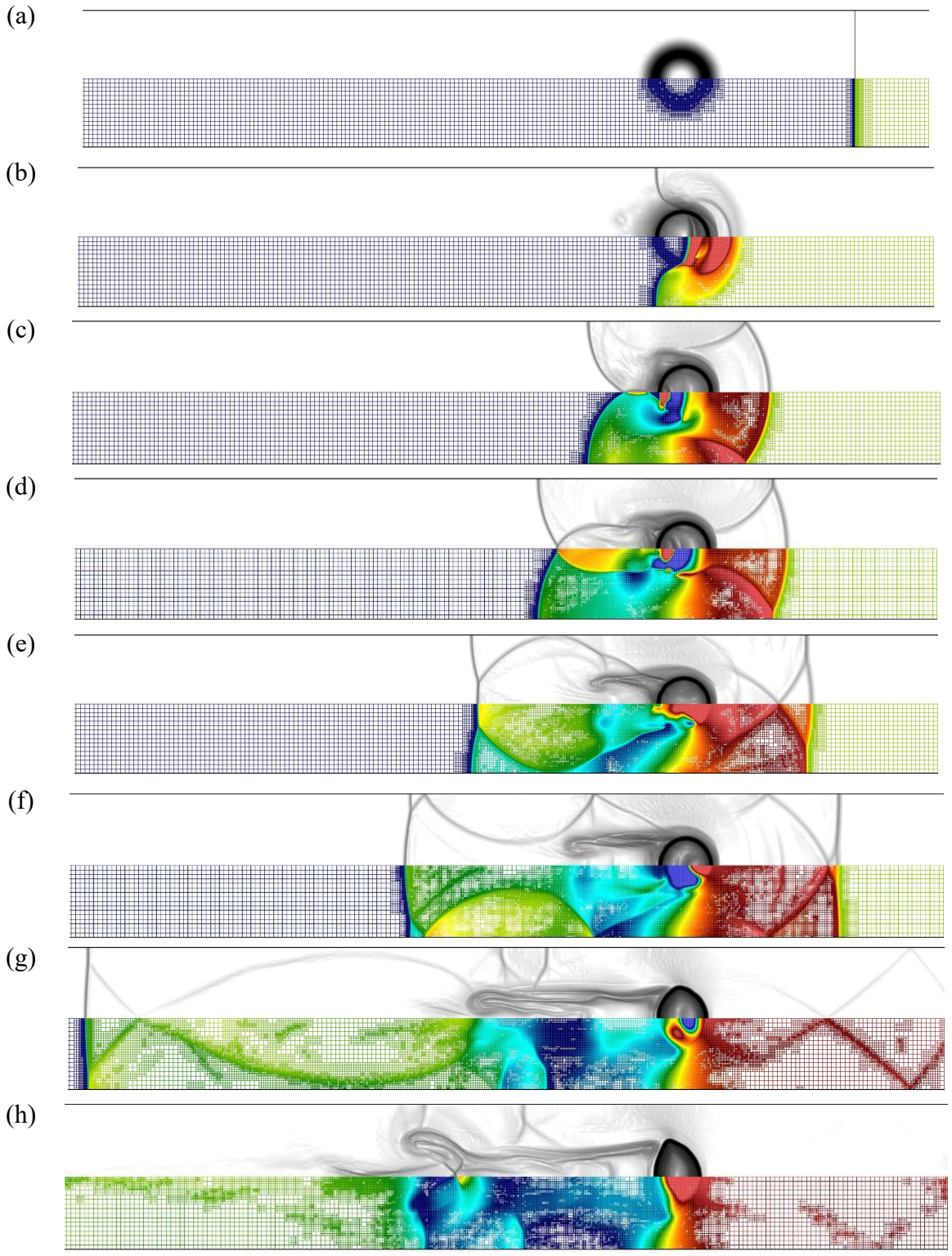

Figure 3-6 Numerical Schlieren images (top) and dynamic adaptive grids colored by pressure contours (bottom) of a shock wave passing through a liquid droplet at $t =$ (a) 0.00 (b) 4.8 (c) 7.5 (d) 9.00 (e) 12.00 (f) 14.80 (top to bottom, left to right).

It can be seen that the grid is localized to regions of the flow that have localized structures necessary of increased resolution. The results demonstrate that the dynamic grid adaptation used in the PAWCM approach makes the simulation of truly multiscale behavior such as this more computationally feasible for large-scale simulations.

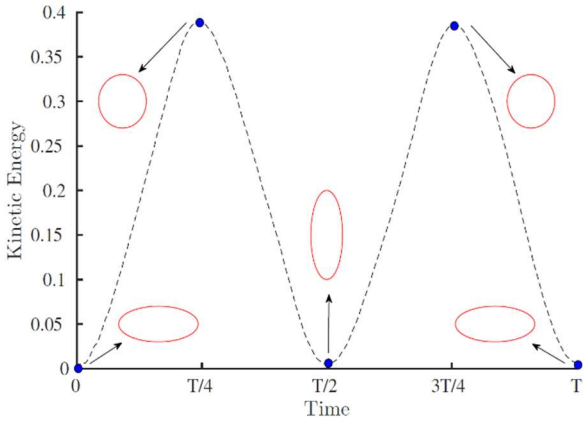

Figure 3-7 Kinetic energy versus time for a period of oscillation.

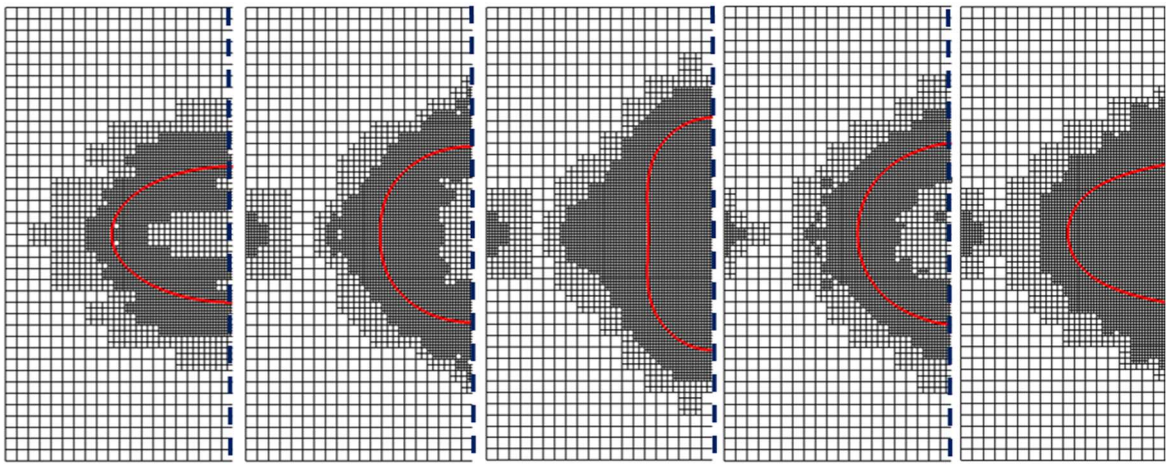

Figure 3-8 Grid adaptation during one period for the oscillating ellipse problem with 5 levels of adaptation.

3.4.6 Oscillating Ellipse

The last problem in this paper is an oscillating ellipse shaped water droplet with surface tension present. The initial pressure is uniform atmospheric pressure everywhere with zero velocity. The surface tension forces deform the shape into a neutral shape (preferably a circle), because the potential energy (kinetic energy) becomes a minimum (maximum) in that phase ($t = T/2$). The inward acting momentum in the x-direction causes the ellipse to elongate in the y-direction ($t = 3T/2$). The same events move the ellipse interface back to the original shape ($t = T$). In order to illustrate the oscillation behavior, the globally integrated compressible kinetic energy

$$KE = \iint (\rho u^2 + \rho v^2) dA \tag{3-24}$$

is evaluated at each time step. Figure 3-7 plots the KE over a single period T. It has been shown that the non-dimensional time period it takes for an ellipse ($x^2/a^2 + y^2/b^2 = 1$) to move back to the original shape after being disturbed by the surface tension forces is[22]:

$$T_{exact} = 2\pi \sqrt{\frac{We\left(1 + \frac{\rho_2}{\rho_1}\right) R^3}{6}} \tag{3-25}$$

where $R = \sqrt{ab}$. For $We = 1$, density ratio of 1000, and $Re = 100$ with $R = \sqrt{3/5 \times 5/3}$ for the ellipse, the period of oscillation becomes $T_{exact} = 81.15$. The simulation shows that this time is roughly about $T_{numerical} \approx 86.5$. It is suspected that the difference exists because secondary oscillation modes also exist. Further details on these other modes can be found in Ref. [22].

Figure 3-8 shows how the grid adapts to the droplets evolution with time. The high localization of the grid to the surface makes the PAWCM method highly suitable to capturing the multiscale nature of atomization processes.

3.4.7 Shock water column interaction with surface tension effect

A Mach 3 shock in air impacting a water column with unity radius is simulated. The domain is $[5, 10] \times [-6,6]$ and extrapolation boundary conditions are applied on all four boundaries. The non-dimensional initial conditions are given by

$$(\rho_l \alpha_l, \rho_g \alpha_g, u, v, p) = \begin{cases} (0,3.857,2.629, 0,10,333) & x < -1 \\ (10\alpha_l, (1-\alpha_l), 0,0,1+\Delta p) & otherwise \end{cases}$$

Where $\gamma_l = 4.4, \pi_{\infty,l} = 60, , \gamma_g = 1.4$ and $\pi_{\infty,g} = 0$ and

$$\alpha_l = 1 - 0.5\left(1 + \tanh\left(\frac{r-0.5}{4\epsilon_h}\right)\right)$$

With $r = \sqrt{x^2 + y^2}$ and $\epsilon_h = 0.72h$. The acoustic Weber number (We_a) is set to 0.75,1.5, 3 making the initial pressure jump distribution $\Delta p = \alpha_l / 0.5 We_a$ for the simulation with surface tension. This corresponds to a physical Weber number of 20, 40, 160 based on the droplet diameter and post-shock velocity. All simulations were performed with a CFL of 0.6 with ten curvature filtering iterations. Three steps of interface compression were performed per physical time step with CFL_τ of 0.07.

Figure 3-9 shows the early interaction of the shock wave with the water column for three cases with Weber numbers of 20, 40, 160, 320 and the case with no surface tension effect. In this figure the interface dynamics and the incident shock and the subsequent wave systems in the wake of the deforming cylinder are visualized using numerical Schlieren images in the top portion of each figure. The bottom of each figure shows the dynamically adaptive grid colored by pressure. The surface tension force actively combat the deformation of droplet as evidenced in this figure. The smaller the Weber number is the larger the effect of surface tension force will be. This effect is more obvious on the top and bottom of the water column where the curvature is larger which leads

to the larger surface tension effect. In this area the surface tension effect is combating the deformation under the effect of recirculation of the flow around the water column.

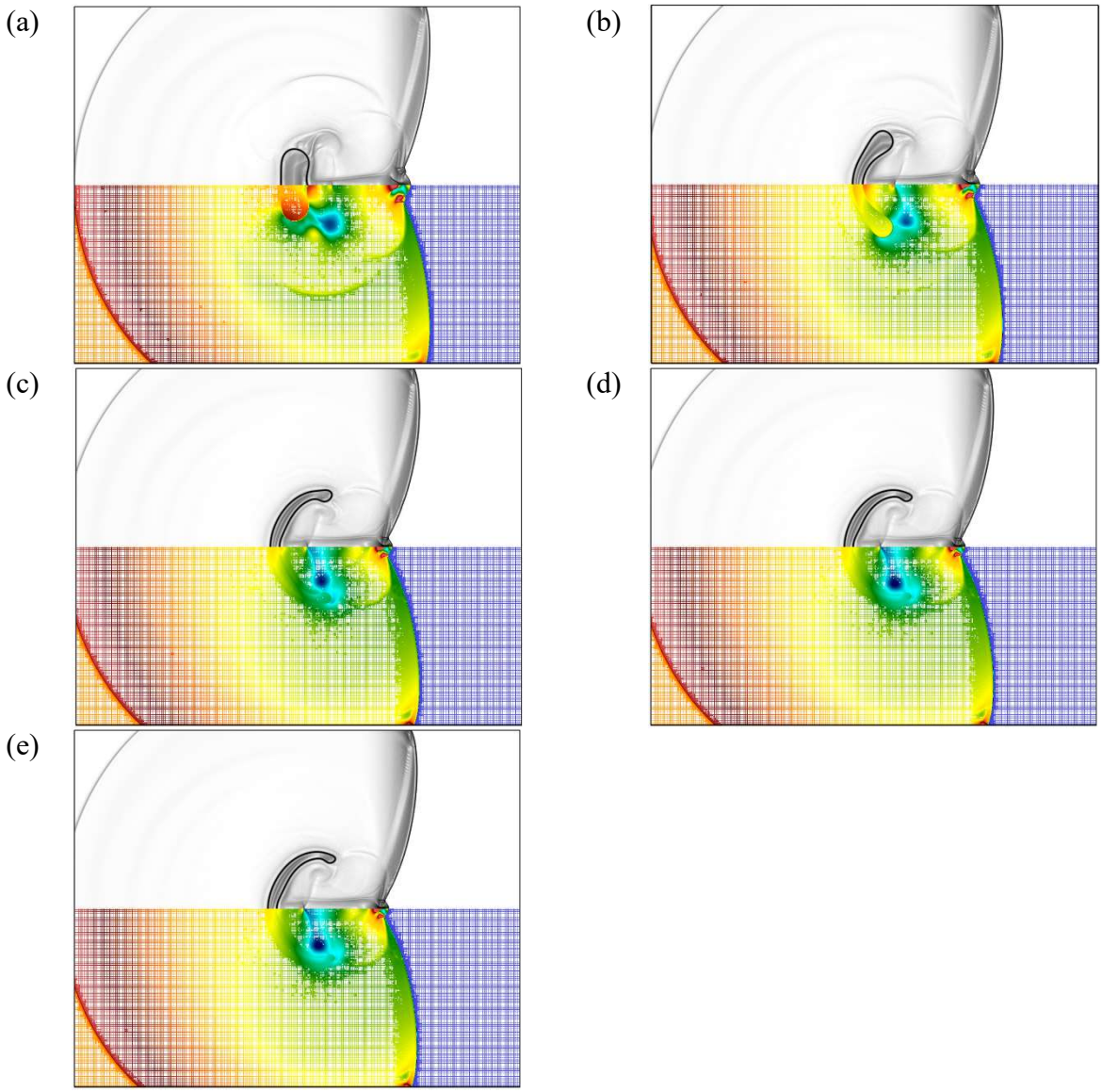

Figure 3-9 Effect of surface tension on the evolution of water column interface (a) $We = 20$ (b) $We = 40$ (c) $We = 160$ (d)$We = 320$ (f) No surface tension ($We = \infty$)

Figure 3-10 depicts the evolution of interface under the effect of shock wave when the Weber number is 40. After the incident shock impacts the water column the deformation starts. Because the density ratio is only 10 instead of 1000, therefore, the inertial force of the water column is 100 times smaller than the actual water column.

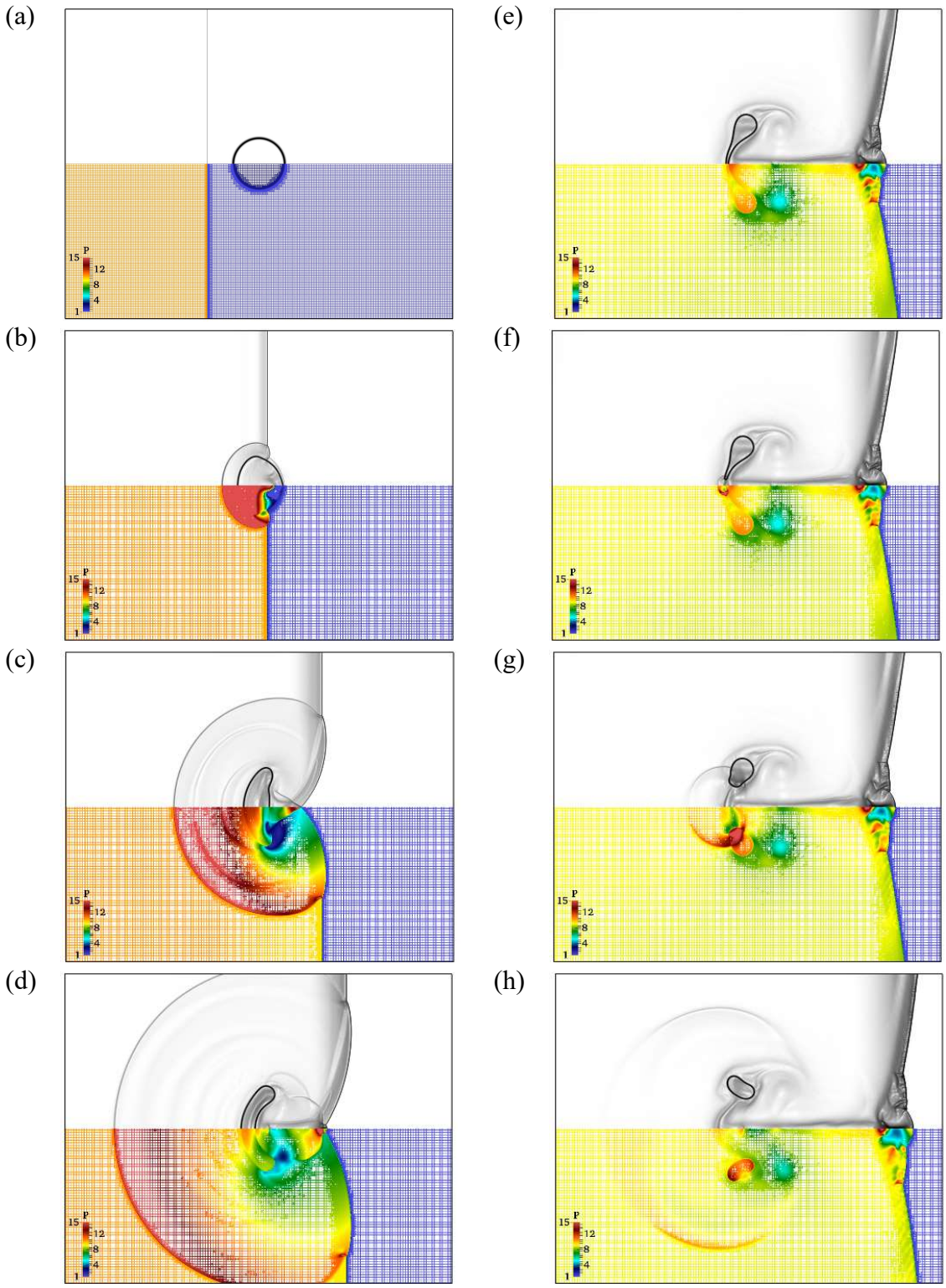

Figure 3-10 Evolution of water column interface with We=40 under the effect of incident shock with Mach=3

The shock wave is transmitted to the droplet and the pressure wave goes back and forth inside the droplet with a separation point forming in front of the droplet. The recirculation of the air in the wake elongates the water column which leads to the bag formation. The bag gets thinner and finally it breaks into two droplets. At the breakup location a reflected shock forms and propagates.

3.5 Conclusion

A compressible multiphase flow solver with surface tension was developed for the Parallel Adaptive Wavelet-Collocation Method. One-dimensional test problems show the ability to resolve both shock and interfaces over just a few points. Spurious oscillations in velocity and pressure are minimal across the interface. A two-dimensional test case for an advecting water column in air demonstrates the method's ability to maintain a steep fluid interface for long durations. Subsonic shock interaction with water column shows the ability of the code to capture the shock and interface dynamics at the same time. An oscillating ellipse with surface tension was tested and the oscillation period matches the theoretical oscillation period reasonably well. Finally, the solver is applied to a supersonic shock-droplet interaction in the presence of surface tension force. For all cases, the grid dynamically adapts to the solution illustrating the capability of the approach to handle large problems with a large range of scales.

3.6 Acknowledgements

This work is supported by Taitech, Inc. under sub-contract TS15-16-02-004 (primary contract FA8650-14-D-2316). This paper is a collaborative work. I would like to acknowledge the contribution of my colleague, Mohamad Aslani, for incorporating the five-equation model in the solver and helping me to prepare some of the test case.

References

[1] D. R. Guildenbecher, C. López-Rivera, and P. E. Sojka, "Secondary atomization," *Exp. Fluids*, vol. 46, no. 3, pp. 371–402, Mar. 2009.

[2] J. O. Hinze, "Fundamentals of the hydrodynamic mechanism of splitting in dispersion processes," *AIChE J.*, vol. 1, no. 3, pp. 289–295, Sep. 1955.

[3] J. A. Nicholls and A. A. Ranger, "Aerodynamic shattering of liquid drops.," *AIAA J.*, vol. 7, no. 2, pp. 285–290, Feb. 1969.

[4] B. E. Gel'fand, S. A. Gubin, S. M. Kogarko, and S. P. Komar, "Singularities of the breakup of viscous liquid droplets in shock waves," *J. Eng. Phys.*, vol. 25, no. 3, pp. 1140–1142, Sep. 1973.

[5] A. WIERZBA and K. TAKAYAMA, "Experimental investigation of the aerodynamic breakup of liquid drops," *AIAA J.*, vol. 26, no. 11, pp. 1329–1335, Nov. 1988.

[6] L.-P. Hsiang and G. M. Fa~tht, "NEAR-LIMIT DROP DEFORMATION AND SECONDARY BREAKUP," *Int. J. Muhiphase Flow*, vol. 18, no. 5, pp. 635–652, 1992.

[7] L.-P. Hsiang and G. M. Faeth~, "DROP PROPERTIES AFTER SECONDARY BREAKUP," *Int. J. Multiph. Flow*, vol. 19, no. 5, pp. 721–735, 1993.

[8] L.-P. Hsiang and G. M. Faeth, "Drop Deformation and Breakup Due To Shock Wave and Steady Disturbances," *Int. J. Multiph. Flow*, vol. 21, no. 4, pp. 545–560, 1995.

[9] W.-H. Chou, L.-P. Hsiang, and G. M. Faeth, "Temporal properties of drop breakup in the shear breakup regime," *Int. J. Multiph. Flow*, vol. 23, no. 4, pp. 651–669, Aug. 1997.

[10] D. D. Joseph, J. Belanger, and G. S. Beavers, "Breakup of a liquid drop suddenly exposed to a high-speed airstream BT - Gad Hetsroni: a festschrift issue on the occasion of his 65th birthday," *Int. J. Multiph. Flow*, vol. 25, pp. 1263–1303, 1999.

[11] D. D. Joseph, G. S. Beavers, and T. Funada, "Rayleigh–Taylor instability of viscoelastic drops at high Weber numbers," *J. Fluid Mech.*, vol. 453, pp. 109–132, 2002.

[12] Z. Dai and G. M. Faeth, "Temporal properties of secondary drop breakup in the multimode breakup regime," *Int. J. Multiph. Flow*, vol. 27, pp. 217–236, 2001.

[13] T. G. Theofanous, G. J. Li, and T. N. Dinh, "Aerobreakup in Rarefied Supersonic Gas Flows," *J. Fluids Eng.*, vol. 126, no. July 2004, p. 516, 2004.

[14] S. Zaleski, J. Li, and S. Succi, "Two.-Dimensional Navier-Stokes Simulation of Deformation and Breakup of Liquid Patches," *Phys. Rev. Lett.*, vol. 75, no. 2, 1995.

[15] D. Igra and K. Takayama, "Numerical simulation of shock wave interaction with a water column," *Shock Waves*, vol. 11, no. 3, pp. 219–228, Sep. 2001.

[16] J. Han and G. Tryggvason, "Secondary breakup of axisymmetric liquid drops. I. Acceleration by a constant body force," *Phys. Fluids*, vol. 11, no. 12, pp. 3650–3667, Dec. 1999.

[17] J. Han and G. Tryggvason, "Secondary breakup of a axisymmetric liquid drops. II. Impulsive acceleration," *Phys. Fluids*, vol. 13, no. 6, pp. 1554–1565, 2001.

[18] C. Aalburg, ¤ B Van Leer, and G. M. Faeth, "Deformation and Drag Properties of Round Drops Subjected to Shock-Wave Disturbances," *AIAA J.*, vol. 41, no. 12, 2003.

[19] S. Quan and D. Schmidt, "Direct numerical study of a liquid droplet impulsively accelerated by gaseous flow," *Phys. Fluids*, vol. 18, pp. 1–9, 2006.

[20] C. H. Chang and M. S. Liou, "A robust and accurate approach to computing compressible multiphase flow: Stratified flow model and AUSM+-up scheme," *J. Comput. Phys.*, vol. 225, pp. 840–873, 2007.

[21] P. Khare, D. Ma, X. Chen, and V. Yang, "Breakup of Liquid Droplets," *ICLASS, 12th Trienn. Int. Conf. Liq. At. Spray Syst. Heidelberg, Ger.*, pp. 1–8, 2012.

[22] G. Perigaud and R. Saurel, "A compressible flow model with capillary effects," *J. Comput. Phys.*, vol. 209, no. 1, pp. 139–178, 2005.

[23] B. Braconnier and B. Nkonga, "An all-speed relaxation scheme for interface flows with surface tension," *J. Comput. Phys.*, vol. 228, no. 16, pp. 5722–5739, 2009.

[24] R. K. Shukla, "Nonlinear preconditioning for efficient and accurate interface capturing in simulation of multicomponent compressible flows," *J. Comput. Phys.*, vol. 276, pp. 508–540, 2014.

[25] E. Johnsen and T. Colonius, "Compressible Multicomponent Flow Calculations and Shock-Bubble Interaction," no. September, 2006.

[26] R. K. Shukla, C. Pantano, and J. B. Freund, "An interface capturing method for the simulation of multi-phase compressible flows," *J. Comput. Phys.*, vol. 229, no. 19, pp. 7411–7439, 2010.

[27] V. Coralic and T. Colonius, "Finite-volume WENO scheme for viscous compressible multicomponent flows," *J. Comput. Phys.*, vol. 274, pp. 95–121, 2014.

[28] J. C. Meng and T. Colonius, "Numerical simulations of the early stages of high-speed droplet breakup," *Shock Waves*, vol. 25, no. 4, pp. 399–414, Jul. 2015.

[29] O. V Vasilyev and C. Bowman, "Second-Generation Wavelet Collocation Method for the Solution of Partial Differential Equations," *J. Comput. Phys.*, vol. 165, no. 2, pp. 660–693, Dec. 2000.

[30] O. V. Vasilyev, "Solving Multi-dimensional Evolution Problems with Localized Structures using Second Generation Wavelets," *Int. J. Comut. Fluid Dyn.*, vol. 17, no. 2, pp. 151–168, Mar. 2003.

[31] A. Nejadmalayeri, A. Vezolainen, E. Brown-Dymkoski, and O. V. Vasilyev, "Parallel adaptive wavelet collocation method for PDEs," *J. Comput. Phys.*, vol. 298, pp. 237–253, 2015.

[32] S. Alahyari Beig and E. Johnsen, "Maintaining interface equilibrium conditions in compressible multiphase flows using interface capturing," *J. Comput. Phys.*, vol. 302, pp. 548–566, 2015.

[33] J. D. Regele and O. V. Vasilyev, "An adaptive wavelet-collocation method for shock computations," *Int. J. Comut. Fluid Dyn.*, vol. 23, no. 7, pp. 503–518, 2009.

[34] H. Tanno, K. Itoh, T. Saito, A. Abe, and K. Takayama, "Interaction of a shock with a sphere suspended in a vertical shock tube," *Shock Waves*, vol. 13, no. 3, pp. 191–200, Nov. 2003.

CHAPTER 4. ON THE EXTENSION OF SLAU SCHEME TO COMPRESSIBLE TWO-FLUID MODEL

A paper Published in 53rd AIAA Aerospace Sciences Meeting,

AIAA SciTech Forum, (AIAA 2015-0285)

Zahra Hosseinzadeh Nik[8], Jonathan D. Regele.[9], Alberto Passalacqua[10]

Abstract

This paper describes the extension of a simple low-dissipation AUSM (SLAU) scheme to a six-equation compressible two-fluid model for gas/liquid flow. This is the latest version of the AUSM-family schemes with a new numerical flux function. This scheme features low dissipation without any tunable parameters in low Mach number regimes while maintaining the robustness of the AUSM-family fluxes at high Mach numbers with a very simple formulation. The accuracy of the method is tested with a well-known two-fluid air/water flow benchmark problem and the results were compared with the two-phase AUSM$^+$ and AUSM$^+$-up schemes.

4.1 Introduction

Accurate methods to simulate multiphase flows are necessary to produce models for engineering applications. Modern commercial solvers employ a range of methods, such as the mixture model, volume-of-fluid model, or the Euler-Euler two-fluid approach [1], [2].These approaches are generally pressure-based and assume incompressibility of the liquid phase. However, because of their limited accuracy, as well as inability to model strong compressibility effects, the current generation of two-phase flow schemes are density-based. Furthermore, these

[8] Graduate Research Assistant of Aerospace and Mechanical Engineering, Iowa State University.
[9] Assistant Professor of Aerospace Engineering, Iowa State University.
[10] Assistant Professor of Mechanical Engineering, Iowa State University

algorithms can be problematic because the governing equations contain non-hyperbolicity, non-conservative form, and numerical stiffness from the large disparity in fluid properties and flow scales [3].On the other hand, in the density based solvers, either for single or two-phase flow, special care must be taken to prevent slow or stalled convergence, which can occur from the large ratio of characteristic speeds and errors arising from excessive amounts of numerical dissipation [4].

The AUSM (Advection Upstream Splitting Method), originally developed by Liou and Steffen [5] and its variant AUSM-family schemes are known to be excellent at resolving flow discontinuities while remaining computationally inexpensive and not requiring characteristic analysis or field by field decomposition [6].Thus, they have been widely used as one of the standard methods of compressible CFD algorithms, especially when dealing with non-hyperbolic models, or with models whose mathematical properties depend closely on closure laws as in two-phase flow. This scheme has been employed successfully by several authors to simulate multiphase flow in different test cases [7]–[11]. Recently, all-speed versions of the AUSM-family of schemes have been developed that can be used for flows at a variety of Mach numbers[12]. However, these schemes include at least one problem-dependent parameter, such as a cut-off Mach number. This parameter should be a very small and non-zero number for very low Mach number flows. This approach can be problematic since there is no standard method to define the cut-off Mach number, especially when no uniform flow is present [4], [13].

Recently, a new, simple low-dissipation numerical flux function of the AUSM-family has been developed [4], [13] for all speeds, called the simple low-dissipation AUSM (SLAU). In contrast with previous all-speed schemes, the simple low-dissipation AUSM features low dissipation without any tunable parameters in a low Mach number regime while maintaining the

robustness of the AUSM-family fluxes against shock-induced anomalies at high Mach numbers (e.g., carbuncle phenomena). Furthermore, the simple low-dissipation AUSM has a simpler formulation than other all-speed schemes [14]–[16].

The objective of this study is to develop a simple two-phase low-dissipation AUSM-family (TSLAU) scheme, which is free from reference parameters, such as a cutoff Mach number. This paper will be organized as follows. First, the system of equations for a single-pressure two-fluid model is described. Second, the spatial discretization of these equations using the two-phase AUSM$^+$[7], modified two phase AUSM$^+$-up, [8], [9], [12] and our new TSLAU scheme is elucidated. Third, the details about the temporal discretization, source terms, equations of state, and primitive variable deduction procedures are explained. Finally, the method's capabilities are evaluated using a well-known benchmark problem.

4.2 System of Equations

In this paper, we will concentrate on the numerical algorithms for compressible two-fluid equations in which the fluids are assumed to be inter-penetrating, non-homogeneous and non-equilibrium. In other words, each fluid has its own velocity and temperature field at a given location, but all fluids share the same pressure, such that $p_l = p_g$ where p_k is the pressure of the k$^{\text{th}}$ phase and l and g denote the liquid and gas phases, respectively. The system of Euler's equations that describe the one-dimensional fluid behavior can be written in vector form as

$$\frac{\partial \boldsymbol{U_k}}{\partial t} + \frac{\partial \boldsymbol{F_k}}{\partial x} = \boldsymbol{C_k^{nv}} + \boldsymbol{S_k} \tag{4-1}$$

where $\boldsymbol{U}$ is the vector of conservative variables, $\boldsymbol{F}$ is the flux vector, $\boldsymbol{C_k^{nv}}$ is the vector of non-viscous differential source terms, and $\boldsymbol{S_k}$ is the vector of the source term containing all the non-differential terms. These are defined [7]

$$\boldsymbol{U_k} = (\alpha_k\rho_k \quad \alpha_k\rho_k u_k \quad \alpha_k\rho_k E_k)^T$$

$$\boldsymbol{F_k} = (\alpha_k\rho_k u_k \quad \alpha_k\rho_k u_k^2 + \alpha_k p \quad \alpha_k\rho_k u_k H_k)^T$$

$$\boldsymbol{C_k^{nv}} = \left(0 \quad p\frac{\partial \alpha_k}{\partial x} + F_k^{nv} \quad -p\frac{\partial \alpha_k}{\partial t} + u^{int}F_k^{nv}\right)^T \tag{4-2}$$

$$\boldsymbol{S_k} = (0 \quad \alpha_k\rho_k g_x + F_k^D \quad \alpha_k\rho_k u_k g_x + u^{int}F_k^D)^T$$

where α_k is the volume fraction, ρ_k the density, u_k the velocity, E_k the total energy, H_k the total enthalpy of the phase k, p the pressure, F_k^{nv} the non-viscous interfacial force (such as interfacial pressure force), u^{int} the interphase velocity, g_x the projection of the gravity vector onto the x-coordinate axis, and F_k^D the interphase drag force. The spatial discretization of this system of equations has been done using three finite volume schemes, namely, two-phase AUSM$^+$, AUSM$^+$-up and the new TSLAU scheme.

4.3 AUSM$^+$ and AUSM$^+$-up Schemes for Compressible Two-phase Flow

The two-fluid AUSM-family scheme is based on a decomposition of the flux into a convective term associated with the mass flux and a pressure term. Thus, the numerical flux at the interface is computed using

$$\boldsymbol{F_k^*} = \boldsymbol{F_k^{*C}} + \boldsymbol{F_k^{*p}} \tag{4-3}$$

The convective fluxes at the interface can be defined by simple upwinding based on the sign of $\dot{m}_k^*$ as

$$\boldsymbol{F_k^{*C}} = \frac{1}{2}\dot{m}_k^*[(\boldsymbol{\psi}_k)_L + (\boldsymbol{\psi}_k)_R] + \frac{1}{2}|\dot{m}_k^*|\,[(\boldsymbol{\psi}_k)_L - (\boldsymbol{\psi}_k)_R] \tag{4-4}$$

where $(\boldsymbol{\psi}_k)_{L/R} = [1 \quad u_k \quad H_k]_{L/R}^T$ are the conv7ected variables of mass, momentum, and energy for each phase at the left and right nodes. The mass flux at the interface for each phase

$$\dot{m}_k^* = a_k^* \left((\alpha_k \rho_k)_L \frac{M_k^* + |M_k^*|}{2} + (\alpha_k \rho_k)_R \frac{M_k^* + |M_k^*|}{2} \right) \tag{4-5}$$

is then calculated using an upwinding scheme based on the direction of the interface Mach number, where $a_k^* = \sqrt{(a_k)_L (a_k)_R}$ is the interface numerical speed of sound. The numerical Mach number, M_k^*, at the interface is computed as a polynomial function of the left and right Mach numbers

$$M_k^* = f^+((M_k)_L) + f^-((M_k)_R) \tag{4-6}$$

where $f^\pm$ are polynomial functions defined as

$$f^\pm(M) = \begin{cases} \frac{1}{2}(M \pm |M|) & \text{if } |M| \geq 1 \\ \pm\frac{1}{4}(1 \pm M)^2 \pm \frac{1}{8}(M^2 - 1)^2 & \text{else} \end{cases}. \tag{4-7}$$

The left and right Mach number $(M_k)_{L/R}$ are defined

$$(M_k)_{L/R} = \frac{(u_k)_{L/R}}{a_k^*}. \tag{4-8}$$

The pressure flux is defined $\boldsymbol{F}_k^p = [0 \quad (\alpha_k p)^* \quad 0]^T$. The pressure at the interface $(\alpha_k p)^*$ is defined as a weighted average of the left and right pressures

$$(\alpha_k p)^* = \beta^+((M_k)_L)(\alpha_k p)_L + \beta^-((M_k)_R)(\alpha_k p)_R. \tag{4-9}$$

Here $\beta^\pm$ are polynomial functions of the Mach number defined as

$$\beta^\pm(M) = \begin{cases} \frac{1}{2}[1 + \text{sign}(\pm M)] & \text{if } |M| \geq 1 \\ \frac{1}{4}(2 \mp M)(M \pm 1)^2 \pm AM(M^2 - 1)^2 & \text{else} \end{cases}. \tag{4-10}$$

The coefficient A varies based upon the scheme that is used. In the original AUSM$^+$ scheme $A = \frac{3}{16}$ and in AUSM$^+$-up scheme $A = \frac{3}{16}(-4 + 5f_a^2)$. The other difference between these two schemes is that AUSM$^+$-up contains additional dissipation terms for both pressure and velocity. The original AUSM$^+$ scheme has mass flow rate and pressure given by Eq.((4-5) and ((4-9),

respectively, whereas the AUSM$^+$-up scheme adds additional velocity, D_k^u, and pressure, D_k^p, dissipation terms such that

$$\dot{m}_k^* = a_k^* \left((\alpha_k \rho_k)_L \frac{M_k^* + |M_k^*|}{2} + (\alpha_k \rho_k)_R \frac{M_k^* + |M_k^*|}{2} \right) + D_k^p \tag{4-11}$$

$$(\alpha_k p)^* = \beta^+((M_k)_L)(\alpha_k p)_L + \beta^-((M_k)_R)(\alpha_k p)_R + D_k^u. \tag{4-12}$$

The addition of these terms enhances the coupling between the mass flux and pressure terms, suppresses oscillations, improves stability as well as convergence, and solves the problematic low Mach number regime behavior. These terms are expressed

$$D_k^p = \left[-\frac{k_p}{f_a} \Delta \mathrm{M} \max(1 - \sigma \bar{M}^2, 0) \frac{\alpha_R p_R - \alpha_L p_L}{a_k^*} \right]_k \tag{4-13}$$

$$D_k^u = [-k_u \beta^+(M_L)\beta^-(M_R)\overline{\alpha\rho}(f_a a^*)(u_R - u_L)]_k \tag{4-14}$$

$$\Delta \mathrm{M} = f^+(M_L) - \tfrac{1}{2}(M_L + |M_L|) - f^-(M_R) + \tfrac{1}{2}(M_R - |M_R|), \tag{4-15}$$

where $\overline{\alpha\rho}$ and $\bar{M}$ are the average values in the L and R states and $f_a = M_0(2 - M_0)$ with $M_0^2 = \min[1, \max(\bar{M}^2, M_\infty)]$. The cut-off Mach number, M_∞ and the velocity, k_u, and pressure, k_p, dissipation coefficients are problem-dependent tunable parameters. These extra terms sacrifice the simplicity of the original AUSM-family algorithm. The SLAU scheme[4], [13], [16] overcomes this challenge for single phase Euler equations. However, a suitable algorithm is still needed for two-phase flow. In the next section we extend the SLAU all-speed scheme to two-phase flow and develop a TSLAU scheme of the AUSM-family. The resulting scheme is simple in form and free from problem-dependent parameters, such as a cut-off Mach number.

4.4 New Numerical Flux Scheme

As for its single phase counterpart described in Ref. [4], [13], [16], and similar to all AUSM-family schemes, the proposed two-fluid SLAU scheme is based on a decomposition of the flux

appearing in Eq. ((4-1) into a convective term associated with the mass flux and a pressure term, such that the flux is expressed

$$\boldsymbol{F}_k^* = \boldsymbol{F}_k^{*C} + \boldsymbol{F}_k^{*p}. \tag{4-16}$$

The convective fluxes at the interface can be calculated as

$$\boldsymbol{F}_k^{*C} = \frac{1}{2}\dot{m}_k^*[(\boldsymbol{\psi}_k)_L + (\boldsymbol{\psi}_k)_R] + \frac{1}{2}|\dot{m}_k^*|\,[(\boldsymbol{\psi}_k)_L - (\boldsymbol{\psi}_k)_R] \tag{4-17}$$

where $(\boldsymbol{\psi}_k)_{L/R} = [1 \quad u_k \quad H_k]_{L/R}^T$.In the SLAU scheme [4], [13], [16], the mass flux of AUSM+ is replaced with the Courant–Isaacson–Rees Roe scheme's mass flux [17].This approach modifies the mass flux in a proper form by using arithmetic averaged values rather than Roe averaged ones (see Ref. [13]). The resulting scheme achieves the accuracy of the Roe flux while keeping the robustness of AUSM+ against shock anomalies. In this paper, the final form of the SLAU mass flux is reformed for the two-fluid system. Therefore, the definition of the SLAU mass flux at the interface for the proposed two-phase model is expressed

$$\dot{m}_k^* = \frac{1}{2}\{\{(\alpha_k\rho_k u_k)_L + (\alpha_k\rho_k u_k)_R\} - |\bar{u}_k|\Delta(\alpha_k\rho_k)\}(1-g) - \frac{\chi_k}{2a_k^*}\Delta(\alpha_k p). \tag{4-18}$$

The mean velocity, $|\bar{u}|$, is the phasic density weighted average velocity of left and right states and is defined

$$|\bar{u}_k| = \left[\frac{\alpha_L\rho_L|u_L| + \alpha_R\rho_R|u_R|}{\alpha_L\rho_L + \alpha_R\rho_R}\right]_k. \tag{4-19}$$

The first term of the mass flux can be interpreted as the average of the left and right state. The second term, containing $\Delta(\alpha_k\rho_k)$, is called the density difference term and captures the direct diffusion. The third term is denoted as the pressure difference and represents acoustic damping under isentropic conditions because

$$\Delta(\alpha_k p) \approx a_k^*\Delta(\alpha_k\rho_k). \tag{4-20}$$

According to Liu [18], a mass flux that contains a pressure difference term tends to exhibit the carbuncle in high Mach number while based on Shima et al. [4], [13] it has a favorable effect in stabilizing low-speed flow computations. Thus, the dissipation produced by the pressure difference term should be alleviated for high-speed flow computations. A simple smoothing function for each phase

$$\chi_k = \left(1 + \widehat{M_k}\right)^2 \tag{4-21}$$

$$\widehat{M}_k = \min\left(1.0, \frac{1}{a_k^*}\sqrt{\frac{(u_k)_L^2 + (u_k)_R^2}{2}}\right) \tag{4-22}$$

is created that tends to zero in the supersonic regime and tends toward unity at low Mach numbers. This function is a two-phase extension of the smoothing function defined in Shima et al. [4], [13] and is used to limit the usage of the dissipation term in Eq. (4-18) to only subsonic flows. It helps maintain stability and boosts the ability of the scheme to work in all speeds. As opposed to the definition of the pressure dissipation term used in the original AUSM$^+$-up scheme mentioned in the previous section, this function is parameter independent. Furthermore, this function shows an asymptotic behavior against the local Mach number, whereas AUSM$^+$-up requires a prescribed cut-off Mach number, M_∞, for each particular problem. Finally, the function g in Eq. (4-18) is defined

$$g = -\max[\min((M_k)_L, 0), -1] . \min[\max((M_k)_R, 0), 1] \in [0,1] \tag{4-23}$$

where $(M_k)_{L/R}$ are the left and right Mach number in which the interface numerical speed of sound for each phase is $a_k^* = 0.5((a_k)_L + (a_k)_R)$, by the definition of $(M_k)_{L/R} = (u_k)_{L/R}/a_k^*$.

4.5 Temporal Discretization

As is common with other AUSM schemes [7], [19], a simple forward-Euler method is used for temporal discretization of the system of equations in Eq. ((4-1) at node m

$$\boldsymbol{U}_m^{t+\Delta t} = \boldsymbol{U}_m^t - \frac{\Delta t}{\Delta x}\boldsymbol{R}_m^f + \Delta t(\boldsymbol{R}_m^C + \boldsymbol{R}_m^S). \tag{4-24}$$

where t and t+Δt are the current and proceeding time levels respectively. The terms $\boldsymbol{R}_m^C$ and $\boldsymbol{R}_m^S$ represent the nodal residuals of the viscous differential and non-differential sources, which correspond to $\boldsymbol{C}_{\boldsymbol{k}}^{\boldsymbol{nv}}$and $\boldsymbol{S}_{\boldsymbol{k}}$, respectively. The nodal residual of convective fluxes $\boldsymbol{R}_m^f$ comes from the difference in the inflow and outflow. The global time step Δt is determined from an assumed volume fraction weighted average of the acoustic type signal:

$$\Delta t_{max} = CFL \times \min_m \left[\sum_k \frac{\alpha_k \Delta x}{|u_k|_m + (a_k)_m}\right], \tag{4-25}$$

where CFL is the CFL-like number used in Ref. [19]. Typical values of the CFL number vary between 0.1 and 0.9.

4.6 Source Terms

The six-equation two-phase flow system of equations is ill-posed in the sense that it may yield complex eigenvalues in some parts of the solution and becomes a non-hyperbolic system. To avoid these problems and enforce hyperbolicity various differential regularizing terms can be added to the system of equations. The introduction of these terms has been justified physically in Ref.[20]–[22]. The most important differential source term is the interfacial pressure, which is defined

$$p^{int} = c^p \frac{\alpha_g \rho_g \alpha_l \rho_l}{\alpha_g \rho_l + \alpha_l \rho_g}\left(u_g - u_l\right)^2, \tag{4-26}$$

with a hyperbolicity condition of $c^p \geq 1$. The non-viscous interfacial force F_k^{nv}, which is the interfacial pressure correction force, is expressed

$$F_k^{nv} = (p - p^{int})\frac{\partial \alpha_k}{\partial x}. \tag{4-27}$$

The interfacial velocity, which is needed in term $u^{int}F_k^{nv}$ in Eq. ((4-2), can be defined as

$$u^{int} = \alpha_g u_g + \alpha_l u_l. \tag{4-28}$$

As it is common in others AUSM-family schemes [7], [19], the non-differential drag and gravity source terms are discretized

$$(\alpha_k \rho_k g_x)_m = (\alpha_k)_m\,(\rho_k)_m g_x \tag{4-29}$$

$$(\alpha_k \rho_k u_k g_x)_m = (\alpha_k)_m\,(\rho_k)_m (u_k)_m g_x \tag{4-30}$$

$$(F_k^D)_m = \pm C_D \left(\alpha_g\right)_m \left(1-\alpha_g\right)_m \left(\rho_g\right)_m \left(\left(u_g\right)_m - (u_l)_m\right), \tag{4-31}$$

and C_D is a (positive) drag coefficient.

4.7 Equations of State and Primitive Variable Decoding

An equation of state (EOS) is needed to determine the thermodynamic quantities for the density, speed of sound, specific internal energy, specific total energy and specific total enthalpy, and also to transform the conservative variables into primitive variables. The ideal gas law is used for the gas-phase EOS. The gas phase density, internal energy, and sound speed can then be determined via

$$\rho_g = \frac{p}{RT_g} \tag{4-32}$$

$$e_g = \frac{RT_g}{\gamma_g - 1} \tag{4-33}$$

$$a_g = \sqrt{\frac{\gamma_g p}{\rho_g}} = \sqrt{\gamma_g R_g T_g}, \tag{4-34}$$

where R_g is the specific gas constant for air and the specific heat ratio is defined as γ_g. The liquid phase is governed by the stiffened-gas EOS where the liquid phase density, internal energy and sound speed are expressed

$$\rho_d = \frac{\gamma_l}{\gamma_l - 1}\frac{p + p_\infty}{C_{p_l}T_l} \tag{4-35}$$

$$e_d = \frac{C_{p_l}T_l}{\gamma_l} + \frac{p_\infty}{\rho_l} \tag{4-36}$$

$$a_l = \sqrt{\frac{\gamma_l(p + p_\infty)}{\rho_l}} = \sqrt{(\gamma_l - 1)C_{p_l}T_l} \tag{4-37}$$

with the constants, $\gamma_l = 2.8$, $p_\infty = 8.5 \times 10^8$ Pa and $C_{p_l} = 4186$ J/kg/K for water.

In the case of the two-fluid model, the primitive variables

$$Q = [\alpha_g \quad u_g \quad u_l \quad p \quad T_g \quad T_l]^T \tag{4-38}$$

are obtained after using the temporal integration outlined previously to determine the conservative variables $\boldsymbol{U}$ at the time $t + \Delta t$. The phase velocities, total energies and specific internal energies can immediately be resolved [7], [19]:

$$u_g^{t+\Delta t} = \frac{U_3^{t+\Delta t}}{U_1^{t+\Delta t}} = \frac{\left(\alpha_g\rho_g u_g\right)^{t+\Delta t}}{\left(\alpha_g\rho_g\right)^{t+\Delta t}} \tag{4-39}$$

$$u_l^{t+\Delta t} = \frac{U_4^{t+\Delta t}}{U_2^{t+\Delta t}} = \frac{(\alpha_l\rho_l u_l)^{t+\Delta t}}{(\alpha_l\rho_l)^{t+\Delta t}} \tag{4-40}$$

$$e_g^{t+\Delta t} = \frac{U_5^{t+\Delta t}}{U_1^{t+\Delta t}} - \frac{1}{2}\left(\frac{U_3^{t+\Delta t}}{U_1^{t+\Delta t}}\right)^2 = \frac{\left(\alpha_g\rho_g E_g\right)^{t+\Delta t}}{\left(\alpha_g\rho_g\right)^{t+\Delta t}} - \frac{\left(u_g^{t+\Delta t}\right)^2}{2} \tag{4-41}$$

$$e_l^{t+\Delta t} = \frac{U_6^{t+\Delta t}}{U_2^{t+\Delta t}} - \frac{1}{2}\left(\frac{U_4^{t+\Delta t}}{U_2^{t+\Delta t}}\right)^2 = \frac{(\alpha_l\rho_l E_l)^{t+\Delta t}}{(\alpha_l\rho_l)^{t+\Delta t}} - \frac{\left(E_g^{t+\Delta t}\right)^2}{2} \tag{4-42}$$

EOSs are then required to determine the pressure, temperature and subsequently the void fractions by implicit root-finding. In the stiffened-gas model the pressure is found through the root of a quadratic equation [7], [19] where

$$A = U_1^{t+\Delta t}(\gamma_g - 1)e_g^{t+\Delta t} \tag{4-43}$$

$$B = U_2^{t+\Delta t}(\gamma_l - 1)\, e_l^{t+\Delta t} \tag{4-44}$$

$$\Delta = (\gamma_l p_\infty - A - B)^2 + 4A\gamma_l p_\infty \tag{4-45}$$

$$p^{t+\Delta t} = \frac{1}{2}\left[A + B - \gamma_l p_\infty + \sqrt{\Delta}\right] \tag{4-46}$$

and the void fraction is defined

$$\alpha_g = \frac{A}{p}. \tag{4-47}$$

The temperature is explicitly defined from the internal energy of each phase

$$T_g^{t+\Delta t} = \frac{\gamma_g - 1}{R_g} e_g^{t+\Delta t} \tag{4-48}$$

$$T_l^{t+\Delta t} = \frac{\gamma_l e_l^{t+\Delta t}}{\left[(\gamma_l - 1)\frac{p_\infty}{p + p_\infty} + 1\right] C_{p_l}}. \tag{4-49}$$

4.8 Results and Discussions

We now present the results of a test problem that demonstrates the method's ability. For this study we focused on Toumi's shock-tube problem [23], [24] in which the liquid phase is water, governed by the stiffened gas EOS, and the gas phase is air, governed by the ideal gas law. This test case is commonly used [7], [19], [23], [24] to test the robustness of an algorithm to handle shock waves with a pressure magnitude on the order of 10^7 Pa. In this case, two shock waves and two expansion fans are generated by the system that are challenging to capture numerically and highlight the effects of the different models and model parameters. At the initial state, we have two different mixtures of water and air on either side of a diaphragm located at x = 5 inside a

domain $x \in [0, 10]$. Thus, the initial condition can be characterized by the two different primitive states

$$Q_L = [0.25 \quad 0\,m/s \quad 0\,m/s \quad 2 \times 10^7 Pa \quad 308.15\,K \quad 308.15\,K]^T$$

$$Q_R = [0.1 \quad 0\,m/s \quad 0\,m/s \quad 1 \times 10^7 Pa \quad 308.15\,K \quad 308.15\,K]^T.$$

The transient behavior begins after removing the membrane at $t = 0$. Since, there is no analytical solution to this test case, it is common [2], [7], [19] to perform a grid convergence study in order to determine if the structures are captured properly. For this test case, grids ranging from 200 to 10,000 nodes were tested. The two-phase AUSM$^+$, AUSM$^+$-up and TSLAU schemes were used for comparison. Each model was run until t=0.006 s with $c^p = 2.0$ and $CFL = 0.1$. The modified low-Mach model in AUSM$^+$-up is used with $k_u = 1$, $k_p = 1$ and $M_\infty = 10^{-4}$.

Figure 4-1 illustrates the results for gas and liquid velocities for the two-phase AUSM$^+$, AUSM$^+$-up and TSLAU schemes. As noted in Ref. [7] and [8]the eigenvalues include one pair of pressure/density waves, one pair of pressure/void waves, and two convective waves. Therefore, Fig. 1 shows five constant states, separating two expansion waves and two compression waves. The strongest expansion wave propagates to the left in the high-pressure region, the right-most shock wave propagates to the right in the low-pressure region, and contact-like waves exist in between these two structures. Finer grid resolution creates more distinct constant states and coarser grid resolution generates more smoothed profiles. For low resolution cases it is difficult to see the constant state located just to the right of $x = 5$. Only for a resolution $N \geq 3200$ does it become clear that this is another constant state region.

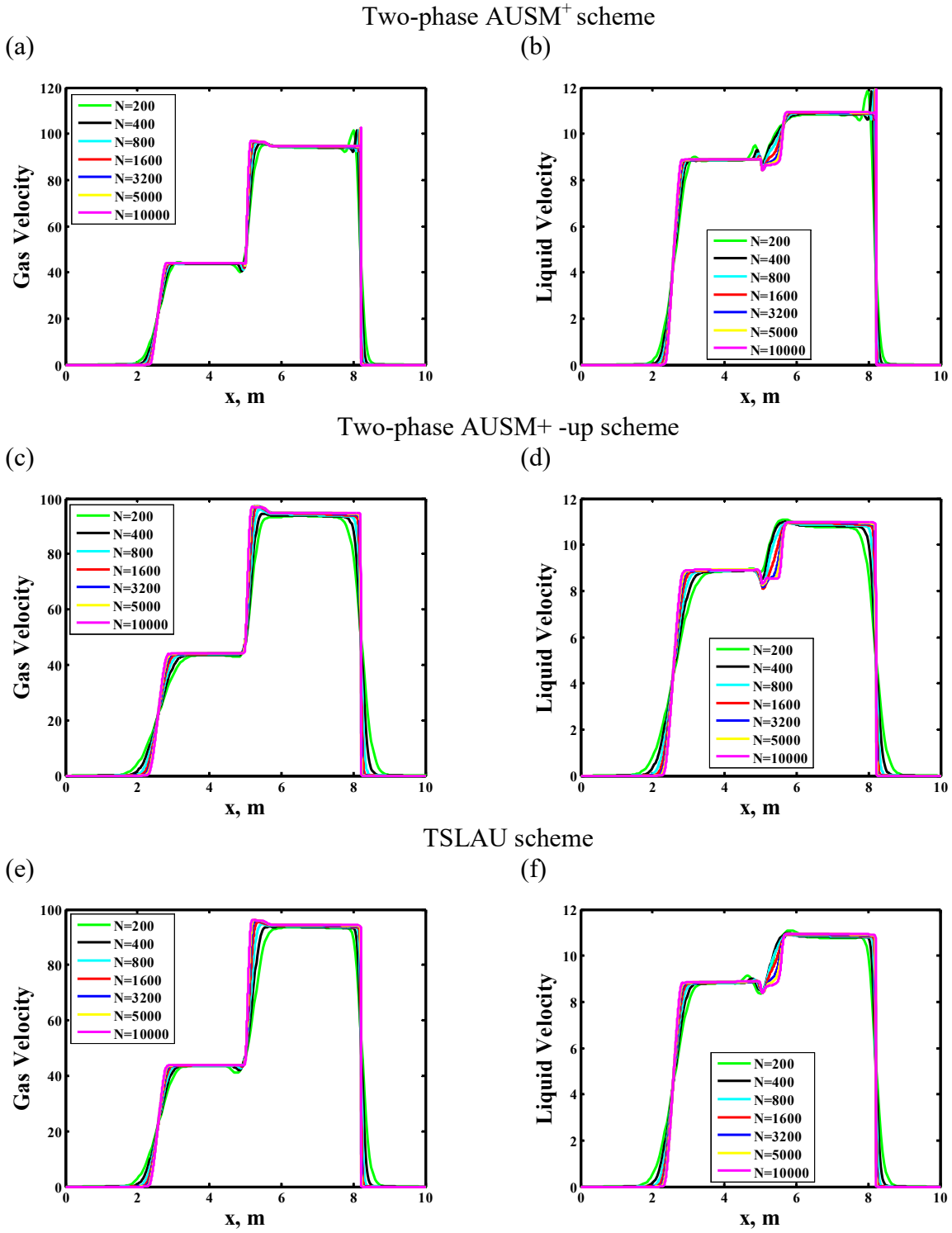

Figure 4-1 Two-Fluid shock tube problem: grid convergence with each scheme for gas and liquid velocities

Figure 4-1(a) and (b) shows that for all grid resolutions the standard two-phase AUSM$^+$ scheme exhibits large overshoots at the shock wave and contact discontinuities. The results for the modified AUSM$^+$-up and the new TSLAU (Figure 4-1 (c)-(f)) show that both of these schemes are able to capture the shock and expansion profile sharply while minimizing overshoots and oscillations. These results are consistent with the Paillere et al. [7] and Chang and Liou [8], [10].

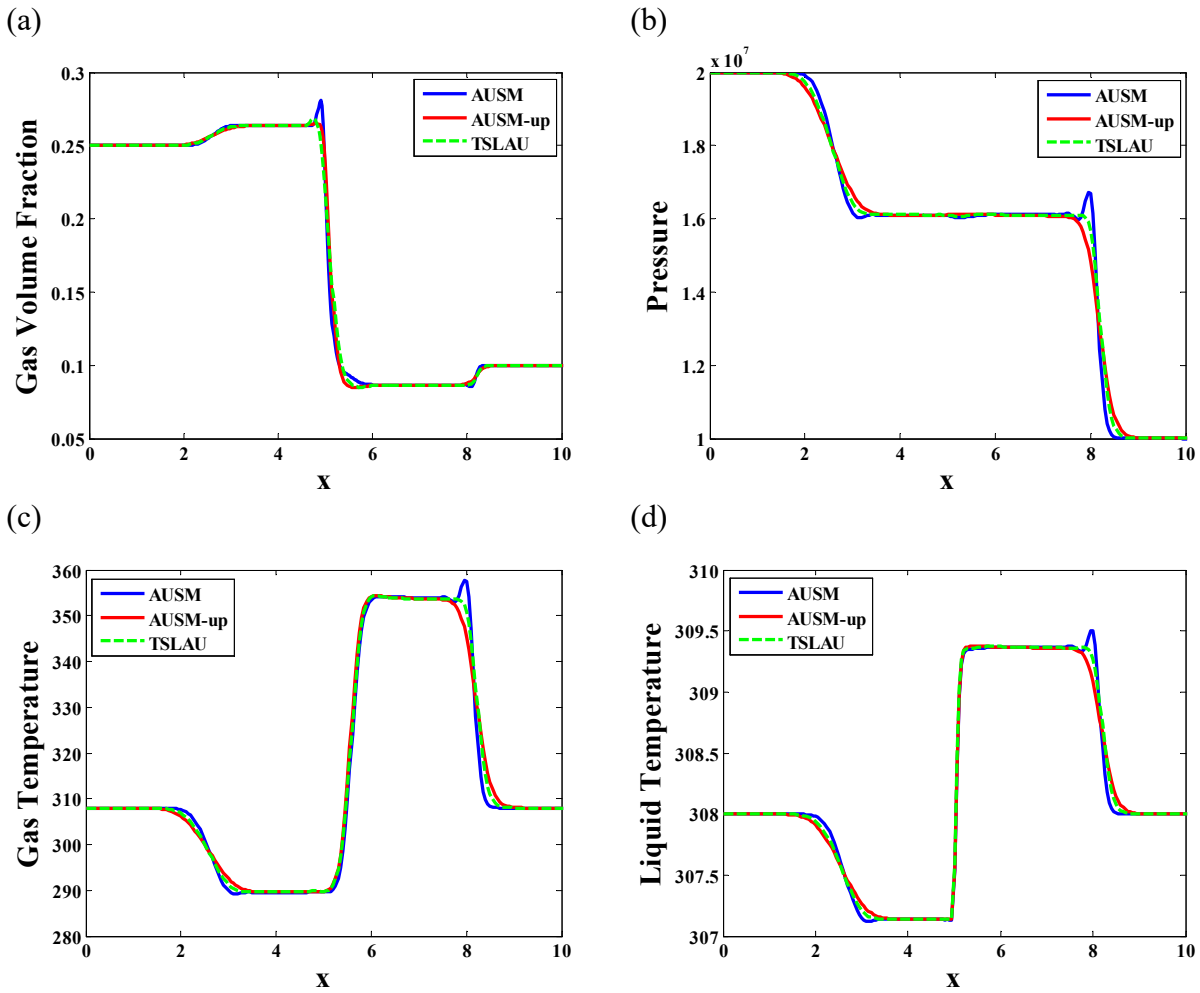

Figure 4-2 Profile of (a) gas volume fraction, (b) Pressure, (c) gas temperature (d) liquid temperature for two-phase AUSM$^+$, AUSM$^+$-up and TSLAU.

In order to better compare the three methods, Figure 4-2 shows the profile of the (a) gas volume fraction, (b) pressure, (c) gas temperature and (d) liquid temperature for a grid size of 200.

The shock capturing behavior is easier to follow in pressure and temperature profiles (Figure 4-2 (b)-(d)). These figures show that the original AUSM$^+$ has a strong overshoot at the shock location ($x = 8$) while AUSM$^+$-up and TSLAU minimize this overshoot through the introduction of the pressure and velocity dissipation terms that better couple the pressure and mass flux. However, the AUSM$^+$-up in which the dissipation coefficients and cut-off Mach number are tunable, has a smoother shock in comparison with the parameter free TSLAU scheme. In fact, in the AUSM$^+$-up scheme these coefficients need to be tuned for each problem to achieve a favorable behavior while TSLAU provides excellent results without any manipulations. The figures also show that the oscillations at the expansion (located at $x = 2.5$) are reduced in the both AUSM$^+$-up and TSLAU schemes while the sharpest expansion is captured using TSLAU. Figure 4-2(a), which shows the volume fraction profile, illustrates the ability of each scheme to treat the contact discontinuity (located at $x = 5$). The original AUSM$^+$ has a strong oscillation near the contact. AUSM$^+$-up and TSLAU schemes both capture the contact with less oscillation. However, due to the lower dissipation in TSLAU compared to AUSM$^+$-up, small oscillations are still observed. In summary, the TSLAU scheme optimizes the dissipation such that it captures shocks and expansions with less dissipation while still minimizing the oscillation at contact discontinuities.

4.9 Conclusion

In this paper, the recent SLAU scheme is extended to solve the two-fluid model equations, where the stiffened gas model describes the liquid phase. This scheme has a simple compressible numerical flux function from the AUSM-family for all speeds in each phase and involves no tunable parameters (e.g., cut-off Mach number or reference velocity) as opposed to the previous schemes. Therefore, it is robust, and efficient for computations over a wide range of Mach numbers for each phase. This scheme, a two-phase low-dissipation AUSM or TSLAU scheme, is simpler

than the existing all-speed two-fluid AUSM schemes and can easily be coded and extended for complex physics and geometries. A well-known two-fluid benchmark problem is successfully tested, showing the accuracy of the scheme. The results are compared against AUSM$^+$ and AUSM$^+$-up two-phase schemes. The comparison shows that the TSLAU scheme minimizes overshoots and undershoots near shocks and expansions. Overall the scheme optimizes the numerical dissipation such that shocks and expansion waves are captured more sharply while minimizing oscillations at contact discontinuities.

References

[1] J. Madsen, *Computational and Experimental Study of Sprays from the Breakup of Water Sheets*, no. October. Group for Chemical Fluid Flow Processes, Esbjerg Institute of Technology, Aalborg University Esbjerg, 2006.

[2] D. J. Robbins, R. S. Cant, and L. F. Gladden, "Simulation of Multiphase Flows Using a Modified Upwind-Splitting Scheme," *World Acad. Sci. Eng. Technol. Int. J. Math. Comput. Phys. Electr. Comput. Eng.*, vol. 6, no. 8, pp. 1216–1222, 2012.

[3] M.-S. Liou, C.-H. Chang, L. Nguyen, and T. G. Theofanous, "How to Solve Compressible Multifluid Equations: A Simple, Robust, and Accurate Method."

[4] E. SHIMA and K. KITAMURA, "On New Simple Low-Dissipation Scheme of AUSM-Family for All Speeds," in *47th AIAA Aerospace Sciences Meeting including The New Horizons Forum and Aerospace Exposition*, 2009.

[5] M.-S. Liou and C. J. Steffen, "A New Flux Splitting Scheme," *J. Comput. Phys.*, vol. 107, no. 1, pp. 23–39, Jul. 1993.

[6] M. Liou, "A Sequel to AUSM: AUSM," *J. Comput. Phys.*, vol. 129, pp. 364–382, 1996.

[7] H. Paillère, C. Corre, and J. R. García Cascales, "On the extension of the AUSM+ scheme to compressible two-fluid models," *Comput. Fluids*, 2003.

[8] C.-H. Chang and M.-S. Liou, "A New Approach to the Simulation of Compressible Multifluid Flows with AUSM+ Scheme," in *16th AIAA Computational Fluid Dynamics Conference*, 2003.

[9] C. H. Chang and M. S. Liou, "A robust and accurate approach to computing compressible multiphase flow: Stratified flow model and AUSM+-up scheme," *J. Comput. Phys.*, vol. 225, pp. 840–873, 2007.

[10] M. M.-S. Liou, L. Nguyen, T. G. Theofanous, C. C.-H. Chang, L. Nguyen, and T. G. Theofanous, "How to Solve Compressible Multifluid Equations: a Simple, Robust, and Accurate Method," *AIAA J.*, vol. 46, no. 9, pp. 2345–2356, Sep. 2008.

[11] Y. Y. Niu, Y. C. Lin, and C. H. Chang, "A further work on multi-phase two-fluid approach for compressible multi-phase flows," *Int. J. Numer. Methods Fluids*, 2008.

[12] M. S. Liou, "A sequel to AUSM, Part II: AUSM+-up for all speeds," *J. Comput. Phys.*, vol. 214, no. 1, pp. 137–170, 2006.

[13] E. Shima and K. Kitamura, "Parameter-Free Simple Low-Dissipation AUSM-Family Scheme for All Speeds," *AIAA J.*, vol. 49, no. 8, pp. 1693–1709, Aug. 2011.

[14] K. Kitamura, P. Roe, and F. Ismail, "Evaluation of Euler Fluxes for Hypersonic Flow Computations," *AIAA J.*, vol. 47, no. 1, pp. 44–53, Jan. 2009.

[15] K. Kitamura, E. Shima, Y. Nakamura, and P. L. Roe, "Evaluation of Euler Fluxes for Hypersonic Heating Computations," *AIAA J.*, vol. 48, no. 4, pp. 763–776, Apr. 2010.

[16] K. Kitamura, E. Shima, K. Fujimoto, and Z. J. Wang, "Performance of low-dissipation euler fluxes and preconditioned LU-SGS at low speeds," *Commun. Comput. Phys.*, 2011.

[17] P. L. Roe, "Approximate Riemann solvers, parameter vectors, and difference schemes," *Journal of Computational Physics*. 1981.

[18] M.-S. Liou, "Mass Flux Schemes and Connection to Shock Instability," *J. Comput. Phys.*, vol. 160, no. 2, pp. 623–648, May 2000.

[19] J. R. García-Cascales and H. Paillère, "Application of AUSM schemes to multi-dimensional compressible two-phase flow problems," *Nucl. Eng. Des.*, 2006.

[20] W. G. Gray and P. C. Y. Lee, "On the theorems for local volume averaging of multiphase systems," *Int. J. Multiph. Flow*, 1977.

[21] J. D. Ramshaw and J. A. Trapp+, "Characteristics, Stability, and Short-Wavelength Phenomena in Two-Phase Flow Equation Systems," *Nucl. Sci. Eng.*, vol. 66, pp. 93–102, 1978.

[22] V. H. Ransom and D. L. Hicks, "Hyperbolic two-pressure models for two-phase flow," *J. Comput. Phys.*, 1984.

[23] I. Toumi, A. Kumbaro, and H. Paillere, "Approximate Riemann solvers and flux vector splitting schemes for two-phase flow," 1999.

[24] I. Toumi, "An Upwind Numerical Method for Two-Fluid Two-Phase Flow Models," *Nucl. Sci. Eng.*, vol. 123, no. 2, pp. 147–168, 1996.

CHAPTER 5. CONCLUSION

The goal of this work is numerical investigation of shock-particle interaction in both compressible gas-solid and gas-liquid flow regime. Owing to complex dynamics and the uncharacteristic flow behavior involved in these problems, this work first focused on limiting the amount of modeling by fully resolving the flow features, through solving the full Navier-Stokes equations. Due to the multiscale nature of these interactions, the numerical solver is developed in the Parallel Adaptive Wavelet Collocation Method framework (PAWCM). The PAWCM is a multiscale framework that uses wavelets to dynamically adapt the grid used, to represent the solution, which minimizes the overall computational cost and allows larger simulations to be performed. This framework provides the capability to generate highly resolved grids only on the necessary regions of the fluid.

In the gas-solid regime, a characteristic based Immersed boundary method suitable for compressible flow is utilized to impose the no-slip and adiabatic condition on the solid particles. The gas solid solver is validated against experimental data, for the shock interaction with a single particle. Then it is employed to replicate shock-particle cloud interaction in the multiphase shock tube experiment of Wagnar et al. [1] to reveal flow physics involved in the particle cloud and the wake behind that. Similar to the Euler's simulation in Regele et al. [2], we observed a high unsteady effect and large velocity fluctuations, however the magnitude of the velocity fluctuations are more realistic due to the presence of physical viscosity in our Navier-Stokes solver. The present work quantifies the flow unsteadiness and velocity fluctuations to answer the question of "why is the unsteadiness large and why are the velocity fluctuations in the same order as the mean velocity field". The quantification of the shock-particle cloud interaction is performed against a gradually

induced flow over the particle cloud, to remove the impulsive effect of the shock and understand how much the impulsive effect contributes to the unsteadiness and the fluctuating field statistics. The numerical results on evolution of complex wave system, dilatation effect and local supersonic zones and the interaction points with the vortical structures reveal interesting information about the strong unsteadiness observed. The vorticity equation budget is performed to analyze the sources of unsteadiness. A detailed analysis of the velocity fluctuation and kinetic energy in the fluctuating motion is performed, for both cases, to ascertain the importance of the velocity fluctuations that arise from the strong unsteadiness in the shock induced case.

In the next step, a compressible gas-liquid flow solver is developed for the PAWCM framework to account for the deformation and advection of droplet interface, as well as surface tension effect, during the shock-droplet interaction. An interface capturing scheme, based on the five-equation model is developed to capture interface dynamics. An interface compression scheme is also developed for PAWCM to maintain the immiscibility condition and counter the interface smearing due to the numerical diffusion. The surface tension is implemented based on the continuum surface force. One dimensional test problems showed the ability of the flow solver to resolve both shock and interface over just a few points with minimal spurious oscillation across the interface. 2D test problems showed the ability of the code in shape preservation and predicting accurate interface dynamics in presence and absence of surface tension effect.

Finally, to further investigate the problem of multiphase shock tube and attempt to model the flow behavior based on the PR-DNS results, a two-phase shock capturing scheme is developed to solve the six equation, two-fluid model. The scheme is developed based on the extension of a Simple Low dissipation AUSM (SLAU) scheme and is called a Two-phase SLAU (TSLAU) scheme. TSLAU is free from the tunable parameters, and in comparison with the AUSM$^+$ and

AUSM^{+}-up two-phase schemes it minimizes overshoots and undershoots near shocks and expansions. Overall the scheme optimizes the numerical dissipation such that shocks and expansion waves are captured more sharply while minimizing oscillations at contact discontinuities.

References

[1] J. L. Wagner, S. J. Beresh, S. P. Kearney, B. O. M. Pruett, and E. K. Wright, "Shock tube investigation of quasi-steady drag in shock-particle interactions," *Phys. Fluids*, vol. 24, no. 12, p. 123301, Dec. 2012.

[2] J. D. Regele, J. Rabinovitch, T. Colonius, and G. Blanquart, "Unsteady effects in dense, high speed, particle laden flows," *Int. J. Multiph. Flow*, vol. 61, no. May, pp. 1–13, 2014.